2007

Dimesionality Aspects Of Nano Micro Integrated Metal Oxide Based Early Stage Leak Detection Room Temperature Hydrogen Sensor

Sameer Arun Deshpande
University of Central Florida

STARS Citation

Deshpande, Sameer Arun, "Dimesionality Aspects Of Nano Micro Integrated Metal Oxide Based Early Stage Leak Detection Room Temperature Hydrogen Sensor" (2007). *Electronic Theses and Dissertations, 2004-2019*. 3140.
https://stars.library.ucf.edu/etd/3140

DIMESIONALITY ASPECTS OF NANO MICRO INTEGRATED METAL OXIDE BASED EARLY STAGE LEAK DETECTION ROOM TEMPERATURE HYDROGEN SENSOR

by

SAMEER ARUN DESHPANDE
B.E. University of Pune, 2001
M.S. University of Central Florida, 2004

A dissertation submitted in partial fulfillment of the requirements
for the degree of Doctor of Philosophy
in the Department of Mechanical, Materials and Aerospace Engineering
in the College of Engineering and Computer Science
at the University of Central Florida
Orlando, Florida

Fall Term
2007

Major Professor: Sudipta Seal

ABSTRACT

Detection of explosive gas leaks such as hydrogen (H_2) becomes key element in the wake of counter-terrorism threats, introduction of hydrogen powered vehicles and use of hydrogen as a fuel for space explorations. In recent years, a significant interest has developed on metal oxide nanostructured sensors for the detection of hydrogen gas. Gas sensors properties such as sensitivity, selectivity and response time can be enhanced by tailoring the size, the shape, the structure and the surface of the nanostructures. Sensor properties (sensitivity, selectivity and response time) are largely modulated by operating temperature of the device. Issues like instability of nanostructures at high temperature, risk of hydrogen explosion and high energy consumption are driving the research towards detection of hydrogen at low temperatures. At low temperatures adsorption of O_2^- species on the sensor surface instead of O^- (since O^- species reacts easily with hydrogen) result in need of higher activation energy for hydrogen and adsorbed species interaction. This makes hydrogen detection at room temperature a challenging task. Higher surface area to volume ratio (resulting higher reaction sites), enhanced electronic properties by varying size, shape and doping foreign impurities (by modulating space charge region) makes nanocrystalline materials ideal candidate for room temperature gas sensing applications. In the present work various morphologies of nanostructured tin oxide (SnO_2) and indium (In) doped SnO_2 and titanium oxide (titania, TiO_2) were synthesized using sol-gel, hydrothermal, thermal evaporation techniques and

successfully integrated with the micro-electromechanical devices H_2 at ppm-level (as low as 100ppm) has been successfully detected at room temperature using the SnO_2 nanoparticles, SnO_2 (nanowires) and TiO_2 (nanotubes) based MEMS sensors. While sensor based on indium doped tin oxide showed the highest sensitivity (S =Ra/Rg= 80000) and minimal response time (10sec.). Highly porous SnO_2 nanoparticles thin film (synthesized using template assisted) showed response time of about 25 seconds and sensitivity 4. The one dimensional tin oxide nanostructures (nanowires) based sensor showed a sensitivity of 4 and response time of 20 sec. Effect of aspect ratio of the nanowires on diffusion of hydrogen molecules in the tin oxide nanowires, effect of catalyst adsorption on nanowire surface and corresponding effect on sensor properties has been studied in detail. Nanotubes of TiO_2 prepared using hydrothermal synthesis showed a sensitivity 30 with response time as low as 20 seconds where as, TiO_2 nanotubes synthesized using anodization showed poor sensitivity. The difference is mainly attributed to the issues related to integration of the anodized nanotubes with the MEMS devices.

The effect of MEMS device architecture modulation, such as, finger spacing, number and length of fingers and electrode materials were studied. It has been found that faster sensor response (~ 10 sec) was observed for smaller finger spacing. A diffusion model is proposed for elucidating the effect of inter-electrode distance variation on conductance change of a nano-micro integrated hydrogen sensor for room temperature operation. Both theoretical and experimental results showed a faster response upon exposure to hydrogen when sensor electrode gap was smaller. Also, a linear increase in the sensor sensitivity from 500 to 80000 was observed on increasing the electrode spacing from 2 to 20 μm. The improvement in sensitivity is attributed to the higher reactive sites available for the gaseous species to react on the sensor surface. This phenomenon also correlated to surface adsorbed oxygen vacancies (O^-) and the rate of change of surface adsorbed oxygen vacancies.

This dissertation studied in detail dimensionality aspects of materials as well as device in detecting hydrogen at room temperature.

Dedicated to my parents

Mr. Arun Bhaskar Deshpande *(Baba)*

& Mrs. Neela Arun Deshpande *(Aai)*

ACKNOWLEDGMENTS

I wish to thank my faculty advisor, Prof. Sudipta Seal, for providing me the support and giving me an opportunity to work on various interesting projects during my course of study and research at UCF. His motivation and guidance is appreciated.

I am very grateful to Dr. Hyoung J. Cho and his graduate students, Peng Zhang and Shyam Londe for Fabricating the MEMS based sensor devices. I also thank Dr. Cho for being on my thesis committee. I would like to thank Dr. Jiyu Fang for being on my thesis committee and his valuable discussions. I am also thankful to Dr. Alfons Schulte and Dr. Pedro Medelius for being on thesis committee. I would also like to thank Dr. Shukla for his valuable guidance in introducing me to gas sensor research.

I would also like to thank Dr. H.W. Hillhouse and his student Mr. Vikrant Urade, Purdue University for synthesis of porous nanostructured SnO_2 films.

I thank Materials Characterization Facility (MCF) at UCF for offering the characterization facilities required for conducting this research work. Also, I would like to acknowledge all the students in the Surface Engineering and Nanotechnology Facility (SNF) and my friends for their cooperation and support.

I am grateful for financial support by NASA, NASA-Glenn, NSF CBET and NSF career (Dr. Cho) for sensor research. Most of all, I would like to thank my parents, sister and brother in law for all their love and for always being there for me.

TABLE OF CONTENTS

LIST OF FIGURES

LIST OF TABLES

LIST OF ABBREVIATIONS

1-D	One Dimensional
Ar	Argon
CO	Carbon Monoxide
CO_2	Carbon Dioxide
CeO_2	Cerium Oxide
CTAB	Cetyltrimethylammonimum Bromide
CVD	Chemical Vapor Deposition
FESEM	Field Emission Scanning Electron Microscopy
H_2	Hydrogen
HRTEM	High Resolution Transmission Electron Microscopy
MEMS	Micro Electro Mechanical Systems
N_2	Nitrogen
Nano	Nanostructured
NEMS	Nano Electro Mechanical Systems
Ppb	Part Per Billion
Ppm	Part Per Million
SCL	Space Charge Layer
SEM	Scanning Electron Microscopy
SnO_2	Tin Oxide/ Stannic Oxide
SXAS	Small Angle X Ray Scattering
TiO_2	Titania/ Titanium Oxide/ Titanium Dioxide

TEM	Transmission Electron Microscopy
Vol	Volume
XPS	X-Ray Photoelectron Spectroscopy
XRD	X-Ray Diffraction

CHAPTER 1. INTRODUCTION

1.1. Nanotechnology

December 29, 1959 is one of the astonishing days in Human Evolution. Through the lecture titled *“There is a plenty of a room at bottom”* Richard Feynman introduced the concept of nanotechnology to Human world[1]. But actual word “nanotechnology” was first introduced by Professor N. Taniguchi in 1974.[2] Actual potential of this science got highlighted by the Noble prize winning innovation by Smalley’s group of carbon buckyball and fullerene structures, first electron microscopic image of carbon microtubules, later famously known as carbon nanotubes (CNT). By definition, a “nano” meter is billionth of meter. A considerable interest in nanostructures has developed because they possess better physical-chemical properties as compared to their bulk counterparts[3]. Nanostructured materials can be made in various shapes and sizes, including spheres, rods, wires, tubes, and triangles. In this sense, invention in nanotechnology can be termed it as a science of 21st century. And there is no doubt that soon it will become an integral part of the daily life. Ability of nanotechnology in creating nanoscale architecture is widely studied and documented in the literature[3, 4,5]. The ease of nanostructured materials to undergo surface functionalization (e.g., biological, chemical, or physical) results wide application in various nanoscale devices[6, 7].

Structural and electrical aspects of nanostructured materials are significantly different from their bulk counterpart. Increase in the surface area by orders of magnitude results in a very large number of atoms on the surface of the material[8]. This leads to the variation in mechanical, physical, chemical and optical properties of the material[9]. Quantum confinement is the next most important term in the nanotechnology. *"Gold is not golden"* is one of the famous phrases of the nanotechnology which stemmed from the variation in color of the metallic gold (Au). A Nanocrystalline structure of the gold is red in color and which is due to the higher cumulative oscillations of the large no of electrons at the atomic level[9]. Also, change in inter-atomic distance of the nanocrystalline materials such as Cerium oxide (CeO_2) can be pertained to induced strain in the lattice due to the vacancies and lower number of atomic arrangement[10]. Such variations subsequently results in the variation in number of defects and dislocations. This further deviates the material properties and subsequently follows the inverse Hall-Petch relation[11]. Different types of nanomaterials and their application is briefly shown in figure 1.1

Nanostructures can be produced using two main methods, "top-down" and "bottom-up". In the "top down" approach, bulk precursors are used to create fine nanoparticles[8]. Lithography using ultraviolet (UV), optical and focused ion beam (FIB) for micro-scale and electron beam for nano-scale design are the few examples for top-down approach. In the "bottom up" approach, however, metal atoms are created via the reduction of metallic precursors, followed by controlled aggregation of the atoms to create a bulk component. This approach can be of different types: (a) chemical synthesis routes for materials, like CNT (b) biological self-assembly, e.g., DNA or proteins etc, and (c) mechanical manipulation of atoms using instruments, such as, atomic force microscope (AFM), scanning tunneling microscope (STM), Focused Ion Beam (FIB), etc. “Bottom- up” approach is more popular as compared to “top-down” since both size and uniformity are relatively easier to manipulate. Using bottom-up approach, the fabrication of nanostructured materials can be achieved by a number of synthesis techniques, such as, hydrothermal, [12] inert gas condensation,[13] plasma processing,[14] physical vapor deposition (PVD),[15] chemical vapor deposition (CVD),[16] mechanical alloying,[17] sol-gel,[18] micro-emulsion[19] etc

Following synthesis, nanostructures can be used to create various new devices. Especially, the field of sensors and actuators is benefited from the use of nanotechnology, particularly in the detection of gases, volatile organic compounds (VOCs) and bio-molecules. Homeland security and counter-terrorism[20] measures have driven the sensor research in developing nanostructures because of their ultrahigh detection ability and selectivity towards various chemical species[21]. For example, gas sensors based on chemi-resistor sensing are typically thin-film devices relying on electrical conductivity changes, upon exposure to specific chemical vapors. The following section discusses the importance of nanostructures in the sensor arena.

1.2. Nanostructured Materials for Sensor Application

Nanostructure materials can be used directly or indirectly for the sensor application. Any sensor has two major functions, namely, receptor function and actuator function[22]. The receptor function is pertained to the receiving and reacting with the targeting species while transportation of free careers is the driven by the actuation function. Nanostructures are incorporated in the MEMS devices in the form of films or particles for gas sensing applications. Ballistic transport of the free carriers (electrons) across the films/ particles is the main reason for the applications of nanostructures in sensing. Dimensionality of the nanostructures plays a key role in the gas sensing applications. 1 D nanostructures are favored over other forms of nanostructures for such applications. The size of the nanowires is comparable to the Fermi wavelength of the conducting electrons in the metal. The electrons transport ballistically along a nanowire and form a well-defined quantum mode in the transverse direction[23]. The conductance, G, does not change continuously with its diameter as in the case of larger conductors. Thus conductance becomes quantized and is described by the Landauer formula[24] :

$$G = G_0 \sum_{i=0}^{N} T_i \quad \text{...} \mathbf{1.1}$$

Where $G_0 = 2e^2/h \sim 1/13\ \mathrm{k\Omega}$ is the conductance quantum, T_i is the transmission coefficient of each mode, and summation is over all the quantum modes.

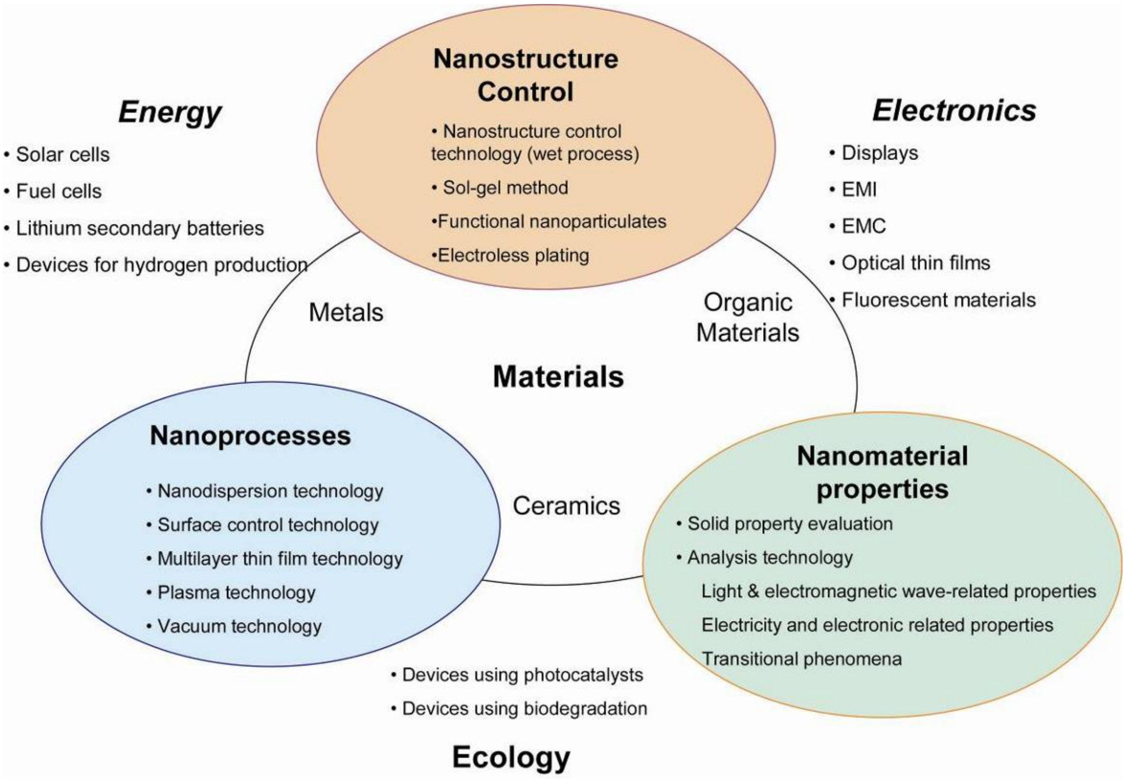

Figure 1.1 *Nanoworld*: figure showing various different types of nanocrystalline materials, their properties, different nanomaterials synthesis techniques and their wide applications**.**

As the particles are reduced in size, the collective oscillation of electrons in the conduction band causes changes in the electrical, optical, and magnetic properties. Such phenomena in nanomaterials may play an important role in sensor technology. By exploiting these nanoscale properties a highly efficient chemical sensor can be designed and fabricated[25].

The importance of developing nanostructure sensors is further realized in the device integration. It is expected that the enhancement of selectivity and efficiency of various types of sensors can be achieved by tailoring the size, structure, and shape of the constituent nanomaterials, and ultimately, the device architecture. Recent developments in the area of micromachining, micro-electro-mechanical system (MEMs), and nano-electro-mechanical system (NEMs) engineering provide an opportunity to further develop miniaturized sensor devices. Several major advantages of MEMs and NEMs devices are[26]: (a) packaging or assembling of sensing and signal processing devices in the proximity of the analyte, (b) improved resolution, sensitivity, and superior functionality, (c) low maintenance, (d) better reliability, (e) lower cost due to batch fabrication and (f) wireless data transfer.

The resolution of a sensor is the smallest change it can detect in the quantity that it is measuring. The resolution is related to the precision with which the measurements are made. High resolution and sensitivity of the MEMS device based sensors can be achieved by modulating device architecture. But mainly miniaturized dimension of the device, ability to reach in complex areas, filtering and signal processing are the major parameters that enhances the sensitivity of the sensor even at low concentration of analyte. The type of electrode material and geometry can strongly affect the sensitivity and selectivity. In case of gas sensors, Vilanova et al.[27] have shown that sensitivity increased with electrode positioning when the electrodes were underneath the film, but decreased when the electrodes were deposited on top of the film. If electrode spacing was decreased to less than the film thickness, it was possible to detect a less-reactive gas in the presence of other reactive gas[28]. Tamaki et al.[29] have shown the sensitivities of sensor to dilute NO_2 as a function of electrode gap of MEMS sensor. They[29] have shown that smaller electrode spacing (~10 nm) provided better sensitivity as compared to 150nm electrode gap size sensors. Aging of the MEMS and NEMS devices can also affect the results significantly. Shukla et al. [22] have shown that sensitivity of the doped tin oxide based room temperature hydrogen MEMS sensor drops by an order of magnitude after 1year of aging.

Standard fabrication techniques used in semiconductor industry (Lithographic, Ion milling, CMP,etc.) are typically used for developing the MEMS devices. Author's research group is involved in developing nanoparticle integrated MEMS devices for room temperature detection of hydrogen gas.[30,31] The development of the MEMs and NEMs are also boosted in biosensor research[32], considering our research group also developed the free radicals detection sensor for biological applications.[32] Next section will discuss the motivation of the research topic presented in this dissertation.

1.3. Hydrogen Sensors: Background and Introduction

Hydrogen (H_2) is the most abundant element in the Universe. Due to the rapid consumption of the fossil fuels, much attention has been paid towards H_2 as nonconventional energy source. For example, solid oxide fuel cell (SOFC) technology uses gaseous H_2 for power generation.[33, 34,35] H_2 powered cars and buses are already in normal transit trial service in U.S. cities.[36,37] Liquid H_2 has been used by NASA for launching space-shuttles, figure 1.2. Moreover, H_2 has found applications in electronic, metallurgical, pharmaceutical, nuclear fuel, food, beverages, as well as glass and ceramic industries.[38] Due to the realization of the potential use of H_2 energy further interest has been sparked regarding safe H_2 storage and its transportation.

Depending on the quantities required, H_2 can be transported by road tanker, or pipeline. North America alone has at least a 700 km H_2 pipeline system. NASA uses pipelines for direct delivery of H_2 to space vehicles. However, due to its very small size, hydrogen is the most susceptible for gas leakage; typically about 1-3 Vol % of the H_2 is considered to be explosive. For example, The Hindenburg tragedy and Three Mile Island nuclear power plant explosion[39] that occurred in 1937 and 1979 respectively have been attributed to H_2 related problems. In 1987, *Challenger's* disaster was also related to the hydrogen leak and plausible explosion[40]. In 2002, space shuttle *Atlantis* lift-off got delayed twice due to H leak in the fuel tank[41]. As a result; safety remains a top priority in all aspects of Hydrogen usage and has been the prime motivation for the proposed work. Sensing of H_2 leakage at room or low temperatures has become very essential to avoid any explosion. Current H_2 sensors are not selective and can raise false alarms. Besides, hydrogen tanks without proper sensors can be a potential threat to Homeland Security.

Figure 1.2 Different applications, which demand a selective and highly responsive room temperature hydrogen sensor. (a) car being fueled with H_2 (b)Truck for liquid H_2 storage for space-shuttle launch.

Much focused work is therefore needed in the development of novel sensor materials or in modifying the properties of the existing ones, in order to achieve very high sensitivity and selectivity towards hydrogen, especially at room temperature. In a recent survey by our group, there are various companies (Fuel cell sensor Inc., H2 Scan LLC., Neodym Tech., RKI Instruments, Macurco, Figaro, Applied Nanotech Inc., Enmet Co., Nextech Materials) produce hydrogen sensors which can detect hydrogen gas from 200 ppm to 10 Vol%. Anything beyond 2 Vol% is explosive. Most of the sensor's operating temperature is in the range of 70-100°C, except, the sensor from H2 Scan LLC sensor operates between -20-70°C. These commercial sensors need a heater which can consume more power. The consumption is at around or above 600 mW (e. g. Figaro, Nextech) due to the heating requirement. Also, the reported response and recovery values are in the range of few to 100s seconds, but failed to mention the exact response and recovery times at specific H_2 gas concentration. Selectivity in these sensors is not addressed. In summary, there is a problem in the cross selectivity and sensitivity of these sensors currently available in the hydrogen sensor market. Thus the dissertation attempts to address these scientific issues. Different experimental and commercial sensors based on alternative principles are currently available, but with major drawbacks are summarized in figure 1.3[42].

A great challenge lies in comprehending and establishing a *room temperature sensing mechanism*- a prime motivation of the program. This dissertation has shown the development of novel H_2 discriminating nanocomposite sensors having the following characteristics:

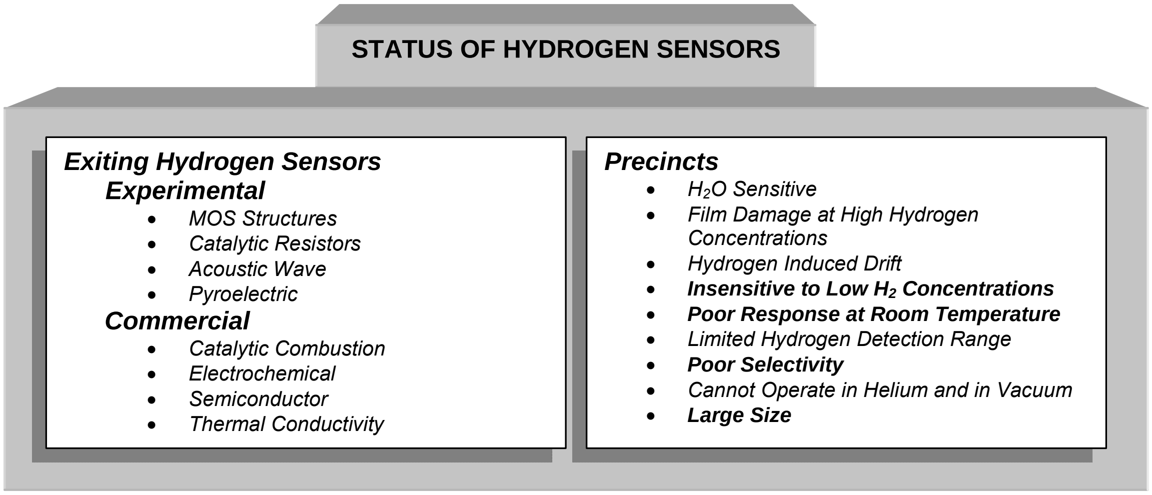

STATUS OF HYDROGEN SENSORS

Exiting Hydrogen Sensors

Experimental

- *MOS Structures*
- *Catalytic Resistors*
- *Acoustic Wave*
- *Pyroelectric*

Commercial

- *Catalytic Combustion*
- *Electrochemical*
- *Semiconductor*
- *Thermal Conductivity*

Precincts

- *H_2O Sensitive*
- *Film Damage at High Hydrogen Concentrations*
- *Hydrogen Induced Drift*
- ***Insensitive to Low H_2 Concentrations***
- ***Poor Response at Room Temperature***
- *Limited Hydrogen Detection Range*
- ***Poor Selectivity***
- *Cannot Operate in Helium and in Vacuum*
- ***Large Size***

Figure 1.3 Charts summarizing the need for an immediate development of hydrogen sensors based on innovative approaches for overcoming the limitations of the current sensor technology and meeting the requirements of the hydrogen based industries.

- Very high hydrogen sensitivity and selectivity
- Low response time and recovery time, robustness, self calibration and cleaning
- Operating at room temperature and sensing hydrogen at ppm level

Considering above mentioned issues as prime target this dissertation evaluates the various aspects of the room temperature based hydrogen sensor and finally developed a prototype device for demonstration. Details about this are explained in next section.

1.4. Organization

This work is part of the current research at UCF funded by National Aeronautics and Space Agency (NASA) regarding the development of room temperature hydrogen gas sensor comprised of nanocrystalline materials integrated into Micro-Electromechanical Devices. This dissertation is divided into two major parts namely, dimensionality effect of the nanocrystalline materials and the MEMS device architecture modulation on gas sensing performance of nano-micro integrated room temperature hydrogen sensor.

The fundamental study of dimensionality aspects of nanocrystalline materials include synthesis of nanocrystalline metal oxides of different materials into different shapes particularly- three dimensions (nano-particles) and one dimensions (Nanorod, Nanotube, nanowires etc.). For synthesis of these materials various techniques such as sol-gel, hydrothermal, anodization and thermal evaporation technique were used.

Second part of this dissertation includes the basic understanding of the sensor design aspects such as length, spacing between the electrodes. We further discuss the theoretical modeling for prediction of sensor performance. Also, integration issues of the nanomaterial with MEMS devices are highlighted. Most importantly testing of the gas sensor corroborates the theoretical predictions of the device. Finally we discuss the development of a hand held prototype device fabrication for hydrogen gas detection.

CHAPTER 2. SYNTHESIS & CHARACTERIZATION OF NANSTRUCTURES

2.1. Introduction

Previous chapter has stressed the importance of the nanostructures and their properties which caused the intensified research for application of the nanostructures in chemical gas sensors. For any type of gas sensors; response time, sensitivity (S), recovery time need to be optimized. Every attribute mentioned above is a function of gas sensing material as well as the device integration. Sensitivity can be controlled by operating temperature, surface area (dimensionality), film thickness, doping and surface catalysis[43]. On the other hand selectivity of the gas sensor can be improved by the surface functionalization, molecular sieves, temperature modulation, and adsorbed gas partial pressure, doping of foreign materials, phase of the nanostrucured materials and varying the work function of the materials[43]. Importance of the nanostrucutred materials over their bulk counterparts stem from the space charge layer (SCL) in enhancing the sensitivity and performance of the device, especially at room temperature.

Formation of the space charge layer occurs when nanocrystalline metal oxides are exposed to air. This phenomenon mainly occurs because of charge neutralization. This results in the formation of an electrical double layer (space charge layer) on the particle surface (shown in figure 2.1), which consists of negatively charged oxygen ions on the surface and positively charged metal ions on the inside[44,45].

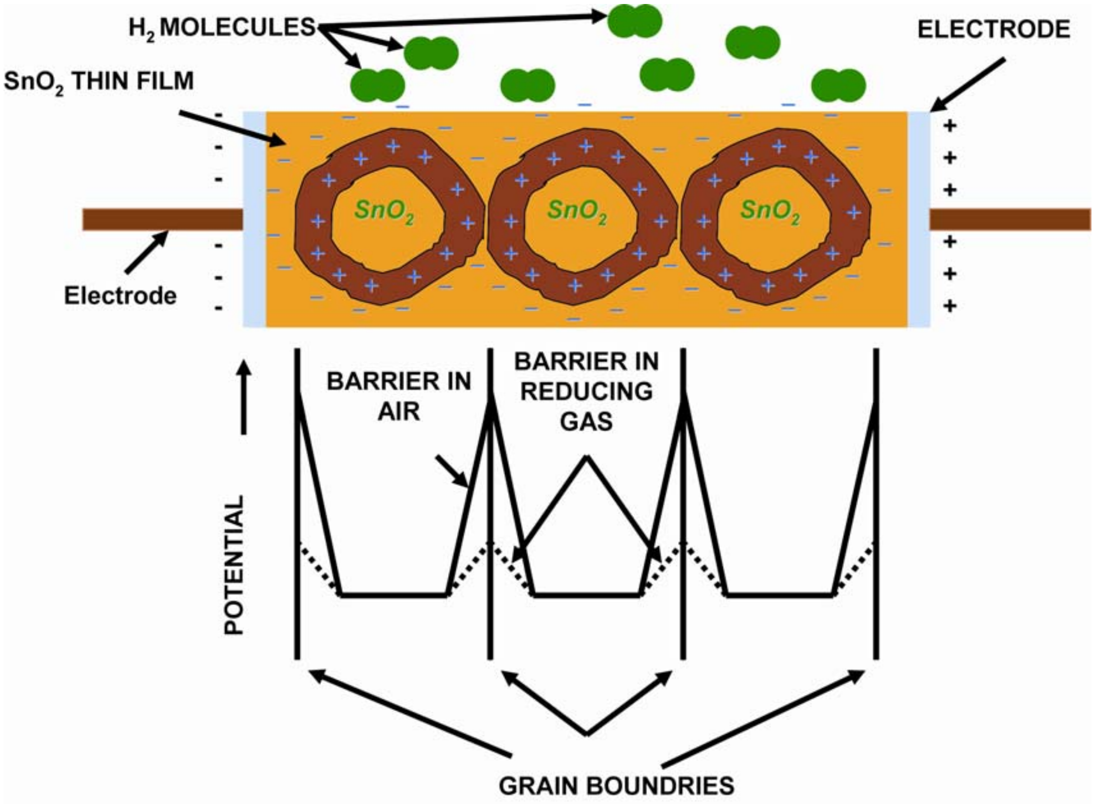

Figure 2.1 Hydrogen sensing mechanism of the metal oxide based gas sensor.[43]

This increases the potential barrier for electron conduction within the film and consequently increases the resistance through the nanoparticles (Ra). When any analyte gas (such as oxidizing or reducing gas) comes in contact with gas sensing material, it reacts with the surface adsorbed species. In case of reducing gases such as hydrogen (H_2), carbon monoxide (CO), analyte gas chemically reacts with surface adsorbed oxygen ions (O^- or O^-_2). This causes the reintroduction of the electrons into the electron-depletion-layer, leading to decrease in the potential-barrier and decrease in the film resistance[46]. In case of hydrogen (H_2), following surface reaction occurs[43]:

$$H_{2(atm)}+O^{-}_{(ads)} \rightarrow H_2O_{(ads)}+e^{-} \quad \text{..................................} \textbf{(2.1))}$$

$$H_{2(atm)}+ {}^{1}\!/_{2}\, O^{-}_{2\,(ads)} \rightarrow H_2O_{(ads)}+e^{-} \quad \text{...........................}\textbf{(2.2)}$$

From the above equation it is clear that as free carrier concentration increases on the sensor surface it increase the conductivity of the gas sensor. The sensitivity is directly correlated to the Debye length (L_D) of the material as follows[43]:

$$S = \frac{\Delta n}{n_b} L_D \quad \text{...}\textbf{(2.3)}$$

Where, Δn is change of number of free carrier concentration in gas sensing material, n_b is charge carrier concentration in bulk SnO_2 and L_D is the Debye Length.

As the size of nanoparticle reduces below twice of the space-charge-layer thickness ($D \leq 2d$), the entire nanocrystallite becomes depleted with the electrons. This result in the distribution of space charge layer through out the nanocrystal and the electrical resistance of the SnO_2 sensor increases abruptly. Under such circumstances the particle size and shape of the nanocrystalline materials determines the overall gas sensing performance. The size and shape of the nanostructured can be manipulated using various synthesis techniques. Precise control over the synthesis method is required to maintain the reliability and repeatability of the product. Hence, the choice of synthesis technique is vital .It has been shown[10] previously that low energy synthesis (e.g. microemulsion) of nanomaterials has resulted in higher oxygen vacancies as compared to the nanomaterials synthesized using high energy (e.g. CVD) synthesis techniques.

The following section discusses the various aspects of different synthesis techniques used in this dissertation for synthesis of different metal oxide based nanostructures

2.2. Tin Oxide

Tin (Sn) is fiftieth element in the periodic table. It belongs to p-block of the periodic table. These elements are more electronegative and softer than the transition metals. Tin is found in the two different oxidation states 2+ and 4+ in oxide form known as stannous oxide (SnO) and stannic oxide (SnO_2). Nanocrystalline oxides of tin usually synthesized using different precursors such as alkoxides and oxidizing different salts. Most stable crystal structure of the SnO_2 is rutile[45] with the following lattice parameter a = 4.373 A and c= 3.186 A. having axial ratio of 1: 0.672. The crystal structure of SnO_2 belongs to the point group of symmetry 4/mm and space group P42/mmm with Sn and O at 2a and 4f positions respectively. Sn to O ratio is 1:2 in a unit cell which means Sn and oxygen has octahedral co-ordination with 4 O and 2 Sn atoms. Oxygen atoms are surrounded by three Sn atoms, which approximate the corners of an equilateral triangle. It was observed that SnO_2 in [110] surface has no net dipole movement making it non-polar[45]. The low axial ratios of centro-symmetric structure was proposed as the reason for reduced ease to form anisotropic nanostructure along <001> direction. This is one of the most investigated materials due to its ease of availability, good chemical, mechanical and physical properties. Most importantly its price gives added advantages over other competing materials for the niche technological applications such as solar cell, liquid crystal displays, surface protective coating and catalytic activities. From 80s it has been widely studied material for gas sensing application.[47,48,49] Earlier various gas sensors made up of micro particulate of tin oxide or micron thick tin oxide films were used for sensor application[50] . Due to recent progress and development in the area of nanoscience and nanotechnology, nanocrystalline form of SnO_2 generated a lot of interest in the scientific community for various applications but mainly for the gas sensor application. SnO_2 based semiconductor type devices have been widely used for the prototype gas sensors for detecting inflammable gases.

It can be found that SnO_2 is one of the most studied materials in all dimensions in the sense of synthesis and fundamental properties evaluations. For gas sensing applications SnO_2 was widely used in the form of nanoparticle thick film,[51,52,53,54,55] thin films[56,57,58] and nanotube and pellets[59,60]. For synthesizing nano SnO_2 various methods has been developed. Mainly, sol-gel[61,62] and hydrothermal [63]. Whatever may be the synthesis technique, the fundamental mechanism of H_2 sensing utilizing nanocrystalline SnO_2 sensor remains the same.

Previous studies from our group have shown successful synthesis and transformation of nano tin oxide using sol-gel method and successful detection of the hydrogen at higher temperatures and room temperature nano SnO_2.[20,30,31]

In the present study, nanocrystalline SnO_2 was synthesized using template assisted mechanism and doped SnO_2 is developed using sol-gel synthesis technique. Thermal evaporation technique was used for synthesizing the SnO_2 nanowires. These nanowires were incorporated in MEMS device for understanding dimensionality aspect (of nano SnO_2) in H_2 detection at room temperature. Next subsections will describe the details about the synthesis of the different SnO_2 nanostructures.

2.2.1. Template Assisted Synthesis of Ordered Nanocrystalline SnO_2 Nanostructures:

This work was performed at the Purdue University (with Dr. H. W. Hillhouse's group) under the collaborative efforts to develop room temperature hydrogen sensor of highly porous nanostructures of templated SnO_2*.*.[64] Surfactant-templated synthesis has proven to be a useful technique in the recent years.[64] Surfactant templating allows very good control over the diameter of the pores and the size of SnO_2 nanocrystallites present in the inorganic wall. Further, the pores are arranged in a 3-dimensional architecture with good interconnectivity between adjacent pores, facilitating the diffusion of the species of interest, such as the gas under detection, through the pore network. Ordered and interconnected nature of the inorganic SnO_2 domain gives added advantage of less charge trapping inside the film. Use of surfactant-templated SnO_2 films in gas sensing has been reported previously.[65, 66, 67] Wang et al.[65] reported hydrogen-sensing properties of cetyltrimethylammonimum bromide (CTAB) templated SnO_2 films.

However, the films lacked long-range order and the sensitivity of the sensors dropped significantly from its peak value at about 300 °C. No room-temperature hydrogen sensing was reported. Shimizu and co-workers[66] have reported synthesis of ordered SnO_2 powders using *n*-cetylpyridinium surfactant and their gas-sensing application. SnO_2 powders reported by Shimizu et al.[66] remain thermally stable up to 600 °C after treatment in phosphoric acid. However, the authors did not report hydrogen sensing performance at room temperature. The sensitivity is the highest at about 300 °C and drops sharply on either side of the maximum. Wagner et al.[67] report sensing performance of SnO_2 thin films for carbon monoxide, another reducing gas, also with CTAB templated films. The films had a disordered nanoporous structure. Template removal was done only at 350 °C, and no information about the crystallization of the inorganic wall was reported. CO was monitored by measuring the conductance of the films in 'humid synthetic air' at 300 °C. The sensors showed up to 250% increase in conductance upon exposure to 5 ppm CO and were reported to be insensitive to background water vapor concentration. However, sensing results only at 300 °C were reported. Most of the literature reports on gas sensing using ordered SnO_2 is plagued by the following shortcomings: the as-made hybrid inorganic-organic nano-composites suffer from a lack of thermal stability and agglomerate during calcination, resulting in crystallites that are significantly larger than 10 nm. Calcination at low temperature (300 °C or so) can remove the template and create pores, but the inorganic wall remains amorphous at this temperature. The semiconducting properties of SnO_2 depend on its crystallinity and in general amorphous SnO_2 based sensors show a poor response. Most of the sensors reported in the literature also require higher operating temperatures (in the range of 100 - 600 °C), thus making a heating element necessary and rendering the sensor architecture more intricate and more energy-intensive. Also at high operating temperatures, the size of SnO_2 nanocrystallites may not be stable due to the possibility of sintering. Even small variations in the size of SnO_2 nanocrystallites (size greater than 25nm) can drastically affect its receptor and transducer functions, and may reduce H_2 sensitivity and the overall sensor life[22]. This shows the importance of precision control of nanoparticle size and shape tight control over synthesis process Template assisted synthesis can give uniform size and shape of the particle. In the present study, synthesis of SnO_2 nanoparticles was carried out using template assisted method.

Details of the synthesis of template assisted SnO_2 thin films are mentioned in the appendix section. In short, stoichemetric amount of tin chloride ($SnCl_4$) in D.I. water was mixed ethanolic solution of triblock co-polymer (pluronic F127, Sigma Aldrich Inc.). The synthesis was carried out at room temperature and thin films of the solution were coated on the substrate (in this case it is MEMS devices) and consequently fired up at around 650C for 24hr[64].

2.2.2. Synthesis of In doped Tin Oxide using Sol-Gel Technique

Sensitivity and selectivity of the nano SnO_2 can be manipulated by doping specific materials in the matrix. Various studies have shown the doping of different cations for detecting H_2, CO, NO. Since the oxidation state of the SnO_2 is four, doping bivalent and trivalent impurities such as (In^{3+})[68], (Cu^{2+})[69], (Zn^{2+})[70] can result in the generation of large number of oxygen vacancies by substitution on a tin lattice site, which in equilibrium expects a 4+ charge to occupy the lattice site. This happens because a 2+ or 3+ on a 4+ site makes the tin site feel a negative charge. To compensate, an oxygen vacancy will form which causes the previous oxygen site to experience a positive charge. This charge compensation will do multiple things within the SnO_2 structure which enhance its gas sensing abilities. *First,* possible modification of the magnitude of the space charge layer is achieved by changing the free carrier density in the space charge region of the structure. *Second*, an increase in surface oxygen vacant sites may help surface dissociation reactions of gases to have immediate access to a site for electron injection. *Third*, trivalent doping increases the number of intermediate energy levels created in the forbidden region of SnO_2. This increases the conduction at room temperature by reducing activation energy.

Doping of foreign atoms in the gas sensor material can increase sensitivity of the gas sensor by manipulating the space charge layer of the nanocrystalline materials especially at the reduced operating temperature (less than 100C). Thin films of the In doped tin oxide were synthesized using following steps. A 50 ml sol of tin (IV)-isopropoxide ($Sn[OC_3H_7]_4$) (10 w/v %) in iso-propanol (72 vol. %) and toluene (18 vol. %) was mixed with 6.5 wt %indium(III)-isopropoxide ($Sn[OC_3H_7]_3$) (0.69 gm) and was allowed to stir for one hour while being covered with a paraffin film. Then sensor device protected with residue free tape (3M Inc., Cleanroom high temperature ESD tape 1258) on the pads was dip coated (20mm /min) twice. The device was heated for 15 min at 120C in a vacuum oven [Fisher Scientific vacuum Oven Model 280A] to dry. It was followed by a 15 sec. deposition of platinum (Pt) film (about 15-20Å thick) using sputter coater [EMITECH Inc., K 500X]. The sample was then heated at 400C for 1hr in a closed furnace [Barnstead Inc, 4800 series] (ramp rate 30C/min) in air. For synthesizing the SnO_2 nanoparticles a small amount (~5 wt%) of polymer, Hydroxypropyl Cellulose (HPC), was added to control the grain size during the gelling reaction[71]. The sol was exposed to air for self hydrolysis and stirred until gelling was completed (~24hr.) The gel was then dried at 150°C for one hour. The amorphous SnO_2 powder formed was calcinated at various temperatures (400 to 1000 C) for 1 hour to achieve crystallization. Synthesis of thin film or nanoparticle using the above described methods results in polymerization and condensation reaction[71]:

$Sn(OC_3H_7)_4 \rightarrow Sn(OH)_4 + 4C_3H_7OH$ (at 25° C)……………………………(2.4)

$Sn(OH)_4 \rightarrow SnO_2$ (amorphous) + $2H_2O$ (at 150° C)……………………..(2.5)

SnO_2 (amorphous) $\rightarrow SnO_2$ (crystalline) (at 400° C)……………………(2.6)

Synthesis route for the doped and undoped SnO_2 particles is shown in figure 2.2..

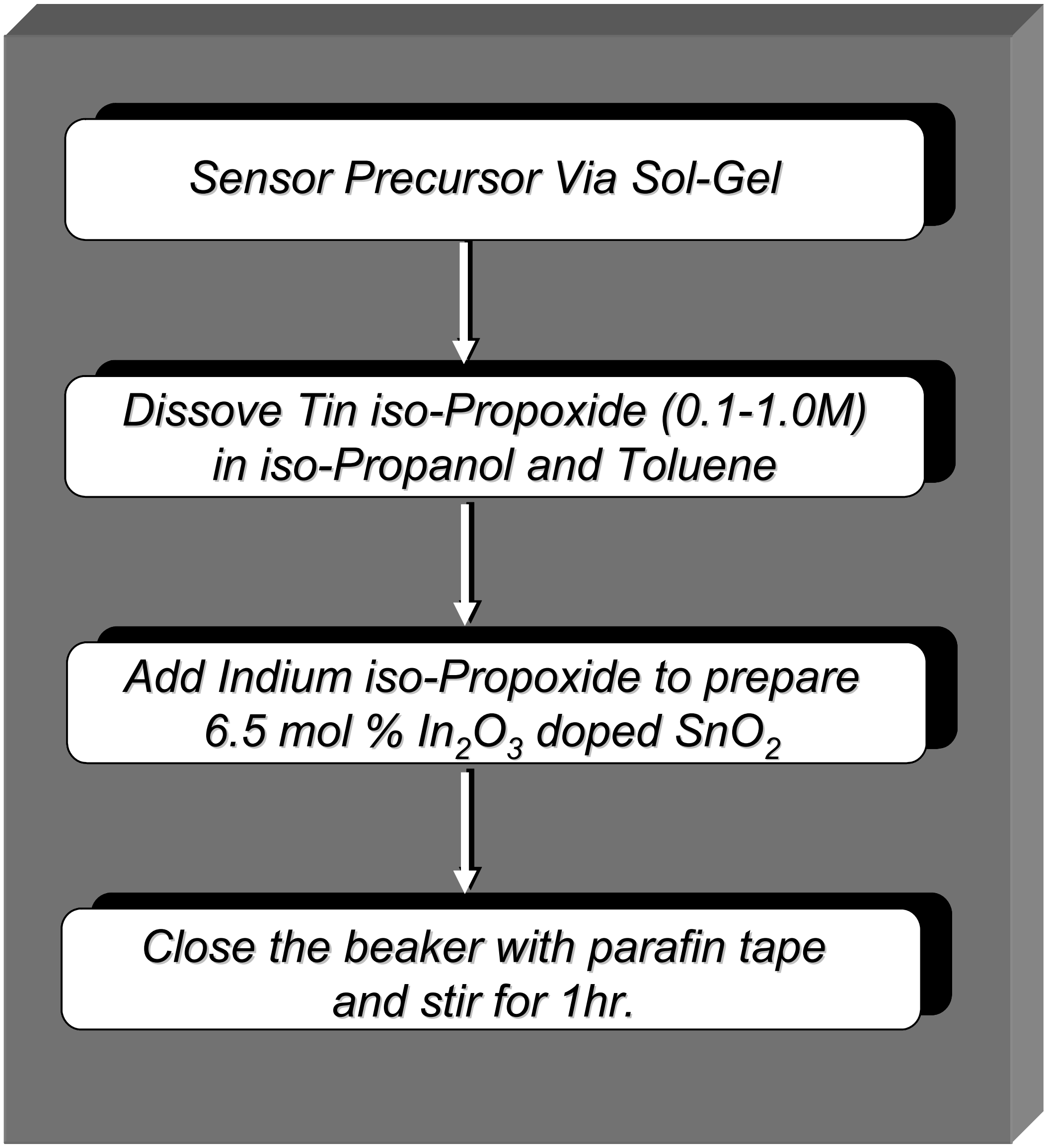

Figure 2.2 Flow chart showing sol-gel synthesis of sensor precursors.

Both phase transformation and particle size variation of the doped SnO_2 particles were studied using X-ray Diffraction (Rigaku Model) with a Cu-$K_{\alpha 1}$ radiation and optimized operating conditions of 30mA and 35kV. The scan rate was 2.5 degree/min with a step size of 0.05 degree. Figure 2.3 shows the spectra from the sample of ITO calcinated at 400°C which show the crystalline nature of the nano Indium doped tin oxide. Dominant peaks at (110), (101), and (211) confirms the cassiterite structure of nano tin oxide. The (110) plane is the most stable of the low index faces[45]. Cassiterite is the most stable phase of SnO_2 with (110) plane as the preferred growth plane, performs best in gas sensing applications [72] . The surface morphology of the nanoparticles were determined by High Resolution Transmission Electron Microscopy (HRTEM) [Philips (Tecnai series)] operated at 300kV accelerating voltage. Figure 2.4 shows the HRTEM images of the In doped SnO_2 particles calcined at various temperatures.

To summarize, indium doped tin oxide nanoparticles and thin film coatings were created successfully using sol gel technique. The characterization of powders using XRD and TEM shows the particle size as well as the crystalline nature of the nanoparticles. Porous nano tin oxide was synthesized using surfactant assisted template based methods and were tested for sensing performance.

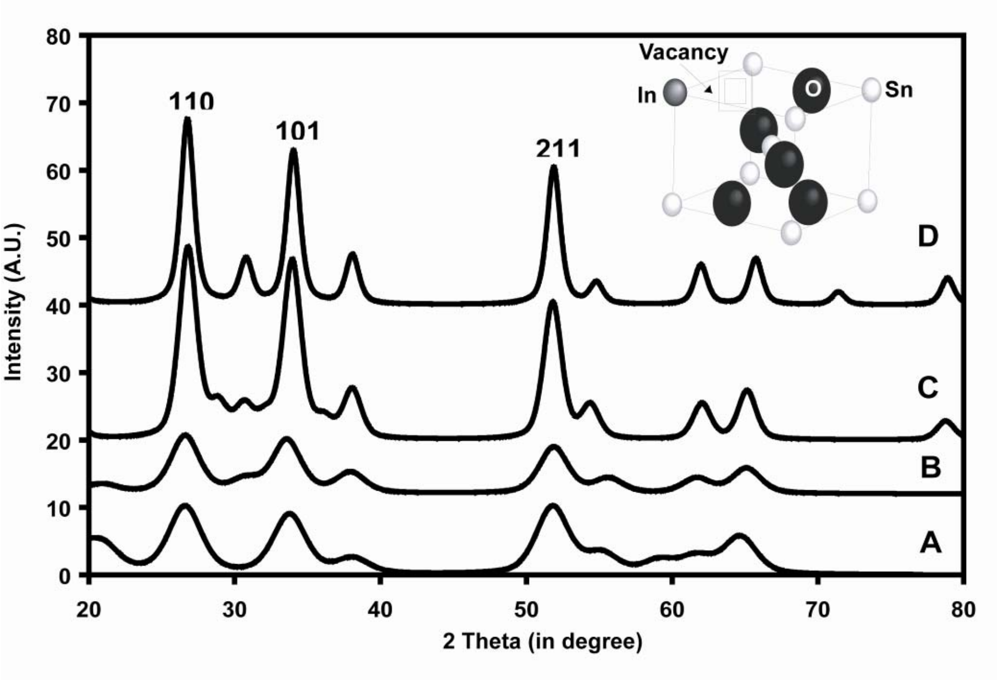

Figure 2.3 X-ray diffraction pattern of In doped SnO_2 samples synthesized at different temperatures (a) 400 C, (b) 500C , (c) 600 C and (d) 700 C. Figure shows the (110) is preferred growth plane of the doped SnO_2 nanoparticles. Inset showing crystal structure of SnO_2 having *vacancy*[45]*.*

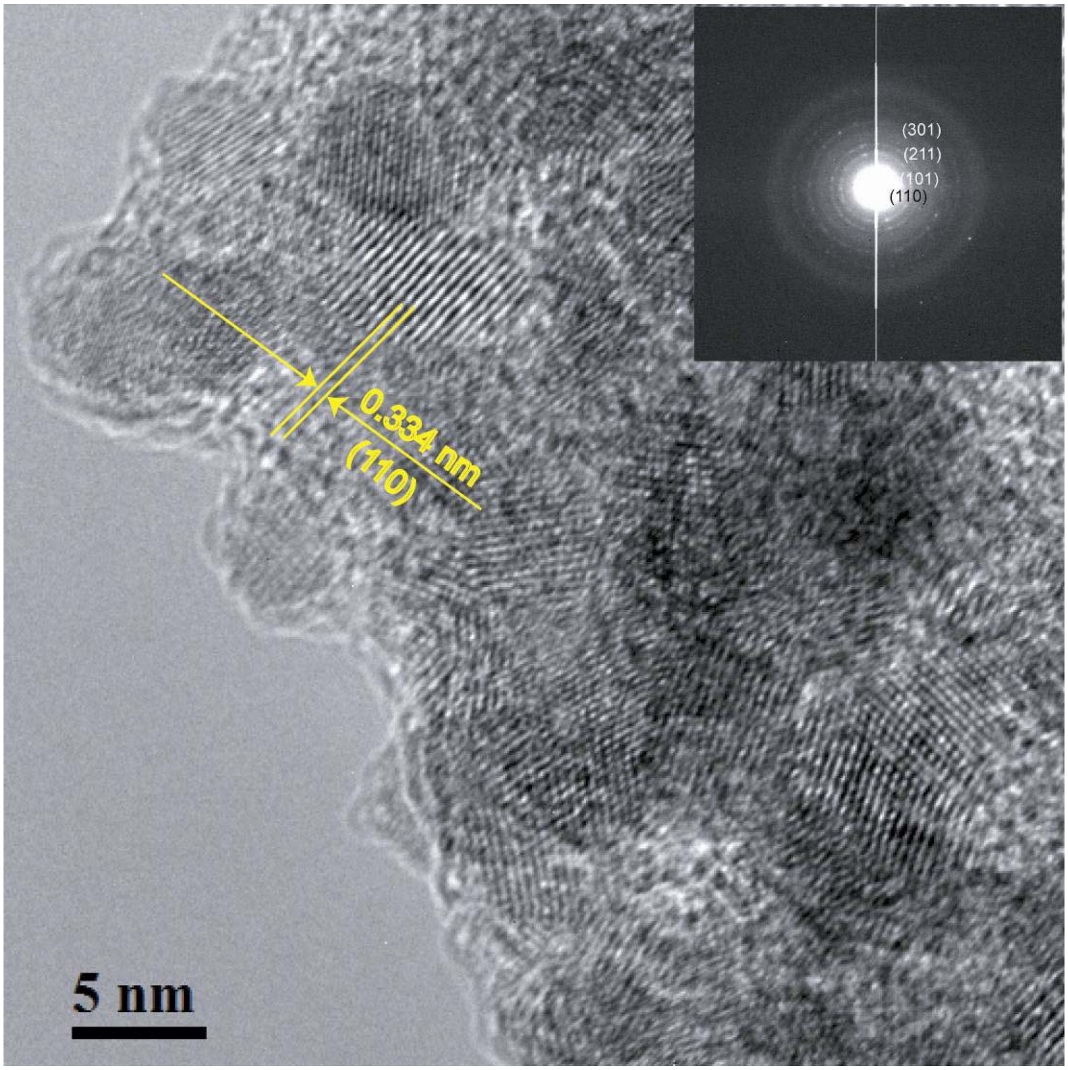

Figure 2.4 Transmission electron Microscopy image of the In doped SnO2 nanoparticles synthesized using sol-gel synthesis method. Inset showing Selected Area Diffraction (SAED) pattern of the In doped SnO_2, confirming rutile structure of the tin oxide.[45]

2.2.3. Synthesis of SnO_2 Nanowires using Thermal Evaporation Technique

As mentioned in earlier sections, 1-D nanostructures such as nanowires, nano fibers or nanotube have high surface area as compared to any other nanostructure morphology. This large surface area of 1D nanostrucutres facilitates higher gas adsorption, reaction and reduced average path traveled by the free carriers rendering them as best candidates for gas sensing application. Nanotubes are considered to be one of the better candidates for gas sensing application than the nanowires since the nanotubes are hollow resulting in higher surface area. Nanowires are solid in nature with diameter less than 100nm but their length can be up to several microns.

High density of atoms at the surface of the particles as compared to bulk results in the higher charge carrier concentration, lowering the resistance of the nanowires as compared to the nanoparticle or thin film counterpart[73] due to this it has been predicted that individual nanowire based sensor will show lower sensitivity as compared to the thin film based sensors. However, by sacrificing some gas sensitivity, response time can be reduced to few seconds, as reported in the literature to milli-seconds[73].

Various techniques such as hydrothermal[74], microemulsion[75], electro-spinning[76] and thermal evaporation[77,78] have been mentioned in the literature for synthesis of SnO_2 nanowires. Thermal evaporation was the most studied and simple technique for the development of 1-D structures of the tin oxides. Ease of synthesis and integration of the thermally grown 1-D nanostructures with MEMS device and possible manipulations are the key aspects for the selection the thermal evaporation technique[79]. Kolmokov *et.al.*[79] have shown the development of the Field Effect Transistors (FETs) of the SnO_2 for gas sensing applications.

2.2.3.1. Experimental

In thermal evaporation technique, usually lower oxidation state of oxides is used as precursors which consequently stabilized by reducing Gibbs free energy by converting to higher oxidation state during heating. For synthesizing the SnO_2 nanowires in present study horizontal tube gas furnace [CM Furnace Inc., Rapid Temp Moldel 1706 FL] was used. Predetermined quantity (~ 5gm) of stannous oxide (SnO) was placed in the area of highest heat flux inside the tube furnace. The Si substrate with thermally grown oxide (thickness~1500A) was coated with noble metal such as silver, gold or platinum using sputter deposition and placed subsequently at approximately 2" distance form the powder. For creating an inert atmosphere, Argon (Ar) gas was blown into the furnace (at rate of 35 CFPH). For rest of the experiment flow of Ar gas was maintained at 20 CFPH. The furnace was programmed to ramp up to a set temperature of 900^{o}C with rate of 3^{o}C/min and hold at a set temperature for 120 min followed by cooling down to room temperature at a rate of 3^{o}C/min.

The structural and morphological evolution of as synthesized SnO_2 nanowires was studied using High-Resolution Transmission Electron Microscopy (HR-TEM) using Philips Technai TEM and the scanning electron microscope (SEM) (JSM-6400F, JEOL, Tokyo, Japan).

2.2.3.2. Effect of Catalyst Coverage on Nanowire Dimensionality:

Typical SEM images of the as synthesized SnO_2 nanorods are presented in Fig. 2.5 (inset) as Pt sputtering time is increased from 30 sec to 120 sec respectively, which effectively varies the Pt catalyst size at the evaporation temperature. Randomly oriented, straight and long rods, as long as 50 µm, are formed under these processing conditions. From figure 2.6 it can be concluded that the Pt sputtering time can affect the diameter of the nanowires. Increase in Pt sputtering time (depositing thicker Pt film) results in formation of large size Pt nanoparticles which subsequently act as a nucleation for the nanowire formation.[80]

2.2.3.3. Mechanism of SnO_2 Nanowire Formation

Figure 2.6 (a-b) shows TEM images of a SnO_2 nanowire with a diameter ~25nm. High resolution image of SnO_2 (Figure 2.6) indicates the formation of SnO_2 nanorods without any catalyst particle at the tip. In the present study, nanorod growth occurs via vapor-solid (VS) mechanism (also known as 'oxide-assisted-growth' mechanism)[81] Nano and submicron SnO_2 rods have been synthesized using thermal evaporation process. It is important to clarify here that the terminology used for the description of these nanostructures is rod and not nanotube or nano fibers. Nanotubes are hollow while fibers are flexible. Author's group earlier successfully reported the SnO_2 nano fibers using electro-spinning technique.[76]

In the presence of a catalyst particle, such as Pt, the nucleation and growth of the SnO_2 rods via thermal evaporation process take place via vapor-liquid-solid (VLS) or vapor-solid (VS) mechanism.[80] VS mechanism is also widely known as the oxide assisted growth mechanism[80]. In VS mechanism, formation of the vapor phase of subsequent oxides and its transportation to the substrate plays a key role.

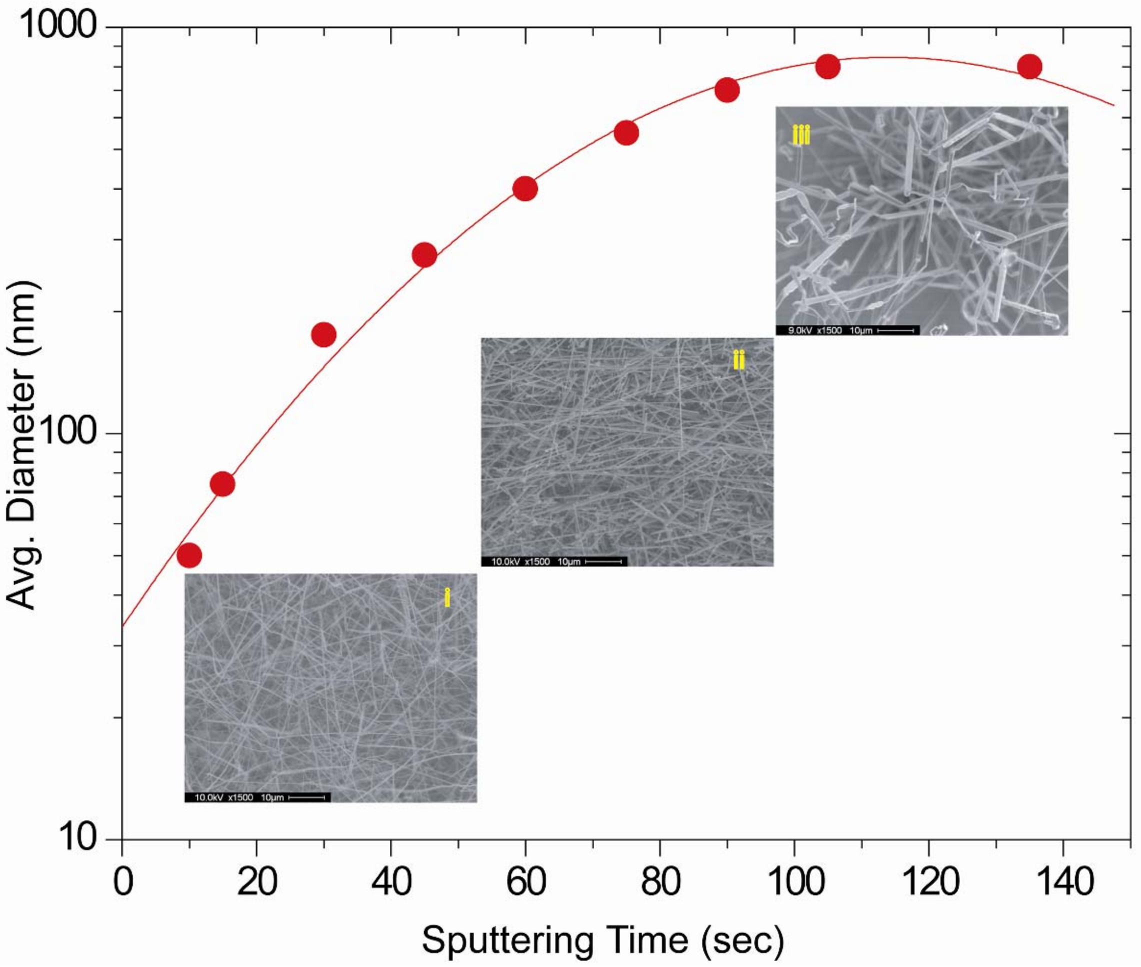

Figure 2.5 Effect of platinum sputtering time on the nanowire diameter. Inset showing SEM images of the nanotube on SiO_2 substrate for platinum sputtering time (i) 15 sec., (ii) 45 sec., (iii) 90 sec.

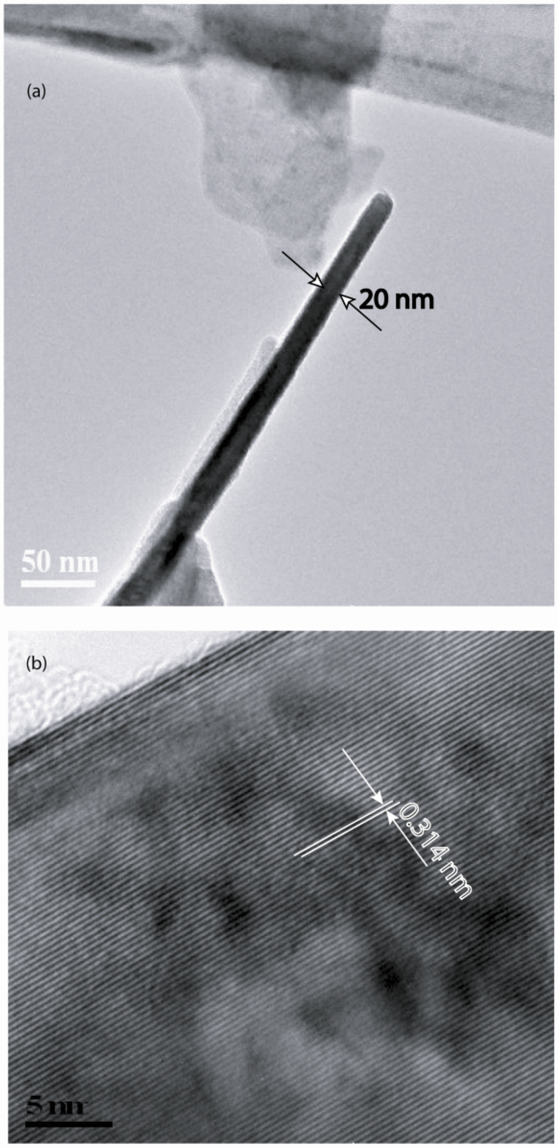

Figure 2.6(a-b) High Resolution Transmission Electron Microscopy (HR-TEM) images of the thermally grown SnO_2 nanowires.

The following chemical reactions are likely to occur at the operating temperature of 900 °C[82]:

$2SnO \rightarrow Sn + SnO_2$………………………………………………………………… (2.7)

The Sn and O atoms are transported to the Pt sputtered substrate. The platinum film on the substrate gets converted into the dispersed Pt nanocrystalline particles resulting in the formation of Sn-O-Pt alloy. These alloyed nanostructures act as nuclei for the nanorod formation. During the formation of nanorod, defects such as point defects or stacking fault play important role in one-dimensional growth. Surface energy plays an important role in nanowire growth. It is known that surface energy is more important when the crystal size is reduced to the nanometer scale.[83] After coming in contact with the substrate containing dispersed Pt nanocrystalline particles, the Sn and O atoms, carried by the Ar gas, may get dissolved into the Pt nanoparticles forming Pt-Sn-O alloy nanoparticles. After reaching the solubility limit, further dissolution of Sn and O atoms from the vapor phase into the liquid Pt-Sn-O nanoparticles, results in the phase separation in the form of precipitation of SnO_2 nanorods. Being in the molten state, the Sn-rich Pt-Sn-O catalyst nanoparticles remain on the top of the precipitated SnO_2 rods. The molten Pt-Sn-O alloy particle, possibly solidifies as the furnace cools below the melting temperature of the particle. This VS growth mechanism should then result in the formation of SnO_2 rod with a catalyst particle at its tip[80].

2.3. Titanium Oxide

Titanium (IV) oxide (TiO_2) also widely known as Titania is one of the oxide forms of the metal titanium. Nanocrystalline form of TiO_2 is widely synthesized and studied[84,85]. Anatase phase of nano- TiO_2 have the most interesting properties as compared to the other two phases[86]. Band gap of nano TiO_2 is 3.2 eV because of which it is widely used in various applications such as solar cell, anti-fogging windows, cloth and paper industries and UV absorber in sun screen lotions[84]. Barnard et.al. have mentioned that phase transformation of nano titania can be manipulated by changing the surface chemistry.[87]

TiO_2 nanoparticles are widely synthesized from organo- metallic (alkoxide) precursors of titanium[88] While TiO_2 nanotubes,[89] nanowires,[90,91,92] nanorods[93] and nanobelts[94] have been synthesized using various different titanates. In the present study different dimensions of TiO_2 were synthesized using sol-gel technique while one dimensional nanostrucutres were synthesized using hydrothermal and anodization techniques explained in detail in the following sections.

2.3.1. Synthesis of TiO_2 Nanoparticles:

A polymeric, sol–gel route (shown in figure 2.7) was used to prepare the metal oxide nanoparticles. For synthesis of TiO_2 sol, 7.5 ml of titanium isopropoxide (Aldrich Inc.) was added in the 50 ml of Anhydrous Isopropanol (Aldrich Inc.). To slow down the hydrolyzation of the alkoxide, a complexing agent, acetylacetone (AcAc, from Aldrich Inc.) 5 ml was added as a stabilizer. After stirring for 2 hr, 5 ml of D.I. water was added to hydrolyze the titanium isopropoxide. Finally, a yellow clear sol was achieved. The sol was aged for 12 hrs and then dried at 100 °C for 4 hrs in air (in Fisher scientific vacuum oven Model 280A) which causes the removal of OH from the gel system, with simultaneous collapse of the gel structure. Figure 2.8 (a) shows the TEM image of sample after sol-gel treatment. Figure shows the amorphous nature of the sample.

These amorphous TiO_2 powder was calcined at 400C for 1hr. for crystallization. Following reaction at

$Ti(OC_3H_7)_4 + 4H_2O \rightarrow Ti(OH)_4 + 4C_3H_7OH$ (at 25° C) …………………(2.8)

$Ti(OH)_4 \rightarrow TiO_2$ (amorphous) + $2H_2O$ (at 100°)…………………………(2.9)

TiO_2 (amorphous)→ TiO_2 (anatase) (at 400° C)…………………… …(2.10)

Figure 2.8 (b&c) shows the TEM image of the sample calcined at 400C. Figure shows the crystalline TiO_2 samples having about 5 nm particle size. XRD analysis (figure 2.9(a)) confirms the anatase phase of the TiO_2 samples.

2.3.2 Synthesis of TiO_2 Nanotubes using Hydrothermal Method

Synthesis of hydrothermal nanowires is done using method described in the literature[95,96]. In short, the TiO_2 nanoparticles used for nanotube production were synthesized using the method explained above in section 2.3.1. 0.5 g of the TiO_2 nano powder, ~ 5 nm particle size (see figure 2.8 (c)) was mixed with 25 ml of 10N NaOH solution and thermally treated at 110°C in a Teflon-lined autoclave for 24 hr. After the hydrothermal treatment, the precipitate was filtered and washed using DI water five times (pH ~9). Further neutralization was achieved by washing in 0.1 N HCl solution (until pH of the solution reaches ~7). Powder was separated by centrifugation (2500 RPM for 5 minutes) and dried at 100 °C for 2hrs in air (in Fisher scientific vacuum oven Model 280A). The dried powder was calcined at 400°C for 1 hr in air (Barnstead international bench top muffle furnace 4000 series) which leads to the formation of anatase TiO_2 nanotubes (as shown in figure 2.8 e and XRD in figure 2.9 c)

2.3.3 Formation Mechanism for Hydrothermally Prepared TiO_2 Nanotubes:

Titania nanotube formation from hydrothermal treatment had been widely debated in the open literature and the mechanism has been studied[95,96],[97] using various parameters such as temperature, initial size of TiO_2 nanoparticles, processing time and pH of cleaning solution (post treatment). As the TiO_2 nanoparticles (shown in figure 2.8 (b&c) reacts with sodium hydroxide to form chains of distorted TiO_6 octahedra in which each titanium is surrounded by six oxygen ions[98] In this arrangement two of the Ti-O bonds are longer (0.1980A) as compared to other four Ti – O bonds (0.1934A).It was hypothesized[98] that treatment with sodium hydroxide breaks only the longer Ti – O bonds leading to the formation of nanosheets of sodium titanate ($Na_2Ti_2O_4(OH)_2$). The reaction between the titania and sodium hydroxide was proposed as:[90,96]

$$2\,TiO_2 + 2NaOH \rightarrow Na_2Ti_2O_4\,(OH)_2 \quad \text{..................................} \mathbf{(2.11)}$$

The cartoon diagram representing the layered nano sheets of sodium titanate and hydrogen titanate is shown in figure 2.10. During the formation of sodium titanate nanosheets, sodium ions are attached with oxygen atom of titania while hydroxyl groups are attached to the titanium as shown in figure 2.10 (a). A simple cation exchange reaction between sodium and hydrogen takes place upon washing with dilute HCl (0.1N) leading to the formation of hydrogen titanate as shown in figure 2.10 (b)

During washing, the exchange reaction between Na^+ and H^+ follows the equation shown below (equation # 2.12). It is believed that the initial nanotubes formed are composed of sodium titanate and their subsequent washing with acidic solutions (in present study washing solution pH~ 2) leads to the replacement of sodium with hydrogen leading to formation of $H_2Ti_2O_4\,(OH)_2$.

$$Na_2Ti_2O_4\,(OH)_2 + x.H^+ \rightarrow Na_{2-x}H_xTi_2O_4(OH)_2 + x.Na^+ \quad \ldots\ldots\ldots\ldots\text{.. (2.12)}$$

Where x is between 0 to 2 and depends on the pH of the medium.

A further heat treatment of this hydrogen titanate nanosheets leads to dehydration of the sample and formation of TiO_2 nanotubes[90,91].

$$H_2Ti_2O_4\,(OH)_2 \rightarrow 2TiO_2 + 2H_2O \quad \ldots\ldots\ldots\ldots\ldots\ldots\ldots\ldots\ldots\ldots\ldots\ldots\text{ (2.13)}$$

In present study, morphological evolution of nanosheets of hydrogen titanates was confirmed by the TEM analysis (fig 2.8 d) The XRD data in figure 2.10(a) confirms the presence of hydrogen titanate after 5 times washing (using acidic solution with pH~2) of powder obtained after hydrothermal treatment of TiO_2 nanoparticles for 120°C for 24 hr. XRD shows dominant peaks at (200), (102), (310) (311) confirming monoclinic structure of the hydrogen titanate sample.

The effect of the pH of washing solution was further explored by Teng et.al.[99] They have mentioned that pH of 5.5 leads to 5 % retention of sodium in the nanotubes. But, selecting pH of washing solution between 0.5 to 5 sodium free nanotubes can be obtained. In the present study, XRD analysis of hydrothermally treated powder after washing shows the presence of only hydrogen titanate (figure 2.10b). The powder was washed with solution having pH 2.0. This will remove all the sodium from the titanate (XRD in figure 2.9 c shows no sodium titanate or sodium hydroxide peaks). Absence of reflections (110) [at 2 Θ = 16.01), (200) [at 2 Θ = 27.53] as well as (600) [2 Θ = 61.98] and (431) [2 Θ = 63.73] in XRD spectra (shown in figure 2.9 b) confirms the absence of sodium titanate.

In this study, hydrogen titanate was heat treated at 400°C for 1hr (to retain nanotube shape as well as anatase phase of TiO_2 nanotubes for gas sensor application). The X-ray diffraction data in figure (2.9 c), after this treatment, confirms the formation of anatase titania nanotubes. Morphological evolution of TiO_2 nanotube observed in present study authenticates the model proposed by Zhang et.al[98] for TiO_2 nanotube formation mechanism using hydrothermal synthesis.

Lan et. al.[12] have highlighted the effect of phase of initial nanoparticles (of TiO_2) can affect the formation of TiO_2 nanowires. They have shown the need of increase in processing time and temperature for hydrothermal treatment if starting nanoparticles have 20% rutile and 80% anatase phase. They also mentioned that coalescence of rutile phase is required for evolution of 100% nanotube In the present investigation precursor TiO_2 nanoparticles have 100% anatase phase (see figure 2.9 a) We have further evaluated the role of hydrothermal treatment temperature on nanotube evolution.. It was found that, increasing processing temperature from 110 C to 150 C leads to the modulation in surface area of the nanotubes .Increase in hydrothermal treatment temperature from 110C to 140 C leads to linear increase in surface area from 232 m^2/g to 400m^2/g. (see figure 2.11). This can be pertained to increase in thermal energy during hydrothermal processing enhanced rupture of O-Ti-O bands and higher diffusion of Na^+ ions in the Ti-O matrix (as shown by Tsai et.al.[84]). This leads to the formation of larger lamellar sheets because of electrostatic repulsion of sodium ions. This could lead to the formation of large sodium titanate nanosheets. Rolling of these large sheets results in higher curvature and multiple layers as shown by Tsai et.al.[84] This further leads to significant increase in the nanotube diameter and reduction in the overall surface area. Figure 2.8 (g) shows the TEM image of sample hydrothermally processed at 150C. It can be interpreted that it is forming the large nanoparticles (as shown in figure 2.8(g)). Such abrupt drop in the surface area due to the morphology variation is also reported in the literature. Hydrothermal treatment at temperature above 140C possibly results higher O-Ti-O bond cleavage which destroy the lamellar TiO_2 structures[84,90]. This leads to formation of elongated nanoparticles rather than nanotubes. This study authenticates the formation mechanism proposed by Zhang et.al.[98] for hydrothermal synthesis of the nanotubes using TEM,XRD and BET analysis.

In summary, nanotubes of TiO_2 were successfully synthesized using hydrothermal synthesis technique. Formation route involves interaction of NaOH with TiO_2 nanoparticles to form sodium titanate which after washing with HCl (pH=2) leads to formation of hydrogen titanate nanotubes. This powder after heating (dehydrating) leads to formation of anatase TiO_2 nanotubes. The section 3.6 explains the process of integration of these nanotubes with MEMS device while the section 4.5 explains the gas sensing behavior of these nanostructures.

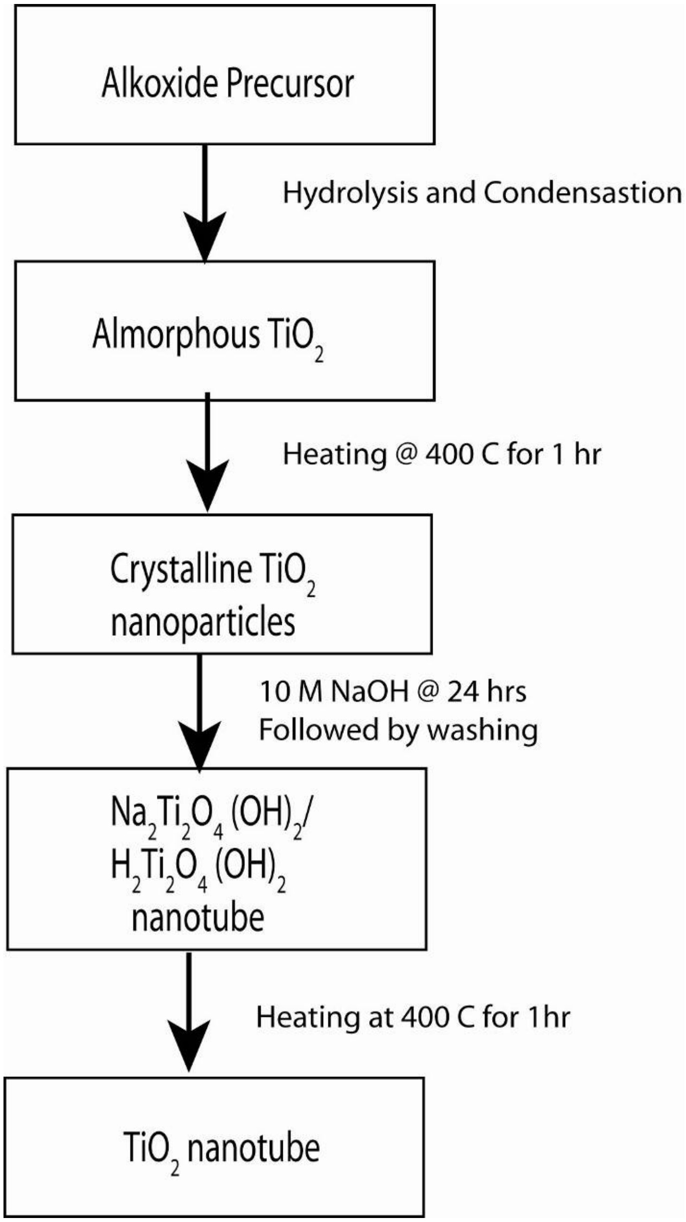

Figure 2.7 Synthesis route for TiO_2 nanoparticles and nanotube

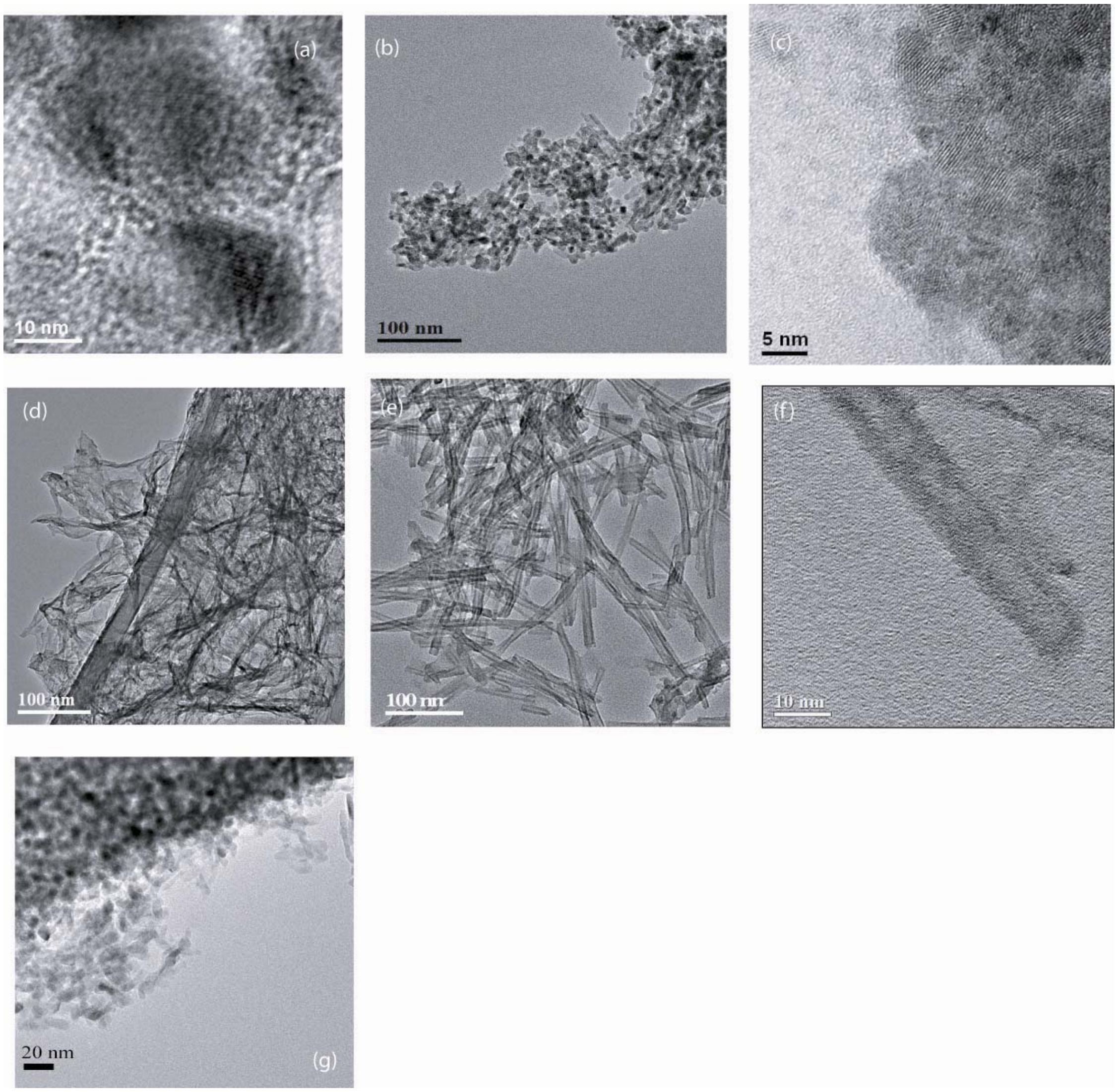

Figure 2.8 Transmission Electron Microscopy Analysis of different TiO_2 nanostructures. (a) as synthesized (amorphous) (b)TiO_2 nanoparticles (formed after amorphous samples calcined at 400 C for 1 hr) (c) high resolution image of TiO_2 nanoparticles showing size of around 5nm. (d) titanate nanosheets (formed after hydrothermal treatment of nanoparticles at 120 C for 24 hr, (e) highly porous TiO_2 nanotube, (f) high resolution image of TiO_2 nanotube showing diameter of around 10nm and pore size around 4nm, (g) sample after hydrothermal processing at 150C.

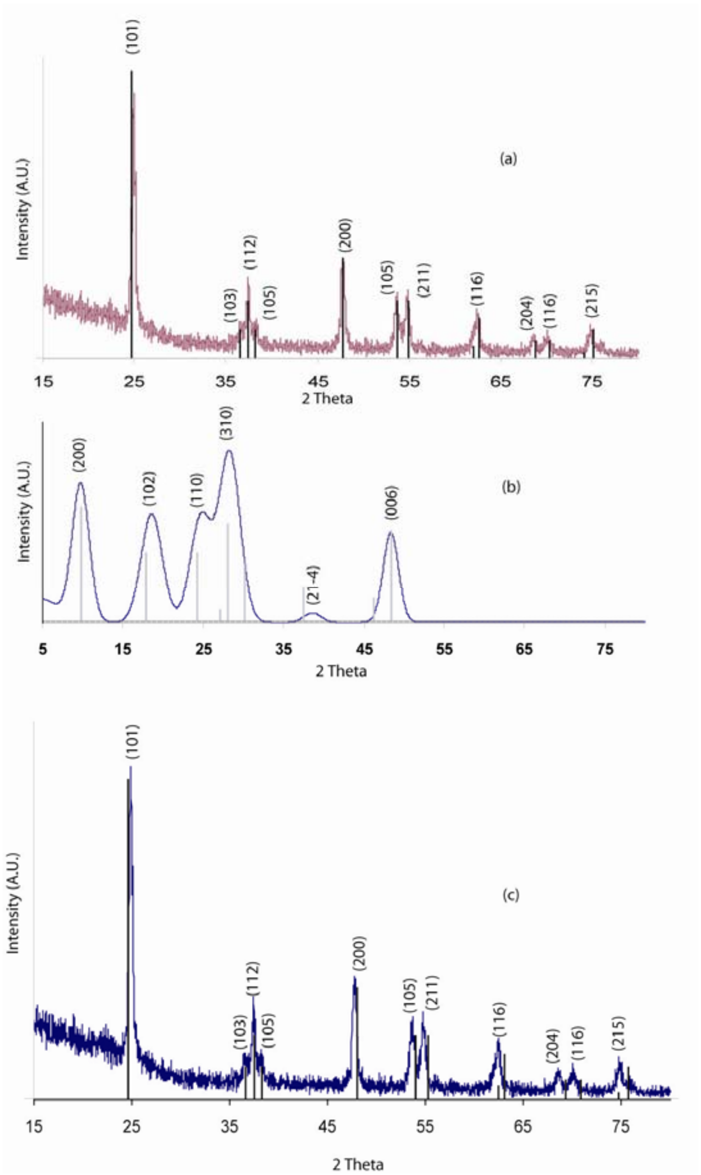

Figure 2.9 XRD pattern of TiO_2 nanoparticles showing anatase phase. Peaks are confirmed using PDF # 00-021-1272 and shown in line in figure; (b) XRD pattern of Hydrogen titanate. Peaks are confirmed using PDF # 00-036-0655 and shown in lines in figure ;(c) XRD spectra of TiO_2 nanotube formed after heat treatment of titanate samples. Peaks are confirmed using PDF # 00-021-1272 and shown in line in figure

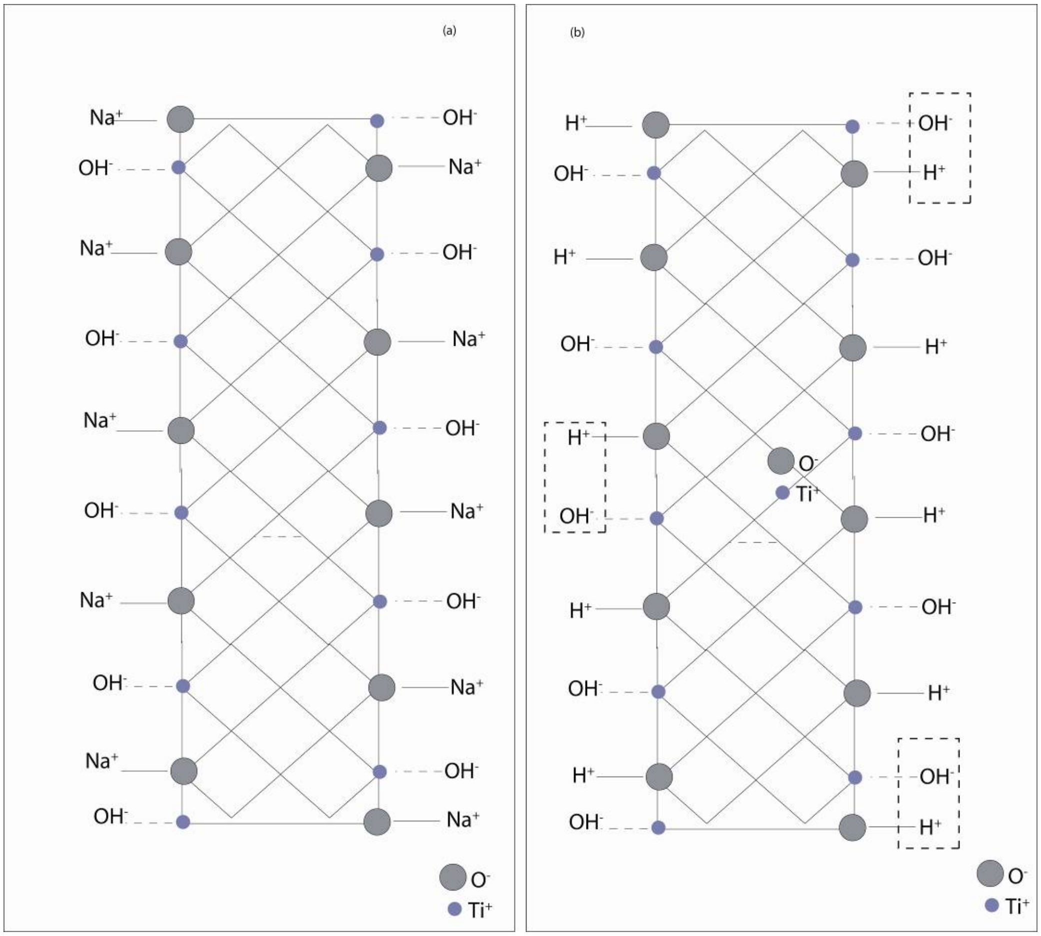

Figure 2.10 (a) Cartoon diagram representing the structure of sodium titanate formed after the hydrothermal synthesis of TiO_2 nanoparticles in 10N NaOH solution at 120 C for 24 hr., (b) Structure of hydrogen titanate nanosheets formed after replacement of Na^+ in sodium titanate by H^+ after washing of sodium titanate sample with HCl solution.

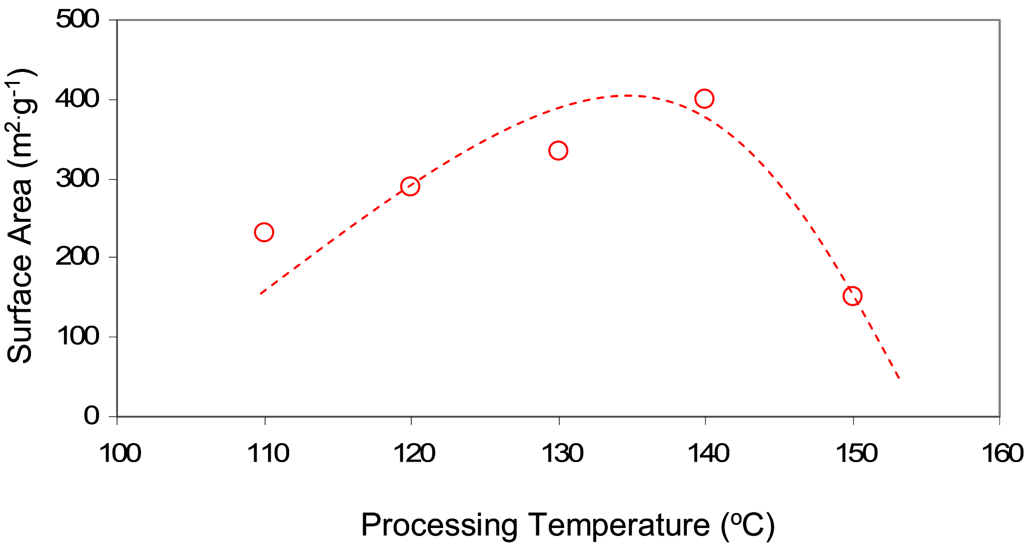

Figure 2.11 Effect of hydrothermal processing temperature on the surface area of the TiO2 nanotubes.

2.3.2. TiO_2 nanotube using potentiostatic anodization

Anodization of the titanium films was achieved using constant voltage conditions (at 15V) Anodization was performed in a standard flat cell using a standard three electrode configuration. The working electrode and the reference electrode were maintained at a distance of 4 inches in a standard flat cell. A 1cm^2 circular surface area of the working electrode was exposed to the electrolyte during anodization. A schematic of the set up is shown in figure 2.12. The working electrode (titanium thin films) was the anode while the platinum served as the cathode (area = 1 cm^2) and silver-silver chloride was used as the reference electrode. The anodization was carried at 15V for 200 minutes using Verastat Multichannel Potentiostat [VSP 03, Princeton Applied Research]. Initial ramping of the potential to the desired 15 V was carried at 10mV/sec followed by the constant voltage conditions for 200 minutes. The electrolyte for the experiments was prepared using 5 Vol% H_2SO_4 [99%, Sigma Aldrich] and 30gm of sodium citrate trihydrate [Sigma Aldrich] in 0.5% solution of potassium fluoride [Sigma Aldrich] in 500 ml of DI water [18.2 MΩ] Anodization for 4hours under constant voltage conditions [15V] then produces the titania nanotubes by field assisted dissolution and penetration of metal oxide into the metallic film.[100,101] Details of the TiO_2 synthesis using anodization is currently under investigation by our research group.

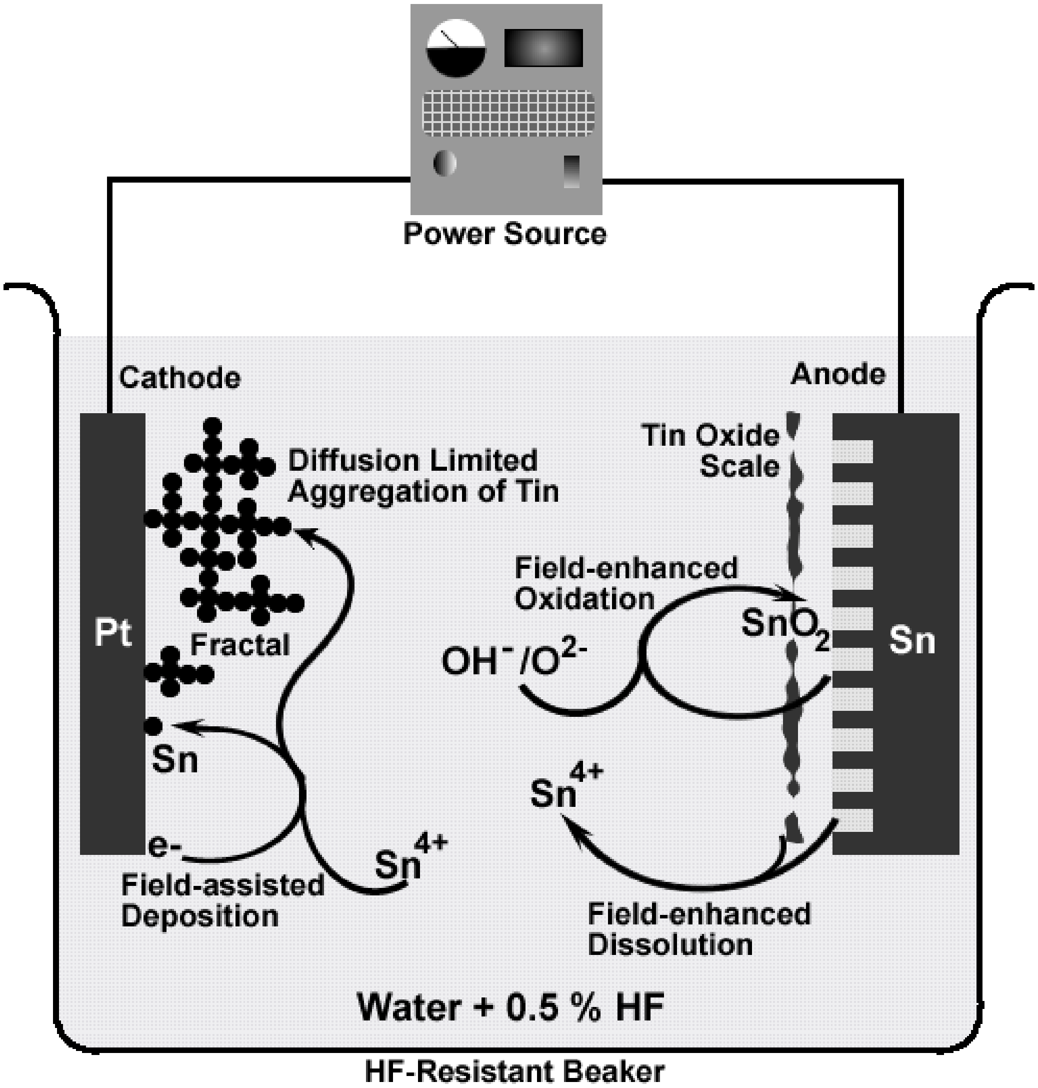

Figure 2.12 A representative picture of anodization technique used for synthesizing high surface area materials.

In summary, this chapter discussed in detail different techniques used for synthesis of nanostructured In doped SnO_2 thin films and thermal evaporation for synthesizing SnO_2 nanowires. The later part of the chapter discussed 1-D nanostructured development of TiO_2 nanotubes using hydrothermal and anodization techniques. Integration of these nanostructures with MEMS devices (provided by Dr. Cho’s group) and details about the hydrogen detection has been explained in details in next two chapters.

CHAPTER 3. MEMS DEVICE DESIGN OPTIMIZATION

3.1. Introduction

Recent development in the technologies like micromachining, micromechanical systems (MEMS) and nano electro mechanical systems (NEMS) provide the opportunity to develop miniaturized sensor devices for the various different sensor applications[102].

A MEMS device based sensor have comprised of various elements such as substrate, electrode and wiring for transferring signal from electrodes to the analyzer. Typical MEMS and NEMS based sensors are developed on the silicon wafers. This is due to the fact that a MEMS device undergoes various thermal and chemo-mechanical processes. Development in the semiconductor industry for chip manufacturing already mastered the process of bulk manufacturing.

Selection of the substrate material for the specific application is a key part in MEMS technology. Substrate on which MEMS device can be patterned should have the following qualities[26]:

(i) Sensor substrate should be chemically inert.

(ii) The substrate material should be mechanically sturdy and should withstand high shocks.

(iii) It should be easily processed and should not affect the sensing film during processing

(iv) It should be readily available and cheap.

Silicon, polymers, glass, silicon carbide and nitrides are the few materials which are widely used for MEMS applications. A typical MEMS device undergoes various fabrication steps. Major steps included are surface barrier layer development, oxidation, patterning of the electrodes, wire bonding.

Selection of the proper material as an electrode material also plays a key role in the sensor response kinetics. Barsan etl.al. [103] have studied the effect of electrode materials towards CO detection. They[103] have reported enhanced sensitivity (~1 order of magnitude) by sensor having platinum electrode as compared to gold electrode. This can be correlated to the contact effects at the sensing layer electrode interface (band bending of nano metal oxide), active participation of metal electrode as catalyst for gas dissociation (spill-over effect) and possible doping at atomistic scale of noble metal resulting the band gap modulation of nano metal oxides.[103] .

Also sensor architecture is another key element in MEMS device based sensor applications. Variation of the MEMS device architecture can result in the faster detection of the analyte, higher sensitivity and selectivity of the gas sensors. In the present work, interdigitated structure of the electrode has been selected. High surface area for sensing, ease to pattern in miniaturized size and minimum charge carrier losses are some of the key features of these types of electrodes. A typical interdigitated architecture of the resistance based MEMs Device is shown in figure 3.1 & 3.2.

Important parameters that define the interdigitated electrode architecture are shown in figure [i.e. finger length (l), spacing (g), width (w) and number of finger]. Modulation of each of the above mentioned parameters can have good or adverse effect on sensor performance.

In the following sections effect of MEMS device architecture modulation has been explained in detail. .

3.2. Fabrication of the Micro Electromechanical Devices

Fabrication of the MEMS devices was done by NanoFab & BioMEMS Lab (Dr. Cho's group)The steps involved in the MEMS device fabrication process are described schematically in Fig.3.1. A 3" silicon (Si) wafer is utilized, which is oxidized at higher temperature to produce an insulating silica (SiO_2) layer.

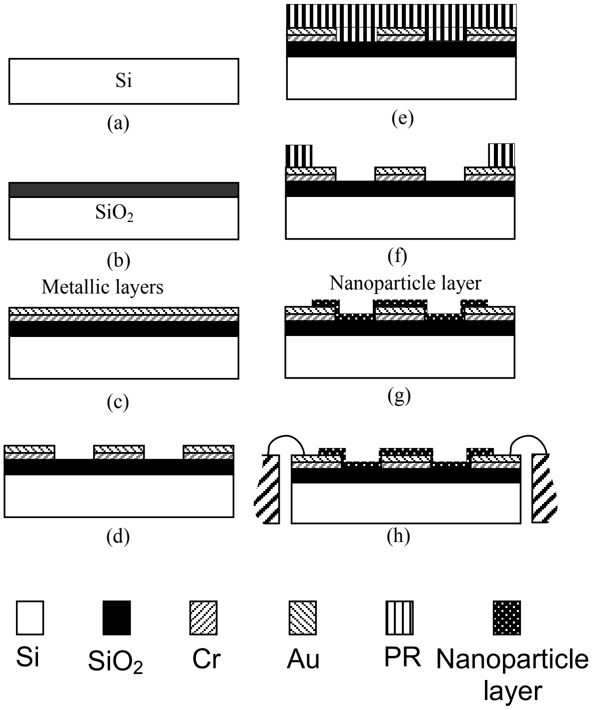

Figure 3.1 MEMS device fabrication steps: (a) cleaning; (b) thermal oxidation; (c) metallic film deposition; (d) photolithography and chemical etching; (e) coating photo-resist as the sacrificial layer; (f) Opening windows; (g) sol-gel dip coating and lift-off; (h) packaging.

During the fabrication, chromium (Cr, 10-20 nm) and gold (Au, 150-200 nm) thin films are deposited by thermal evaporation technique. Four interdigitated sensors are patterned on the substrate using the photolithography and the wet chemical etching techniques (Fig. 3.1). The nanocrystalline materials was dip coated on the patterned MEMS device, which is subsequently wire bonded to the ceramic package for the H_2 sensing tests[104].

A silhouette of the packaged MEMS device is shown in Fig.3.2. Four interdigitated Au electrodes with the electrode distance of 2-20 μm sensor are clearly visible. The integrated circuit (IC) chip with the wire bonded MEMS device is shown inserted in a 32 pin socket assembly. The sensor test-board is designed and laid out using LPKF CircuitCAM 4.0 software and subsequently cut using the LPKF Boardmaster 4.0 software on a single-sided copper clad prototype boards.

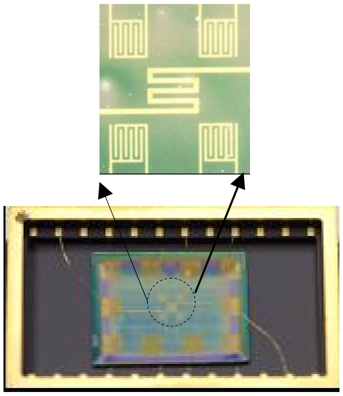

Figure 3.2 Fabricated, coated (with In doped SnO_2) and wire bonded MEMS device for detection of the hydrogen at room conditions.

3.3. Effect of Sensor Device Modulation on the Response Kinetics

The MEMS design parameters related to electrode can affect the gas sensing performance significantly. Electrode parameters such as the number of fingers, spacing and length of electrode fingers, positioning of the electrode (above or below the gas sensing material) and material of the fingers can significantly affect the sensor performance. MEMS device architecture can be seen in figure 3.3. Figure 3.3 (b) also shows the FIB cross section of the device coated with thin film of In doped SnO_2.

In the literature it has been shown that smaller electrode spacing can results higher NO_2 sensitivity for tungsten oxide (WO_3) thin film sensor[105]. According to this model, the original resistance of a semiconductor thin film sensor in air decreases with decreasing finger spacing. This is due to the reduction in the number of nanoparticles accommodate between the two electrodes and consequently reduce grain boundary barrier for charge transportation. The dependence of the H_2 sensitivity on the resistance of the thin film sensor in air, has also been experimentally demonstrated by others.[106].

3.3.1. Effect of Number of Fingers

In the case of interdigitated electrodes, an increase in number of fingers results in higher sensor performance for SAW devices based sensors. To understand the effect of the number of fingers on the electrical resistance based sensor, sensors with 8 and 20 fingers (and spacing 10μm between the electrodes) were fabricated and coated with In doped SnO_2 (150nm) film. Figure 3.4 shows the response transient of the sensors. It is observed that sensor does not show any variation in the response time. But surprisingly sensor sensitivity was higher for sensor with reduced number of fingers (n=8) as compared to the increased number of fingers (n =20). This can be pertained to scattering centers (such as grain boundaries and increased number of defects) for electron hoping. This result further directed author towards the miniaturizing of the device and so in all future work sensor device with 8 numbers of fingers were patterned.

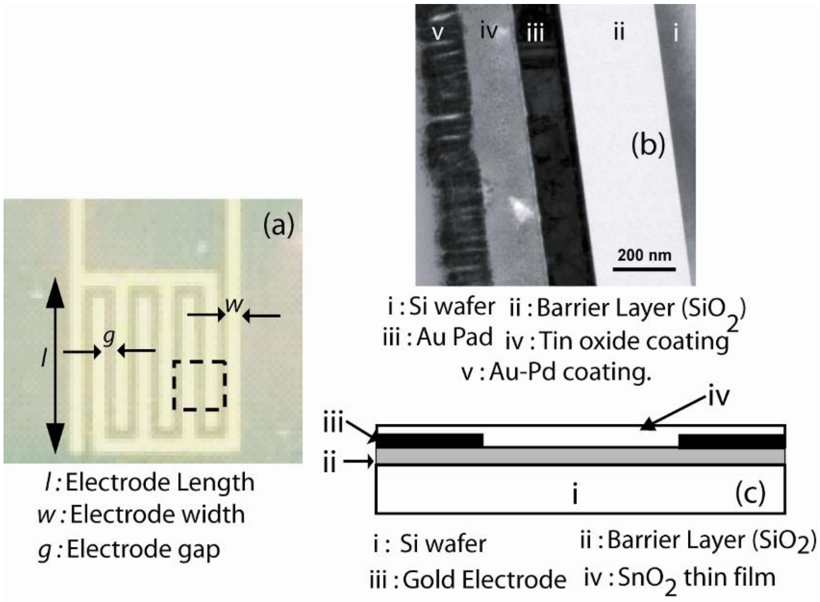

Figure 3.3 (a) Image showing the nano tin oxide coated micro chip; (b) Focused Ion Beam (FIB) cross section of the nano-tin oxide coated micro chip; (c) side of the metal oxide coating and electrode arrangement

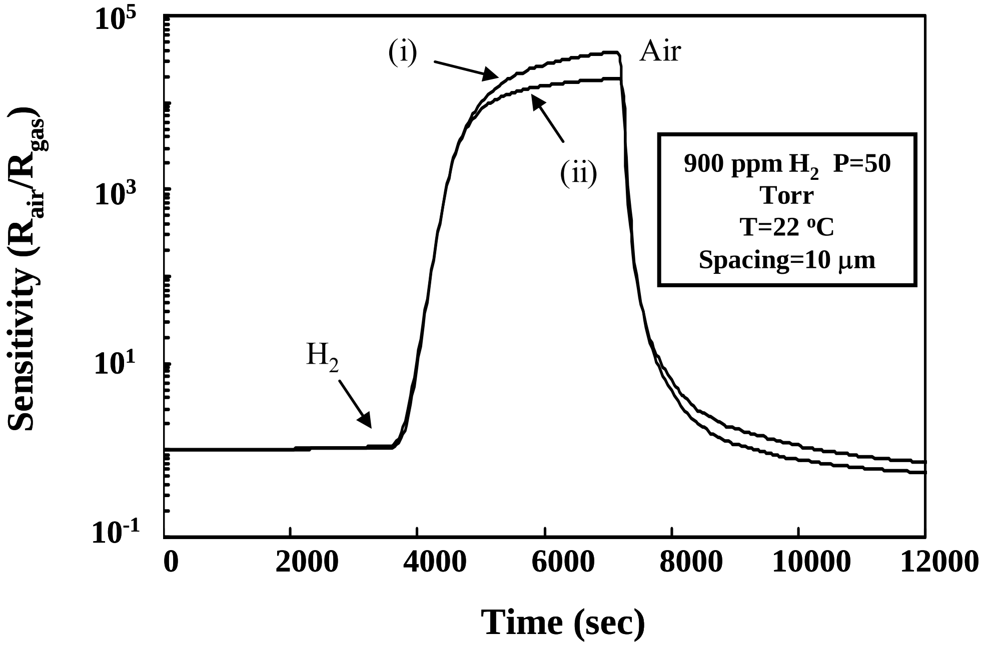

Figure 3.4.(a-b) Comparison of the variation in the room temperature H_2 sensitivity as a function of test duration for the nano-micro integrated sensor with two different numbers of fingers: (i)-8 and (ii)-20. (*reproduced by permission from S.Seal et.al.*[30]).

3.3.2. Effect of Electrode Spacing on Gas Sensing Behavior:

For understanding the effect of the finger spacing variation on sensor response, a Micro-electro mechanical (MEMS) hydrogen sensor device with varying electrode spacing (*g* =2-20 μm) and constant electrode length (*l*= 1000 μm) were fabricated[30] (figure 3.1). The gas sensing performance of the devices were tested at 900 ppm H_2 concentration at room temperature under the dynamic test conditions. The variation in the room temperature sensor-resistance as a function of test-duration for the present nano-micro integrated sensors with eight numbers of fingers is presented in Fig. 3.5 (a - inset).

It can be observed from figure 3.5 (a&b) that the variation in spacing does affect the response kinetics and sensitivity of the sensor. By varying the finger spacing from 20 to 2 micron sensor response time was reduced to few seconds (as low as 10 sec.).

This behavior can be explained from device as well as materials point of view. From materials point of view, the sensor response kinetics of the sensor is a function of the surface-adsorbed oxygen-ion concentration; while from the device architecture point of view, a rate of change of electrical conductivity of the device is dependant on the average distance traveled by the charge carrier from its origin to the edge of the electrode and charge trapping.

3.3.2.1. Material Aspect

Gas sensor response kinetics for different spacing between the electrodes from materials point of view (effect of surface adsorbed species, vacancy concentration, of the thin film material) is explained by Seal et.al.[30] in detail (also shown below). They have shown[30] that change in the resistance of the gas sensor is a result of variation in the surface adsorbed oxygen ions.

The sensitivity of the resistance based gas sensor is given as

$$S = \frac{R_{air}}{R_{gas}} \quad \text{...} \textbf{(3.1)}$$

The surface adsorbed oxygen ion concentration is related to the grain boundary potential as[30]:

$$[O^{-}] = \sqrt{\frac{2\varepsilon_r \varepsilon_o V_o V_{gb}}{e}} \quad \text{...} \textbf{(3.2)}$$

Where, O^{-} surface adsorbed oxygen ion concentration, *e* the electronic charge, V_{gb} the grain boundary potential, $\varepsilon_r\varepsilon_o$ is the permittivity of the sensor, $[O^{-}]$ the surface-adsorbed oxygen-ion concentration, and V_o the oxygen-ion vacancy concentration.

The relationship between the original sensor-resistance and the grain boundary potential in air, which is given by the relationship[30, 107]

$$R_{gas} = R_b \exp(\frac{eV_{gb}}{kT}) \quad \text{...} \textbf{(3.3)}$$

where, R_{gas} is the sensor-resistance in a reducing gas, R_b the bulk sensor-resistance, *e* the electronic charge, V_{gb} the grain boundary potential, *k* the Boltzmann's constant, and *T* the absolute temperature.

. Substituting the equation 3.2 in equation 3.3 we get [30],

$$R_{gas} = R_b \exp\left(\frac{e^2\left[O^-\right]_{surf}^2}{2\varepsilon_r\varepsilon_o kTV_o}\right) \quad \textbf{(3.4)}$$

The variation in the surface-adsorbed oxygen-ion concentration as a function of time in the presence of H_2 is determined here using the appropriate values $R_b= 20\Omega$, $e=1.6021\times10^{-19}$ *C*, $k= 1.3806 \times 10^{-23}\ m^2\ kg/\ s^2.K$, $T= 298K$, $\varepsilon_r\ \varepsilon_o = 8.8541\times 10^{-12}m^{-3}kg^{-1}s^4A^2$, and $V_o =1.6 \times 10^{23}\ m^{-3}$ for the sensor-tests conducted with two different electrode spacing, Fig. 3.6.

Again differentiating equation 3.4 w.r.t. to time (t)

$$\frac{dR_{gas}}{dt} \propto R_{gas}\left[O^-\right]_{surf}\frac{d\left[O^-\right]_{surf}}{dt} \quad \textbf{(3.5)}$$

As we have seen that from equation 3.1 the correlation between the sensitivity and resistance of the sensor equation 3.5 can be further modified as[30]

$$.\frac{d(\ln S)}{dt} \propto \left\{-\left[O^-\right]_{surf}\frac{d\left[O^-\right]_{surf}}{dt}\right\} \quad \textbf{(3.6)}$$

Thus, the response kinetics of the present nano-micro integrated sensor as represented by Eqs. 3.5 and 3.6 is a function of the product of the surface-adsorbed oxygen-ion concentration and the corresponding rate of change in the surface-adsorbed oxygen-ion concentration. It also appears from Eqs. 3.5 and 3.6 that, if the surface–adsorbed oxygen-ion concentration is a constant, then improved room temperature response kinetics would be observed if the rate of decrease in the surface-adsorbed oxygen-ion concentration in the presence of H_2 is higher. This condition has been essentially satisfied for the smaller electrode spacing.

3.3.2.2. Device Aspect

The sensor response kinetics is largely govern by the surface adsorbed species.(type of adsorbed species O^- or O_2^- and concentration of adsorbed species) The reaction between the analyte gas (H_2 in present case) and surface adsorbed species result in generation of free carrier (electrons). Generation of free carriers and the free carrier (charge) transportation inside the film governs the sensor response. The charge inside the film on the MEMs device can be trapped and scattered due to the various scattering centers such as grain boundaries, holes. Minimization of such losses can be largely reduced by reducing average distance traveled by the electron. So, it has been proposed that reducing the spacing can result in the amount of distance traveled by the electron with minimum scattering.

When, the thin film of indium doped tin oxide coated on the co-planar electrodes (see Figure 3.3 (c)) exposed to hydrogen gas, It results in simultaneous adsorption and diffusion to the reactive sites. The diffusion of hydrogen inside the film can be considered as one dimensional gas diffusion in a medium bounded by two parallel planes (figure 3.3(c) thickness (x_0)). The rate of reaction inside the film is effectively controlled by the diffusion rate of hydrogen. The ratio of the gas concentration inside the film at any point to the concentration of gas on the film surface can be defined as [108]:

$$C = \frac{c}{c_s} \text{ ....} \textbf{(3.7)}$$

If *c* is the concentration at a distance *x* inside the film and the gas of initial surface concentration (c_s) diffuses into the thin film of tin oxide (having thickness- x_0); lying on the co-planar electrodes, with boundary conditions:

$C = c / c_s = 1$ when $x = x_0$ (on surface of the film)………………………….**(3.8)**

and $C = c / c_s = 0$ when $x = 0$ (underneath the film)**……….(3.9)**

The solution satisfying above conditions becomes[108]:

$$C = \frac{c}{c_s} = 1 - \frac{4}{\pi} \sum_{n=0} \frac{(\ 1)^n}{2n+1} \cdot e^{\ D(2n+1)^2 \pi^2 t / 4x^2} \cdot \cos \frac{(2n+1)\pi . x}{2x_0} \text{ ……………} \textbf{(3.10)}$$

Where, D is diffusion coefficient of the diffusing gas, and *t* is time,

Introducing the dimensionless parameters,_in equation (3.10) as follows[108]:

$$T = \frac{D.t}{l^2} \text{ and } X = \frac{x}{x_0} \text{ ………………………………………………………….} \textbf{(3.11)}$$

Equation (3.11) becomes:

$$C = \frac{c}{c_s} = 1 - \frac{4}{\pi} \sum_{n=0}^{\infty} \frac{(-1)^n}{2n+1} \cdot e^{-(2n+1)^2 \pi^2 . T / 4} \cdot \cos \frac{(2n+1)\pi . X}{2} \text{ …………………..} \textbf{(3.12)}$$

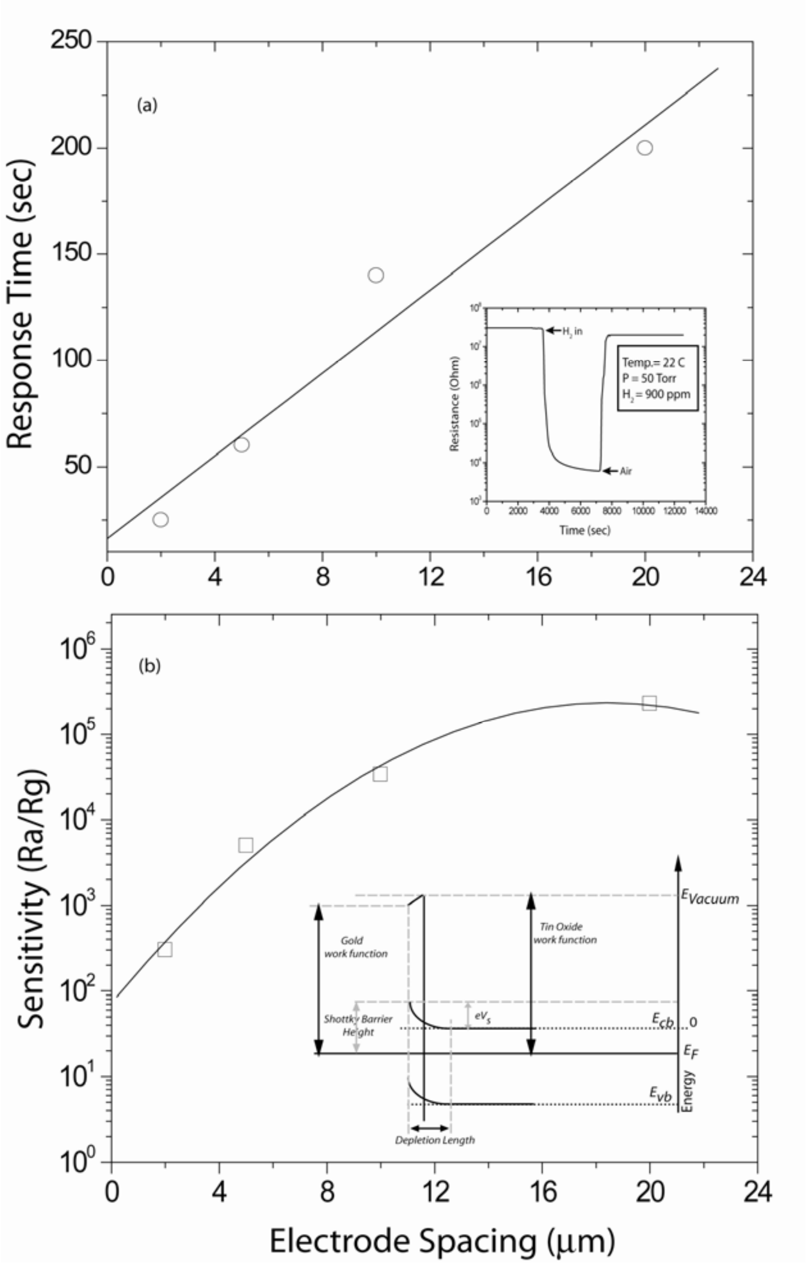

Figure 3.5 (a) Figure showing the effect of electrode spacing variation on the response time of the nano tin oxide coated MEMs devices towards 900 ppm of hydrogen at room conditions; (a-i) inset showing typical response transient nano tin oxide coated MEMs sensor; (a-ii) inset showing the effect of electrode spacing on rate of change of resistance inside the nano tin oxide coated thin film hydrogen sensor. (b) Impact of electrode spacing on gas sensitivity of the room temperature nano tin oxide hydrogen sensor.

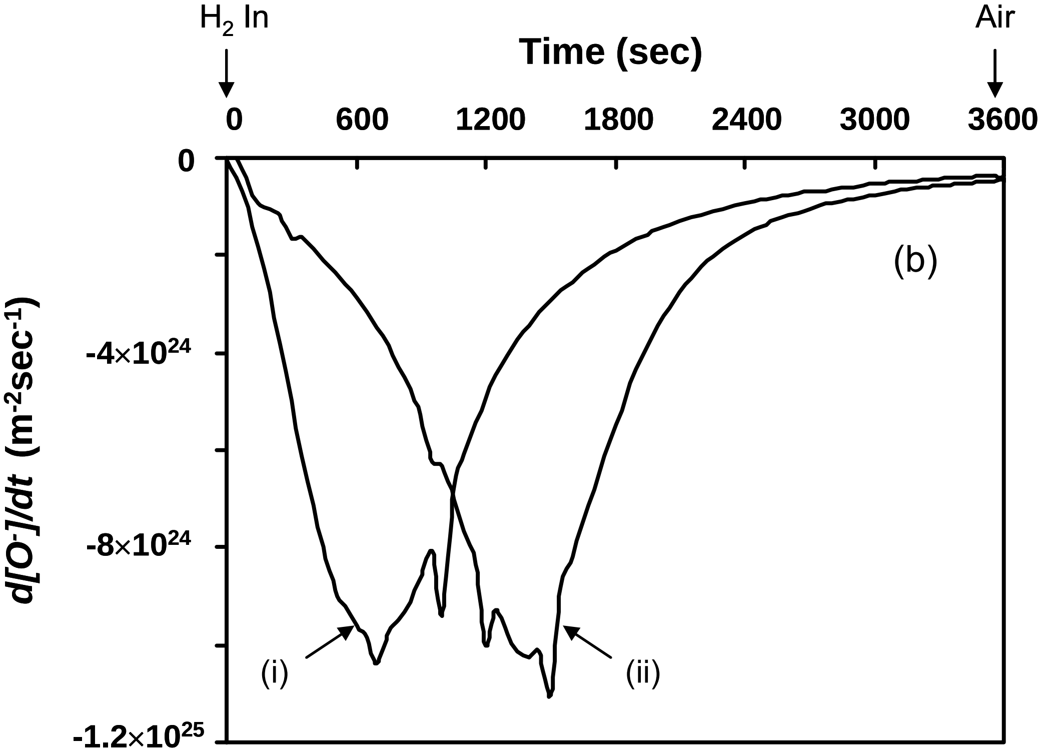

Figure 3.6 Figure showing rate of change of oxygen ion concentration of the In doped SnO coated MEMS device having electrode gap of (i) 10 micron (ii) 20 micron, respectively. (Figure reproduced by permission S.Seal. et. al.[30])

Analytical solution for the equation (3.12) is shown in figure 3.7 (a), which depicts the variation in concentration at different exposure time and varying film thickness. In the present case, the length of electrodes was kept constant (1000μm) for all sensor and the edge effect was neglected (since coating width>>coating thickness). According to Ohm's law the current is proportional to the applied electric field (E). The current density (current per unit area) "*J*" inside the nano tin oxide film is a function of the conductivity (*σ)*, and can be defined as[109]:

$$J = \sigma \cdot E \quad \textbf{(3.13)}$$

While the current flowing through the device is given by[110]:

$$i(t) = \int J.ds = \int \sigma.E.ds \quad \textbf{(3.14)}$$

The change in total current [*i(t)*] flowing through the device can be given by:

$$\Delta i(t) = \mu.e.k \int_{cs} c.E.ds \quad \textbf{(3.15)}$$

Where, c is the gas concentration, E is the electric field inside the film while μ and e are electron mobility and charge respectively.

The change in electric conductance is given by[110]:

$$\Delta G(t) = \Delta i(t) / V \quad \textbf{(3.16)}$$

Where, V is the applied voltage.

The solution for Laplace's equation for the semiconducting layer above the co-planar electrode is derived in detail elsewhere as[110]:

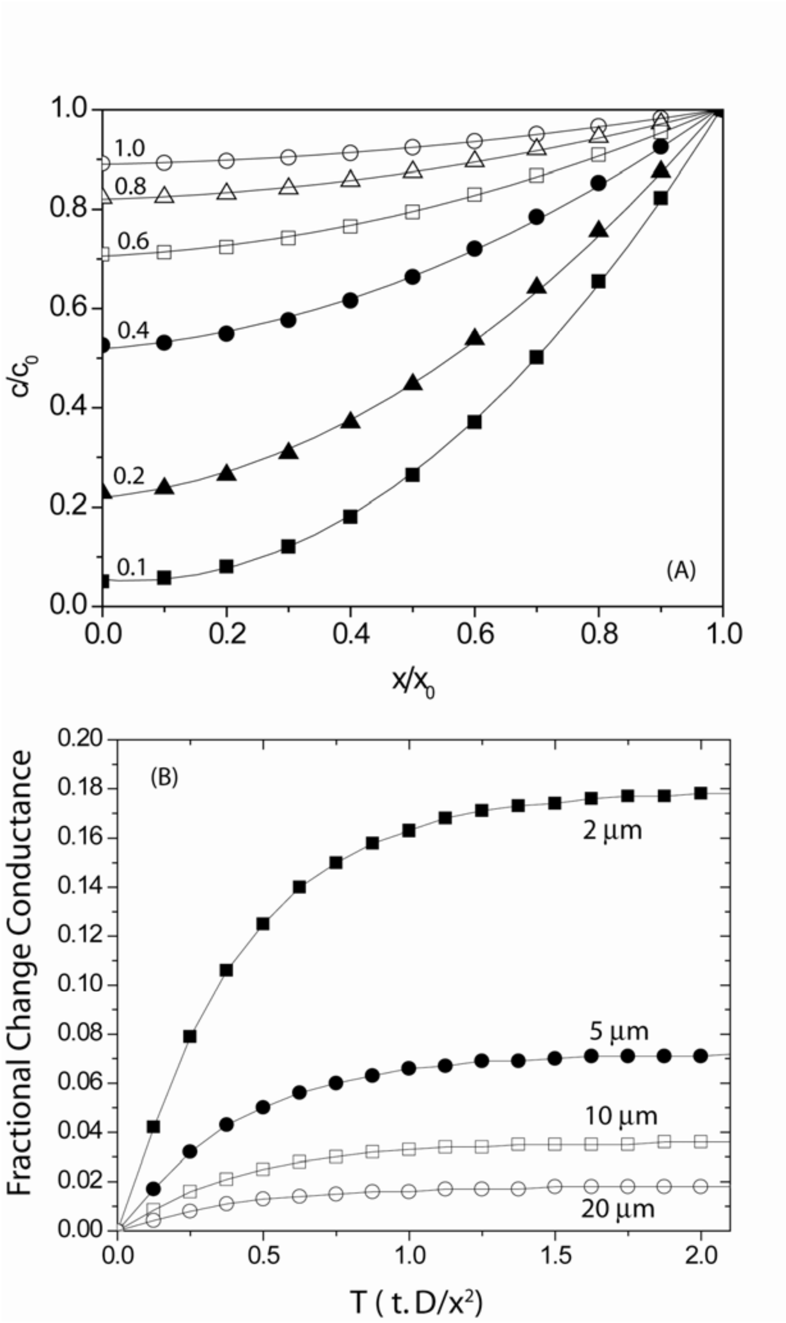

Figure 3.7(a) Figure showing variation in concentration at different exposure time (varied from 0.1 to 1.0) and varying film thickness (x/xo). (b) Change in fractional rate of conductance for different electrode spacing sensors.

$$\Delta G/G_0 = \int_0^1 C[(1-X)^2 + g^2/4x_0^2]^{-1/2}dx \ldots\ldots\ldots\ldots\ldots\ldots\ldots\ldots\ldots\ldots \textbf{(3.17)}$$

Where, G_0 is the initial conductance of the film.

The theoretical transient response for the current electrode geometry where the fractional change in conductance, plotted as function of factor "T" is shown in figure 3.6 (b) for different electrode spacings. From the figure it can be interpreted that the response of the device depends on the ratio g/x_0. At a constant thickness (x_0) the sensor response is solely controlled by the electrode spacings. Smaller gap size leads to faster change in the electric field inside the film resulting in faster response of the device.

Figure 3.5 shows the effect of electrode spacing (g) on the response time of the MEMs hydrogen sensors. From the figure it can be concluded that the sensor response time increases linearly with the electrode spacing. Inset in figure 3.5 shows a response transient of a sensor (electrode spacing = 5 μm and number of fingers = 8) when exposed to hydrogen (900ppm) at room temperature. Sensor with 5 micron electrode spacing showed a faster rate of change of resistance (higher conductance change) as compared to 10 and 20 micron electrode spaced MEMS sensors as shown in Figure 3.5. These experimental results are in good agreement with the theoretically modeled behavior of the effective variation in the electrode spacing on the sensor response. Change in spacing between the electrodes also changes the sensitivity of the sensor. Figure 3.5(b) shows the sensitivity of a nano doped tin oxide MEMS based hydrogen sensor. Increase in spacing from 2 μm to 20 μm results in an increase in active sensing area by almost 10% for a pair of electrodes. This results in the increase of sensitivity (S=Ra/Rg) from 500 (for 2 μm spacing) to 80000 (for 20μm spacing) for 900ppm H_2. When the sensor is exposed to hydrogen, gas molecules are adsorbed not only on the surface of the SnO_2 but also on the interface of the tin oxide-electrode (Au) interface. This results in an increase in the thickness of the electron-depleted layer of SnO_2 grain as well as in the work function of Au. As a result a large increase in the Schottky barrier height at the Au–SnO_2 interface is expected (inset of figure 3.5(b)). Due to a very high increase in the active sensing area, as the electrode gap increases the number of charge carrier (free electrons) after reacting with hydrogen, which results in the compensation of Schottky barrier height. Therefore, an increase in electrode spacing shows higher gas sensitivity.

3.3.3. Effect of Change in Length of the Fingers

For optimizing the parameter of the length, variation in length of the interdigitated electrode is also varied from 200 micron to 1000 micron. The base line conductance of the gas sensor is given by[111]:

$$G = \frac{\sigma b}{\pi} \cdot \ln\left[\frac{1+(1+w^2/L^2)^{1/2}}{w/2L}\right] \qquad \textbf{(3.18)}$$

Where, G is the base line conductance, b is length of the electrodes and w and L are the spacing and film thickness respectively. Earlier, J.W.Gardner[111] has mentioned that for very thin films coated on inter-planar electrode above equation can further get simplified as:

$$G \approx \frac{2\sigma bL}{\pi . w} \qquad \textbf{(3.19)}$$

But, this shows that higher the electrode length lower the sensor resistance. Similar trend was observed in present investigations (seen in figure 3.8) as 200 micron finger length sensor showed order of magnitude higher resistance as compared to 1000 micron electrode length sensor. It has been also observed that the length of the electrode increases sensitivity of the electrode also increases. From figure 3.8 it can be observed that when length of the sensor decreased from 1000 micron to 200 micron sensor response kinetics did not affect the response time but sensitivity of the sensor did change orders of magnitude. This can be pertained to the higher surface area available for the gas sensing and consequently higher O^- concentration which consequently results in increase in gas sensor sensitivity.

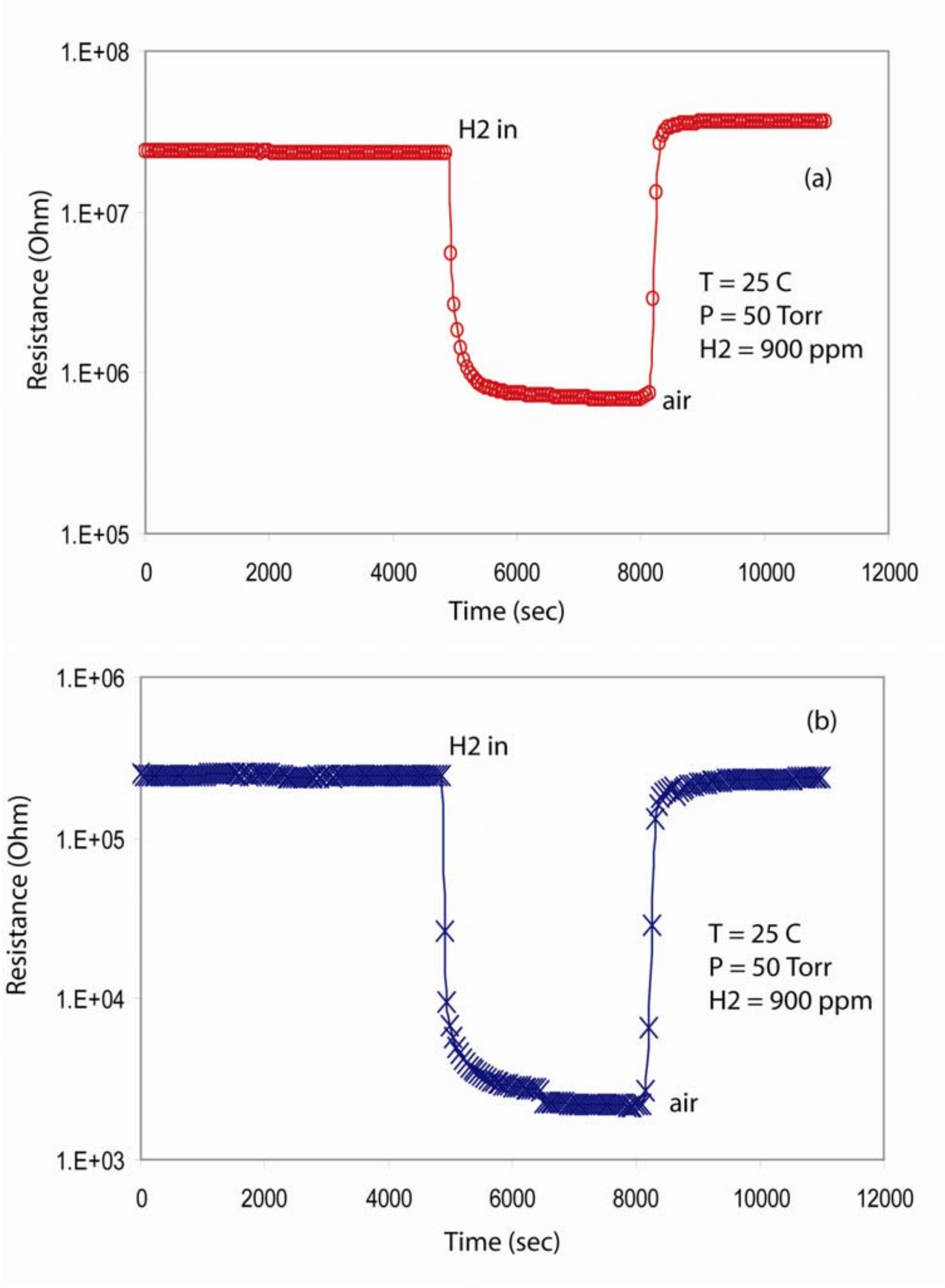

Figure 3.8 Figure showing transient response of the room temperature H_2 sensor as a function of test duration for the nano-micro integrated sensor with two different numbers of finger length: (a) 250 μm and (b) 1000 μm.

3.3.4. Integration Issues in Gas Sensor Arena

In application of nanostructured materials for gas sensing application the integration step of nanostructures with MEMS device is the toughest challenge. And this issue becomes pronounced when morphology of the nanostructures reduced to 1 D. The instability of the nanostructured based sensors can be divided into three major issues: i) contact between the electrode (actuators) with metal oxides, ii) in process contamination and iii) impurities in or on the barrier layer. Out of these three contact issues are more pronounced but other two can not be neglected either. Thin film deposition technique are easy but can not be applicable for the all type of nanostructures

Contact issues are related to the deposition (integration methods) used. In single or multiple nanowires (nanotube or nanobelts) configuration based sensors, nanostructures can be directly grown on the MEMS device or can be transferred on the suitable substrate after the synthesis process. On substrate direct development technique is more feasible as shown by the Grimes et. al[112]. It is easy to fabricate highly porous nanostructures of TiO_2 using anodization of the Ti metal in HF environment and development of contact pads after synthesis. They have shown very high sensitivity towards hydrogen. In this study, synthesis and development of TiO_2 using anodization was carried out. But, the sensitivity shown was by this sensor was poor (S=4) as compared to the reported values in the literature ($S \sim 10^5$)[101]. Formation of the barrier layer, deposition of surface catalyst and post heat treatment to achieve specific phase (anatase) further intricate the development process. This is of course not an easy task when dealing with metal oxide structures due to their resistance to corrosive environments. Especially, application of such methods on large scale further highlights the nanostructure integration issues.

In another approach, synthesis of 1-D nanostructures was carried out separately. and the nanostructures are integrated into MEMS device using drop casting method. In the sense, 1-D nanostructures can be dispersed into the solvent and then drop cast on the area of interest. Ease of deposition is though key advantage of this method but poor repeatability, reliability is the major concern of this technique. Also, to improve the mechanical stability and electrical contacts, thin metallization can be deposited by focused ion beam (FIB) or electron beam deposition (EBD) between the nano-wires and the pre-existing pads. In single nano-wire configurations a nano-manipulator can be used for transferring nano-wire in the desired position on the transducers. During these processes adsorption of the superfluous species such as water or other molecules can largely impact the overall gas sensing behavior of the nanosensors. But nanostructure manipulation approach can not be implemented in a large-scale production scenario. Contact issues remain still one of the biggest problems when dealing with 1D nanostructures.[79]

CHAPTER 4. HYDROGEN INTERACTION WITH DIFFERENT NANO-MO_X AT ROOM TEMPERATURE

4.1. Introduction

Interaction between the gas sensor and analyte gas (H_2) depends on the material, operating temperature, oxygen partial pressure and catalyst. The following section explains in detail the mechanism of hydrogen detection using nanostructured MO_x (SnO_2 and TiO_2) semiconductors at room temperature.

4.1.1. Hydrogen Detection Mechanism using n- type Metal Oxide Semiconductors:

Typically the gas sensing mechanism of various n-type nanocrystalline semiconducting materials are the same. Mainly the generation of point defect in the nanocrystalline structure of these materials determines the variation in the conductivity of materials. Until recently the gas sensing devices were made up of in built heater for faster analyte gas dissociation and subsequent reactions[62]. But, as we are driving towards gas sensing at room temperature, the oxygen ion vacancies, impurities and presence of surface catalyst govern the gas sensing characteristics of the n- type nanocrystalline gas sensors.

When a freshly prepared nanocrystalline MO_x semiconductor is exposed to air, physisorbed O_2 molecules pick-up electrons from the conduction band.[43] The adsorbed O_2 molecules change their states to $O_2^-{}_{ads}$ or O^-_{ads} species. Below 150-200 ^oC, the adsorption of $O_2^-{}_{ads}$ dominates; and above this range, $O^-{}_{ads}$ is the dominantly adsorbed species[43].

$$O_0^x \,\square^{\cdot\cdot}\, \frac{1}{2}O_{2(g)} + V_O^{00} + 2e^- \ldots\ldots\ldots\ldots\ldots\ldots\ldots\ldots \mathbf{(4.1)}$$

Consequently, the space-charge-layer (an electric-double-layer) is formed near the surface of the particles, which creates a potential-barrier for electron conduction in between the particles increasing the electrical resistance of the gas sensor.

However, when a reducing gas (such as H_2) comes in contact with this material, it gets oxidized via reaction with the $O_2^-{}_{ads}$ or $O^-{}_{ads}$ species, and subsequently, electrons are reintroduced into the electron-depletion-layer, leading to decrease in the potential-barrier[43].

$$H_2 + \frac{1}{2}O_2^-{}_{(ads)} \rightarrow H_2O_{(ads)} + e^- \ldots\ldots\ldots\ldots\ldots\ldots\ldots\ldots \mathbf{(4.2)}$$

$$H_2 + O^-{}_{(ads)} \rightarrow H_2O_{(ads)} + e^- \ldots\ldots\ldots\ldots\ldots\ldots\ldots\ldots \mathbf{(4.3)}$$

The sensor-resistance, thus, reduces in the presence of reducing gas. The sensitivity of the SnO_2 thin film is usually defined as[31]:

$$S = \frac{R_{air}}{R_{gas}} = \frac{G_{gas}}{G_{air}} \ldots\ldots\ldots\ldots\ldots\ldots\ldots\ldots \mathbf{(4.4)}$$

where, R_{air} and R_{gas} are the resistances, and G_{air} and G_{gas} are the conductances, of the sensor in air and reducing gas respectively.

It is to be noted that, along with the sensitivity, there are three other important sensor-parameters-(i) response time, (ii) recovery time and (iii) H_2 selectivity, which also need to be considered for optimizing the sensor-performance. The response time is defined as the time required for dropping the sensor-resistance by 90% of the total drop (R_{air}-R_{gas}); while, the recovery time is defined as the time required for recovering 90% of the total drop (R_{air}-R_{gas}) after removing the H_2 and purging air into the test-chamber. On the other hand, the H_2 selectivity is defined as the ability of the sensor to sense only H_2 from the gaseous mixture having other reducing gases such as carbon monoxide (CO), nitrogen oxide (NO_x), hydrogen sulfide (H_2S), methane (CH_4), and ethanol (C_2H_5OH).

Continuous efforts are underway to reduce the response, recovery times and maximize the H_2 sensitivity and selectivity of nanocrystalline gas sensor. Following sections discusses the interaction of hydrogen with different morphologies of SnO_2 and TiO_2.

4.1.1.1. Hydrogen Detection using Porous SnO_2 Thin Films

All the gas-sensing trials were conducted under dynamic test conditions at room temperature as described earlier.[113] A mixture of appropriate amounts of nitrogen and hydrogen was introduced into the test-chamber through the respective mass-flow-controllers.

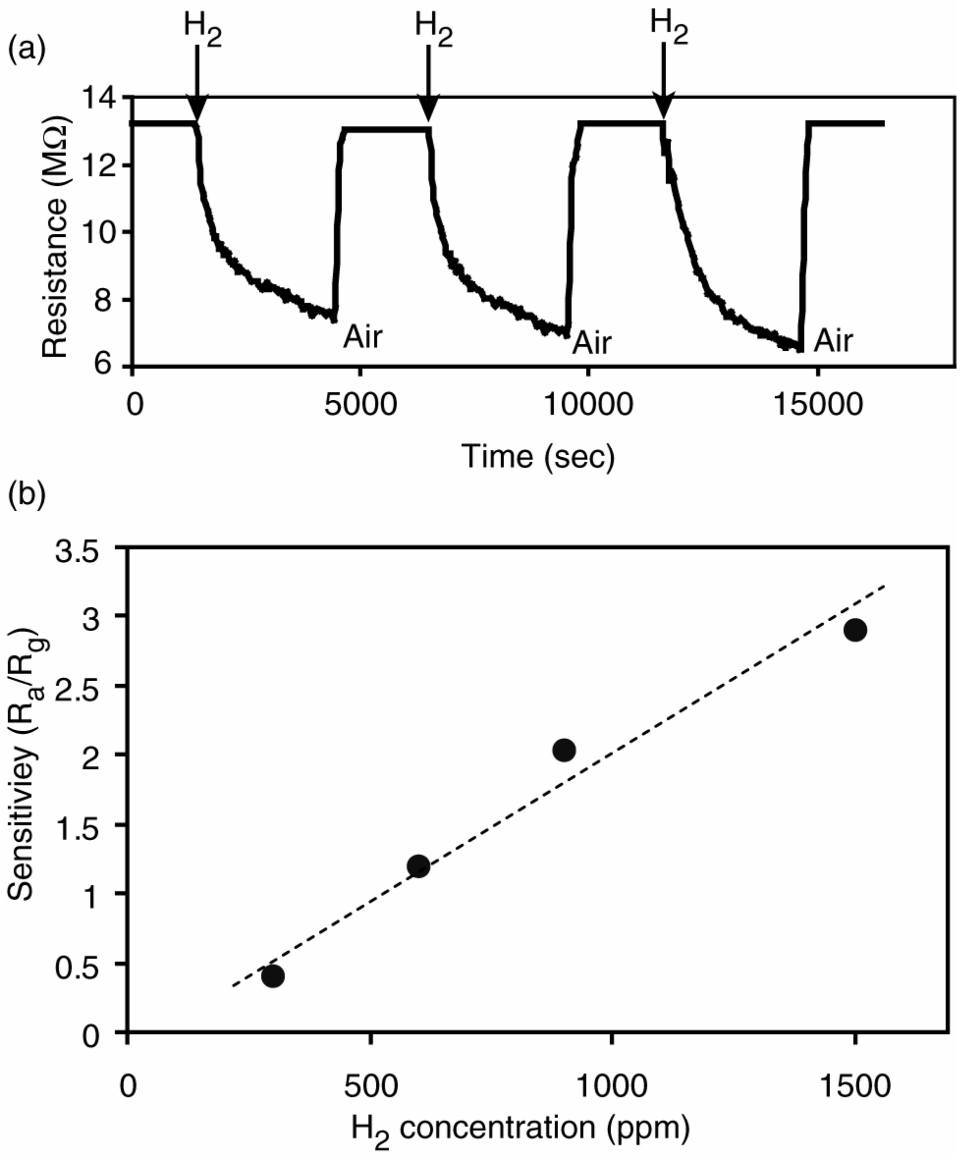

Figure 4.1 (a) Response transients of ordered tin oxide thin film sensor at room temperature to 900 ppm hydrogen gas (b) Effect of hydrogen concentration on the sensitivity of templated nanoporous tin oxide film at room conditions.

The response transient at room temperature of a nano-micro integrated sensor for H_2 (900 ppm) under cyclic testing conditions is illustrated in Fig. 4.1(a). Three cycles were conducted over a period of approximately 4 hours, and good reproducibility was obtained across all cycles.

Thus, the sensor resistance is reduced in the presence of hydrogen. Fig. 4.1(b) represents the effect of hydrogen concentration (300-1500 ppm) on the sensitivity at room temperature. The sensitivity increased from 1.3 to 3 when hydrogen concentration was increased from 300 ppm to 1500 ppm. Table 4.1 shows typical sensitivity values of pure tin oxide thin film sensors. Except for the present study, all the sensors have been tested at elevated temperatures (more than 200 ^{o}C). Lower sensitivity observed in present testing is correlated possibility due to the surfactant residue on the film surface or improper catalyst (Pt) distribution (resulting poor spillover effect).

The integration of nanoporous tin oxide thin films with a MEMS device and detection of hydrogen (as low as 300 ppm) is thus successfully demonstrated. Ordered nanoporous tin oxide thin films prepared using the surfactant-templating are promising candidates for gas sensing applications.

4.1.1.2. Hydrogen Detection using Thermally Grown SnO_2

Figure 4.2 (a) shows the cartoon diagram of the tin oxide nanowires based sensor device. Figure 4.2(b-inset) shows the response kinetics of the pristine tin oxide nanowires show very less sensitivity (even negligible) towards hydrogen. Sensor showed very sluggish response kinetics.

Table 4.1 Comparison of various different undoped SnO_2 gas sensor performance

SynthesisTechnique	Operating Temp	Test Gas Conc	Sensitivity	References
Sol-Gel	250	2000	1.18	J. Gong et.al.[62]
MOCVD	300	10000	2.5	Lee et.al[114].
R-IAD	250	1000	95	S.-K.Song et.al.[115]
R.F.Sputtering	350	1000	2	R. Sanjinis et.al[116].
Sintered	300	1000	7.6	V.A. Chaudhary et.al[117].
Sol-Gel	250	640	17.4	J.W,Hammond et.al.[118]
Template-assisted	22	1500	3	Present Study

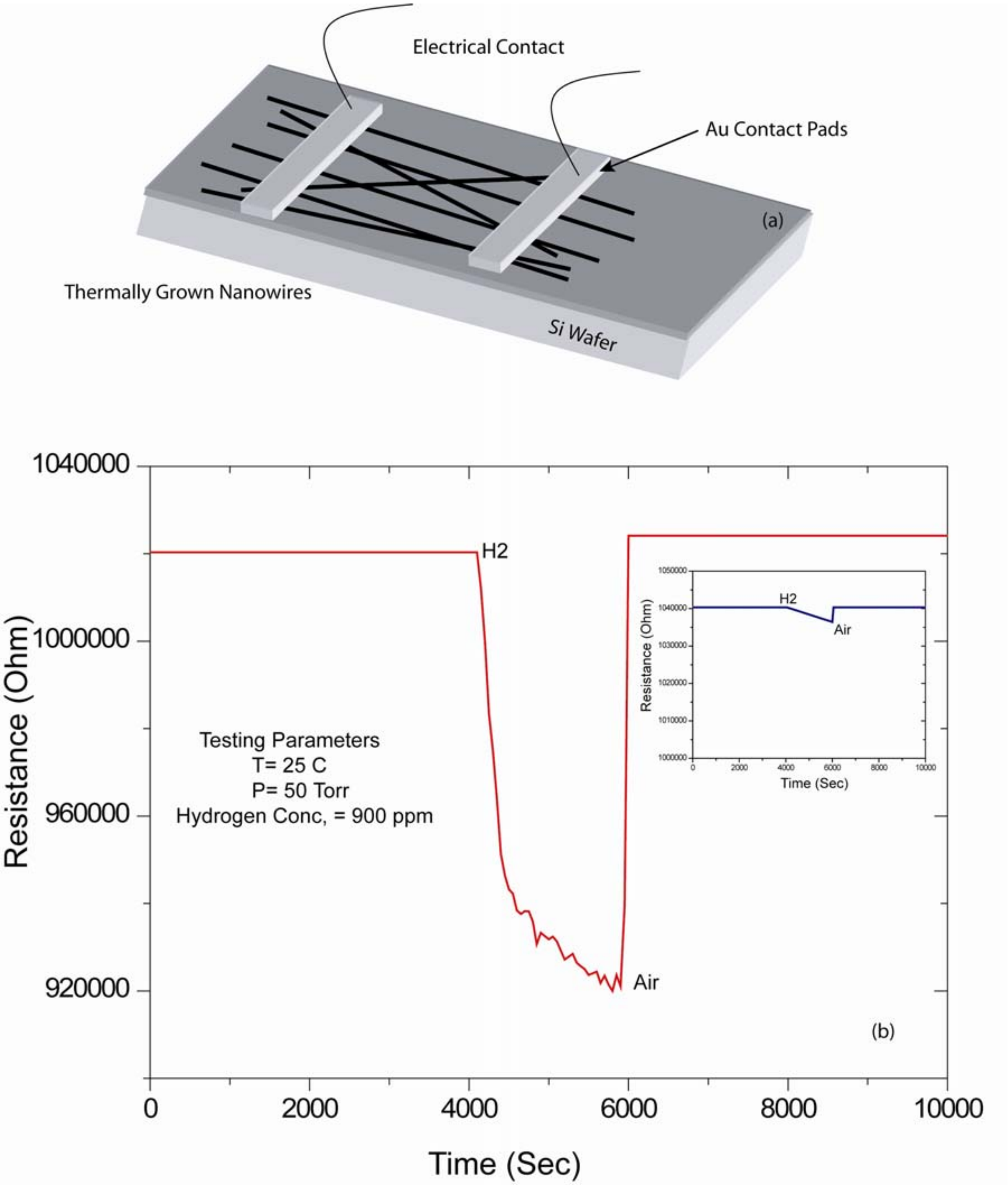

Figure 4.2 (a).Figure showing the schematic of contact geometry for multiple-nanorod gas sensor (b) Response transient of the thermally grown nanowire sensor device to 900 ppm hydrogen at room conditions. Inset showing gas sensor performance of SnO_2 nanowire based gas sensor at room temperature with out having any catalyst (pt) on the sensor surface.

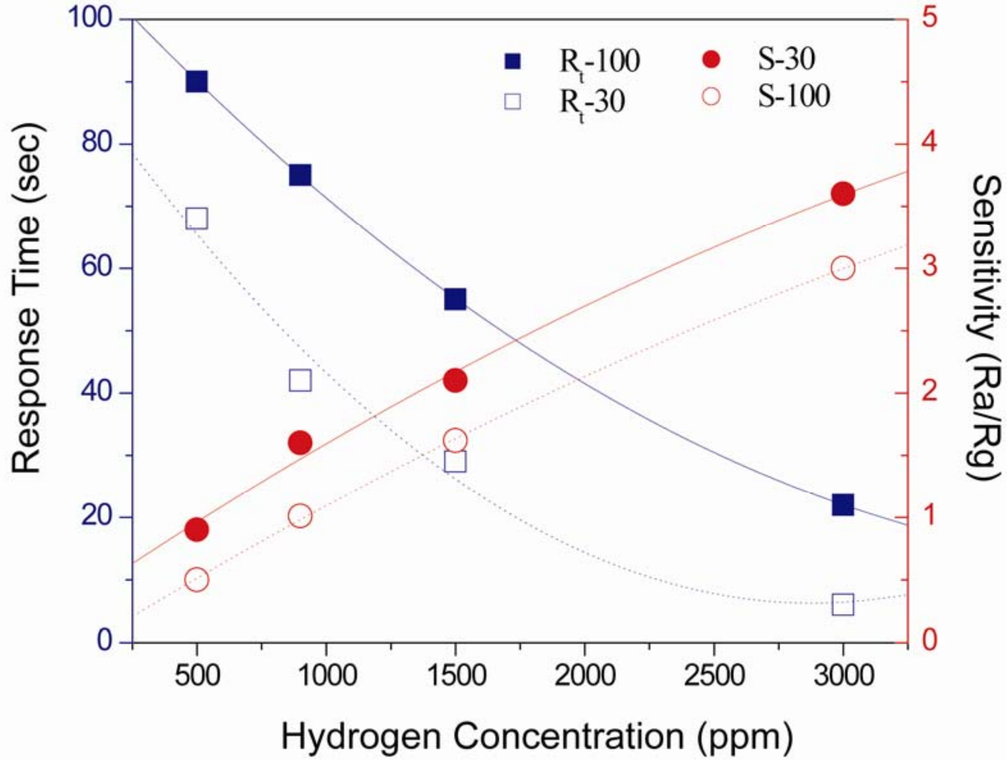

Figure 4.3 Sensitivity and Response time of the thermally grown nanowires having different nanowire diameter.

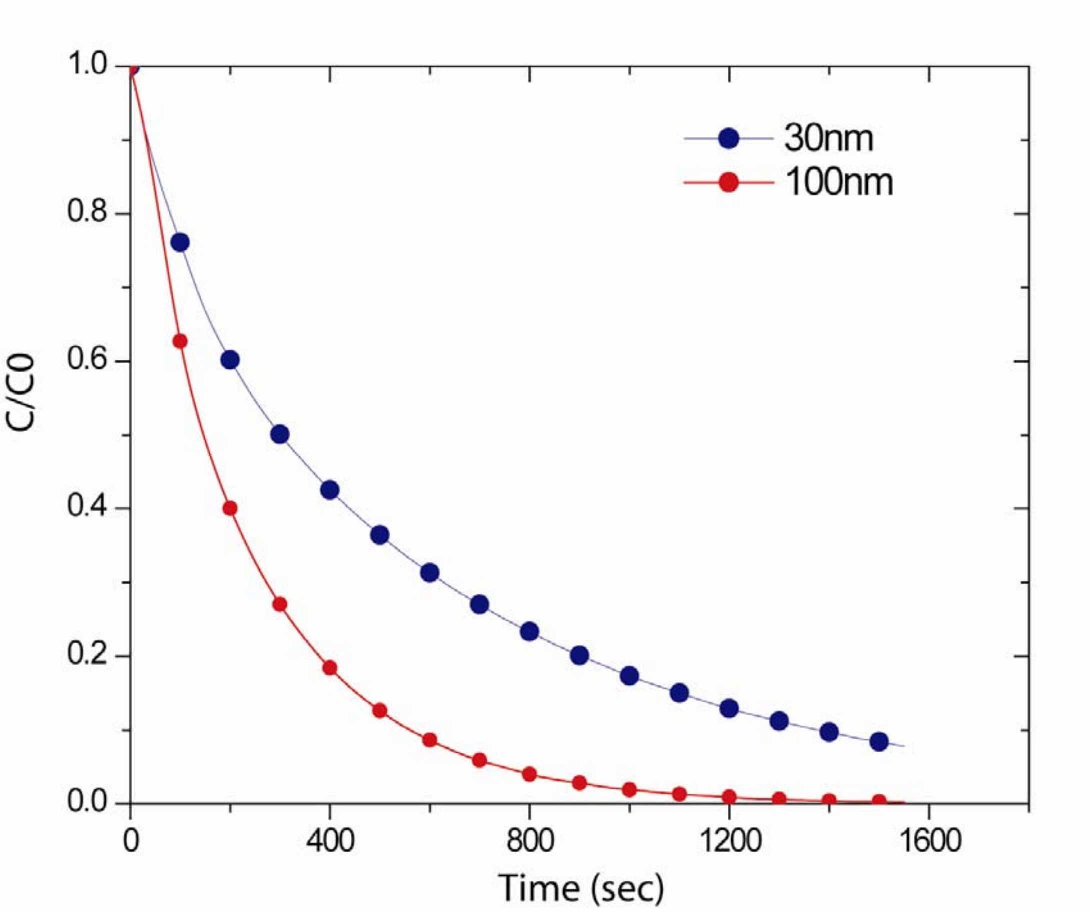

Figure 4.4 Effect of concentration variation on nanotube with respect to time. Faster diffusion of hydrogen inside the small diameter nanowires leads the faster response kinetics and enhanced sensor performance**.**

Sensor device was sputtered with Pt (~10nm) and heat treated at 400C for 1hr. Response kinetics of this sensor is shown in figure 4.2(b). Figure 4.3 represents the effect of hydrogen concentration (500-3000 ppm) on the response time and sensitivity at room temperature for TNWS of different diameters. Response time of almost 10 sec was shown by sensor device having tin oxide nanowires with 30nm. While, sensitivity increased from R_a/R_g = 1.4 to 4 when hydrogen concentration was increased from 500 ppm to 3000 ppm (shown in figure 4.3). The sensors were capable of detecting hydrogen in the range of ppm at room temperature using very low power requirements and recovers quickly once the hydrogen is removed (see figure 4.2b). Lower sensitivity observed in present testing is due to the operating temperature of the gas sensor. at lower operating temperatures (<100^{o}C), the SnO_2 surface preferentially adsorbs $O_2{}^{-}{}_{ads}$ ions than $O^{-}{}_{ads}$ ions. And $O^{-}{}_{ads}$ ion is more reactive with H_2 than $O_2{}^{-}{}_{ads}$ ions, which result in lowering the sensor sensitivity towards hydrogen. Also, the need of activation energy for molecular H_2 dissociation into atomic H increases with decreasing operating temperature. This increased activation energy impede the H_2 sensitivity with lowering the operating temperature. Presence of Pt on nanowire surfaces act as a catalyst for hydrogen dissociation. Previous studies have shown that hydrogen adsorption energy is lowest on pt surface than Ni and Pd[119,120]

Figure 4.4 shows the effect of diameter of nanowires on the overall hydrogen sensing performance. Figure shows dependence of the response kinetics of the sensor device on the hydrogen diffusion into the nanowire. Electro-neutrality is maintained by the charge transfer between the hydrogen molecule and specific active site and this leads to increase in charge carrier density. We can describe this process with a model of diffusion in the solid cylinder with constant gas surface concentration. For a nanowire having radius “r” , the concentration variation inside the nanowire can be given by:[108]

$$C(t)/C_0 = 1 - \sum_{n=1}^{\infty} \frac{4}{\alpha_n^2} 4 \cdot e^{-D \cdot \alpha_n^2 \cdot t / d^2} \qquad \ldots\ldots\ldots\ldots\ldots\ldots\ldots\ldots\ldots\ldots\ldots\ldots\ldots\ldots\ldots\ldots \mathbf{(4.5)}$$

Where, C_0 is the initial surface concentration, D (4.3 x 10^{-11} cm^2/s) is the apparent diffusion coefficient. α_n is the roots of $J\alpha = 0$, where J is the Bessel function of the first kind (values are taken from Bessel function table from book “Diffusion in solids” by J Crank [108]). Considering the constant diffusion coefficient, figure 4.4 shows the faster concentration variation inside the nanowire with 30nm diameter to sensor with a diameter of 100nm. This leads to better performance of sensor device having 30nm diameter as compared to the sensor device with 100 nm diameter.

In conclusion, tin oxide nanowires was successfully synthesized using oxide assisted growth mechanism. The size of the nanowires was found to be dependent on the function of substrate coverage of catalyst and governs the final diameter of the nanowires. These nanowires were successfully incorporated in the MEMS device. TNW sensor successfully detected hydrogen with response time as low as 10 sec at room temperature.

4.1.1.3. Hydrogen Detection using Thin Films of In Doped SnO_2

Successful detection of hydrogen at room temperature using In doped SnO_2 was first reported by our group in open literature. Also, Seal et.al.[30,46] have shown the champion sensitivity (Ra/Rg = 10^6). They have also explained detail inverse catalysis effect, UV light radiation, aging and He environment in hydrogen detection at room temperature.

Details about the In_2O_3-SnO_2 sensor are discussed in previous sections (section 3.1 to 3.4) in detail.

4.1.2. Morphological Impact on Gas Sensing Mechanism of Nanostructured Materials.

A significant amount of research has been developed and utilized in the area of nanoparticle gas sensing properties and mechanism. Before discussing the differences between the metal oxides based semi-conducting mechanism of nanoparticles and nanowires following facts must be established.

A very important aspect of semiconductor nanoparticle bas chemical gas sensing is the application of the nanoparticles as thin films. This is very important to maintain the continuity between the particles across which the conductance (or resistance) is measured. The individual nanoparticle make up will cause disruption or discontinuity of the electronic transition resulting in inaccuracies and inconsistency in data.

Another important factor in the mechanism of nano particle thin film based metal oxide semiconductor is the influence of surface oxygen vacancies and amount of chemisorbed oxygen on the surface of the metal oxide. It is known that for metal oxide nanoparticles the presence of oxygen vacancies on the surface (essentially surface defects) changes their behavior as n-type semiconductors. Specifically any stoichiometric oxide upon excitation with energy sources such as annealing in vacuum, under reducing inert atmosphere, exposure to UV rays etc may cause the desorption of surface oxygen to create oxygen vacancies. It is the presence of oxygen vacancies that dominate the electronic properties of the sample and correspondingly the conductance (or resistance) based gas sensing. The oxygen vacancies create a donor level just below the conduction band which is separated by a very low energy. While several parameters govern the sensing mechanism in whole much of the *room temperature sensing is governed by this energy gap*. A high vacancy concentration reduces this energy gap thereby causing the large fraction of electrons in the donor state to excite to the conduction band at room temperature. On the contrary if the energy band gap is high a large amount of energy is needed (usually thermal energy) to cause the excitation of electrons from the donor level to the CB of the metal oxide.

Exposure of a nanocrystalline metal oxide such as tin oxide to air leads to the chemisorption of oxygen molecules on the surface of the particles. This phenomenon is progressed by the trapping of the free electrons by the adsorbed oxygen species through a charge transfer from metal oxide to oxygen species. With the adsorption of oxygen the surface vacancies are repopulated forming the ionized surface oxygen. The coverage of oxygen adsorbed or the surface coverage, θ, is a function of multiple components such as partial pressure of oxygen, system temperature, adsorption and desorption rate constants and on the concentration of the electrons, n, involved in charge transfer and upon the concentration of free available sites, N_s, for chemisorption. The following equations hold good for sensing mechanism[73]

$$\frac{\beta}{2} O_2^{gas} + \alpha . \cdot e^- + N_S \leftrightarrow O_{\beta S}^{-\alpha} \quad \text{...(4.6)}$$

$$K_{ads}.N_S.n.p_{O_2}^{\beta/2} = K_{des}.\theta \quad \text{..(4.7)}$$

Where K_{ads} and K_{des} are the rate of surface oxygen adsorption and desorption. Now assuming these to be constant, the above equation will be affected by the surface coverage, θ, and the amount of unoccupied vacancy, N_s. Since the nanocrystalline materials have higher surface area and higher number of defects the influence and predominance of equation [37] in the sensing mechanism is increased by several orders of magnitude for a nanocrystalline material. This accounts for the large improvement in the sensitivity of nanocrystalline materials over bulk metal oxides. The Seal Group[31,45,46] showed that nano indium doped tin oxide have a carrier concentration of ~ 1.9 x 10^{17} cm^{-3} arising from oxygen vacancies (defects). Sensor developed using nano indium doped oxide have shown giant sensitivity (10^{6}) at room temperature. Anodized TiO2 nanotubes (~ 50nm diameter) have shown carrier concentration of ~1.9x 10^{19} cm^{-3} for sample annealed in inert atmosphere. Grimes et.al.[101,112] have developed sensor from titania nanitube based sensor having similar sensitivity.

The chemisorption of oxygen species on the surface also causes the shift in the Fermi level of the of the metal oxide semiconductor away from the conduction band thereby reducing the conductance of the metal oxide[73] This leads to a) band bending observed in nanocrystalline thin film semiconductors from interior to the surface of the metal oxide and b) formation of flat bands in nanocrystalline nanowires and nanotubes[73]. C.Drake[63] has reported band gap about 2.8eV for In doped SnO_2 particles as compared to bulk tin oxide (3.6eV). D. Calestani et.al.[121] have reported band bending of ~1eV in case tin oxide nanowires having diameter 150nm. Anodized TiO_2 nanotubes have shown reduced flat band potential (-0.5V) as compared to compact TiO_2 oxides (-0.85V)[122] This is one of the major differences in the electronic properties shown by 3-D and 1-D nanoparticles. The ionization of the adsorbed oxygen on the surface creates a 30-100nm thick electron deficient surface layer (corresponding to the Debye length). It has been well documented in literature that when the Debye length of nanoparticles becomes comparable to the radius of nanoparticles, a significant shift is observed in the Fermi level of metal oxides. In case of nanocrystalline thin films this causes a band bending as we move from the bottom of the thin film to the surface of the film[73]. In case of nanowires the charge depletion layer cause by trapping of electrons by the adsorbed oxygen encompasses the entire nanowire resulting in so called flat band conditions wherein the Fermi level shifts away not only on the surface but throughout the entire nanowire[73]. This causes a new kinetic equilibrium to be established among the free electrons and the unoccupied and occupied vacancies. During the flat band conditions and because of the radial geometry of the electron momentum, the participating electrons can reach the surface of the nanowire without any interference from the low electrostatic barrier. The electrons are distributed homogenously throughout the entire volume of the nanowire and leads to the increased response time of the nanowires. Thus the charge conservation condition simplifies to[123]

$$Ns.\theta = \frac{R}{2}.(n - n_m) \text{ ....} \textbf{(4.8)}$$

Where n_m is the density of participating electrons remaining in the nanowire after exposure to adsorbing gas. Mathematically, the electron depletion, $\Delta n = 2Ns\theta/R$, occurred due to gas –surface adsorbed species interaction, leads to a significant drop in conductance is given by[123]:

$$\Delta G = \frac{\pi \cdot R \cdot e \cdot \mu}{L} \cdot \frac{2N_s\theta}{R} \ldots\ldots\ldots\ldots\ldots\ldots\ldots\ldots\ldots\ldots\ldots\ldots\ldots\ldots\ldots\ldots\ldots\ldots \mathbf{(4.9)}$$

It must be noted that the electron diffusion length is greatly reduced in nanocrystalline materials and nanowires as compared to bulk counterparts which is essential for the electrons to participate in sensing mechanism before recombining and falling back to bulk/surface.

After exposure of sensor to the reducing gas environment (such as hydrogen), following reaction occurs on the surface[123]:

$$\beta \cdot H^{gas} + O^{-\alpha}_{\beta.S} \rightarrow \beta \cdot H_2^{gas} + \alpha \cdot e^{-} \ldots\ldots\ldots\ldots\ldots\ldots\ldots\ldots\ldots\ldots\ldots\ldots \mathbf{(4.10)}$$

This results the removal of surface adsorbed oxygen species and introduction of electron in the conduction band resulting the increasing the sensor conductance[123]. It has been shown that increase in charge career concentration (Δn) is directly related to partial pressure of analyte gas (here reducing gas).[123] Increase in gas sensor conductivity increases monotonically with gas partial pressure.

Thus ideally one dimensional nanostructures should exhibit increased sensing performance than the nanocrystalline particles in the form of thin films. However in a real world environment a large array of nanowires and/or nanotubes complicates the picture of sensing mechanism by increasing additional surface defects arising from the interfaces of adjoining nanowires. The surface hydroxides and hydrocarbons are also active on the nanowires as the adsorbed oxygen species thereby rendering loss of available surface sites for gas adsorption during sensing. The continuity of large array of nanowires that can collectively produce a synchronous measurable and detectable signal is lowered due to integration issues involved with 1-D nanostructures.

4.1.2.1. Hydrogen Detection using TiO2 Nanotube Synthesized using Hydrothermal Synthesis:

In earlier section, section 2.3.4 integration of the TiO_2 nanotube (hydrothermal) with MEMs device has been discussed in detail. Figure 4.5 shows the effect of hydrogen concentration on the gas sensing performance of the TiO_2 nanotube prepared by hydrothermal method. The maximum room temperature sensitivity (Ra/Rg) was 29 for 1500 ppm hydrogen. According to our knowledge this is the first report in open literature about detection of hydrogen at room temperature using hydrothermal TiO_2 nanotube. Jun et.al. [124] have shown that the high temperature (150 C) gas sensing of nanoparticle TiO_2 thin films is about $\sim 10^3$ for 1Vol % of H_2. Apart from that Grimes et.al[101]have successfully detected hydrogen using nanotube grown by anodization technique.

Whatever method has been used for synthesis, the basic gas sensing mechanism of nanotubes remains the same. Presence of *oxygen vacancies* dominates the electronic properties of the nano TiO_2 and consequently gas sensing properties. The oxygen vacancies create a donor level just below the conduction band which is separated by a very low energy. While several parameters govern the sensing mechanism in whole much of the *room temperature sensing is governed by this energy gap*. At high vacancy concentration as observed in case of TiO_2 nanotubes reduces this energy gap thereby causing the large fraction of electrons in the donor state to excite to the conduction band at room temperature. Titania nanotubes have large number of defects (oxygen vacancies) on their surface. Also, during the last step of hydrothermal processing of TiO_2 nanotube, high temperature of heat treatment of titanate in an inert atmosphere results the formation of oxygen vacancies.[98]

It has been investigated in numerous studies that the large number of defects arises from the nanoscale nature of the tubes as well as tubular geometry (high curvature) which leads to several broken and dangling bonds destroying the stoichiometry of the oxide. While the contact between two particles may create deep defects far from the Fermi level of the material,[112] in case of TiO_2 nanotubes these defects serve as additional sites where the adsorption as well as dissociation of hydrogen can take place making them *ideal for room temperature hydrogen sensor.*

Also, when exposed to reducing gas environment the consumption of the chemisorbed oxygen from the surface of the TiO_2 nanotubes, results in the charge transfer from chemisorbed oxygen to conduction band of the TiO_2. This phenomenon is predominantly influenced by the surface area and porosity in the material. It was reported[125] that for TiO_2 nanoparticles with an average diameter of 10nm, the surface area is ~110 m^2/g having average pore volume 0.1ml/g. In the present study, from BET analysis of hydrothermal nanotubes (figure 2.11) maximum surface area observed was ~ 400 m^2/g. This means that high surface area of nanotubes is available for gas adsorption as compared to titania nanoparticles. Most importantly the electron depletion region (SCL) exists on either side of the titania nanotubes (as shown in figure 4.7).

Also, in the present study Pt was used as catalyst on the surface of the nanotube. It catalyze the dissociation of hydrogen on the surface of the nanotube (spillover effect) resulting in the faster response and higher sensitivity of the current hydrothermally grown TiO_2 nanotube based hydrogen sensor at room temperature.

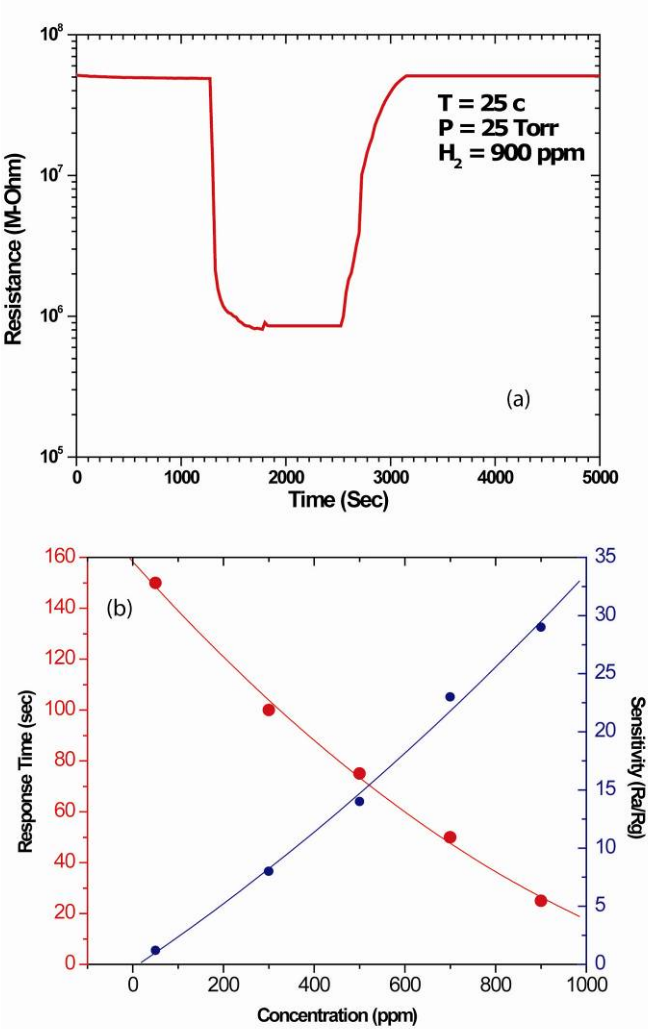

Figure 4.5 (a) Response transient of TiO_2 nanotube synthesized using hydrothermal route at room temperature in presence of 900 ppm H_2 showing the drop in resistance of the sensor upon exposure to hydrogen gas. b) Figure depicting the change in response time and sensitivity of the sensor as a function of concentration of hydrogen at room temperature and 50 torr chamber pressure. It can be followed that the response time decreases while the sensitivity increases almost linearly with increase in concentration of hydrogen.

4.1.2.2. Hydrogen detection using titania nanotube synthesized using anodization

The sensor data obtained at our lab indicated that titania nanotubes by anodization technique are sensitive to hydrogen (900ppm) at room temperature. However, the sensitivity obtained (Ra/Rg =1.1) was very poor as compared to the existing published results (Ra/Rg=10^6)[112]. The major reasons were identified as follows:

1. Integration issues: The present sensor data was obtained by coating the metal surface with the platinum nanoparticles and making wire-bond interconnects with the nanotube surface. It has been observed that coating of the Pt nanoparticle on the surface of the nanowires leads to decrease in nanowire resistance by one to two orders of magnitude in air. Coating thickness of Pt on nanotubes surface and heat treatment are the critical parameters. These two parameters are the function of TiO_2 nanotube length, wall thickness and barrier layer thickness. Since heat treatment of Pt sputtered TiO_2 NT samples results in percolation of the platinum nanoparticles inside of the titania nanotubes. Sometime it also results in diffusion of TiO_2 nanoparticles in the barrier layer (between the nanotube and base metal) which results poisoning of the sensor (sensor become full conductive; R= 2000 Ω).

2. Much of the titania nanotubes sensor is dependant on the aspect ratio, wall thickness and diameter of the nanotubes. The best response of titania nanotube was shown by titania nanotubes having 30nm pore diameter and 15 nm wall thickness[101] [Grimes]. As compared to these the nanotubes synthesized in our lab has pore diameters in the range of 100-120nm while the tube thickness varied from 30-50 nm (Detail comparison is given in table 4.2). The thicker wall size does not shift the Fermi level of the titania nanotubes upon the chemisorption of gases like hydrogen and

oxygen as expected from the thin wall nanotubes where Debye length is comparable to space charge layer.(~15 nm from reference number [101,112]). Moreover as depicted by the SEM images (Figure 4.6 b) a large part of the titania nanotubes was still covered by islands of oxides which were not converted into nanotubes. The large coverage of nanotubular surface by metal oxide islands causes a huge reduction in the surface area and a loss of connectivity between the space charge regions of nanotubes as they are disrupted by islands of oxide space charge layer.

3. Grimes et.al[112] have shown that the sensitivity of the TiO_2 nanotube based sensor dropped three order of magnitude when the relative humidity was increased from 3% to 56% in testing environment. They proposed that in humid environment the physisorption of water molecules on a layer of nanotube surface results in the blocking of active sites for chemisorption of hydrogen molecules. They also propose that the underlying blocking of sites chemisoprtion site for hydrogen adsorption might be specific to TiO_2 nanotube. In present study the sensor testing was done at 50 Torr dynamic conditions by maintaining chamber pressure by continuous flow of breathing air (18% moisture). While this may not be the predominant reason but could be a contributing factor to reduce the sensitivity of the gas sensor.

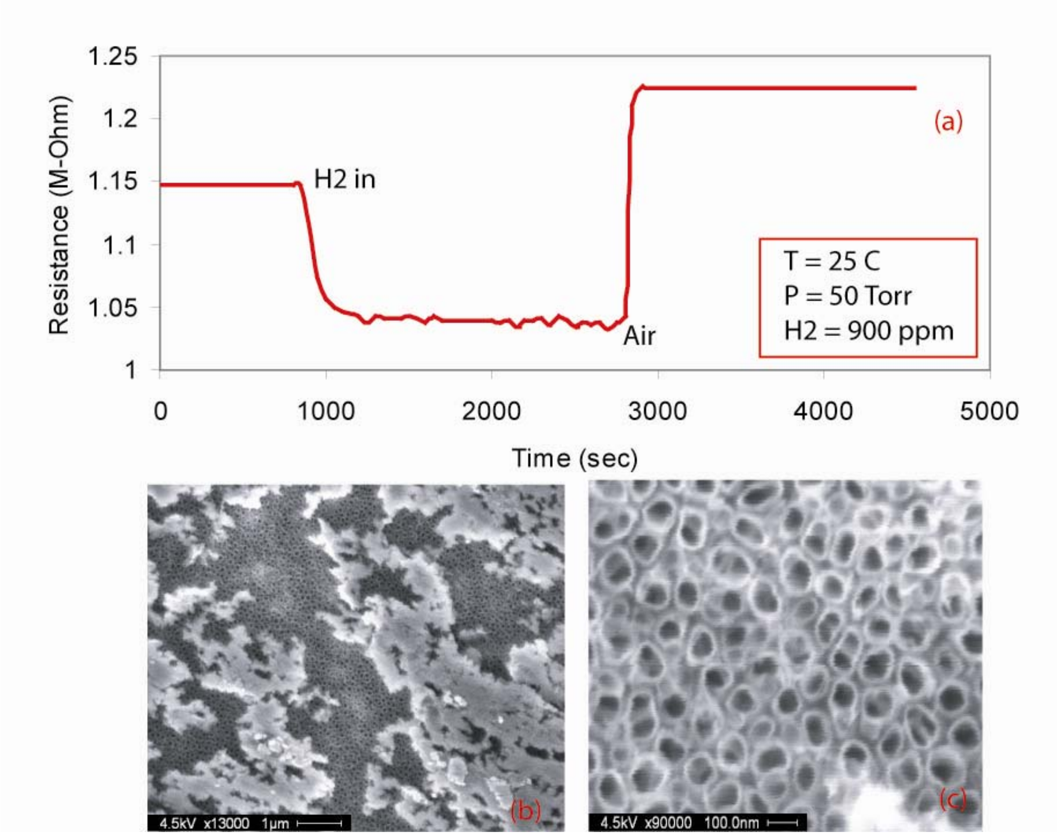

Figure 4.6 (a) Response Transient of the TiO_2 nanotubes synthesized using anodization in 900 ppm H_2 in N_2 environment at room temperature (b) SEM image of TiO_2 nanotube synthesized using anodization technique. (c) From figure it can be observed that nanotube have pore diameter of about 80-100nm with wall thickness 30-40nm.

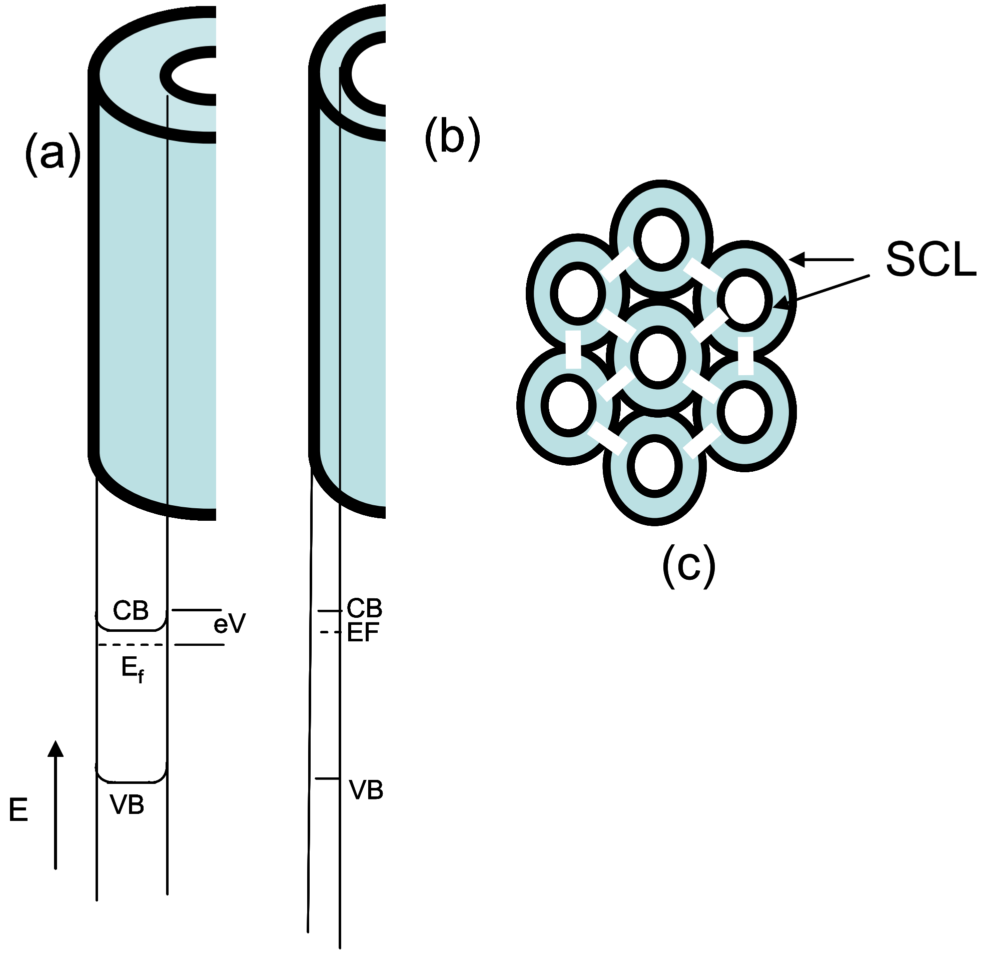

Figure 4.7 Effect of nanotube diameter on the band bending due to surface adsorbed O^- and O_2^- ions (a) diameter (d) > Debye length (L_D = 7nm for TiO_2) and (b) diameter (d) < Debye length (LD = 7nm for TiO_2) (c) figure showing both sides of nanotubes having space charge layer (SCL) and SCL are overlapping; while white bridges indicates tube to tube connecting points.[112]

Table 4.2: Table showing effect of nanotube diameter (in nm) on hydrogen sensitivity.

Nantube Diameter (nm)	Sensitivity
20	1000000 [Grimes et.al.][112]
46	1000 [Grimes et.al.][101,112]
76	100[Grimes et.al.][101,112]
100	1.1 (present study)

CHAPTER 5. CONCLUSIONS

1. Different morphologies of doped and undoped SnO_2 were synthesized using sol-gel, template assisted and thermal evaporation technique. (Chapter 2)

2. Template assisted synthesis of thin film SnO_2 detected hydrogen (900ppm) at room temperature in as low as in 25 seconds with maximum sensitivity (S=Ra/Rg) was about 4. The poor sensitivity shown by the sensor possibly due to surfactant residue on the thin film surface and improper catalyst coverage on the surface of the film. (Chapter 4)

3. SnO_2 nanowires were synthesized using thermal evaporation technique. Contact pads were developed on the nanowires surface and exposed to hydrogen room conditions. Pristine SnO_2 nanowires based sensor showed very sluggish response to hydrogen. Nanowire deposited with Pt (~5nm film) and heated at 400C (1hr) successfully detected hydrogen in 50 seconds. Platinum nanoparticles on the surface of the nanowires plays key role in hydrogen dissociation and improving sensor response kinetics. (Chapter 4)

4. TiO_2 nanoparticles were synthesized using sol-gel technique and successfully transformed to nanotube morphology using hydrothermal synthesis. The entire nanoparticle to nanotube transformation process can be summarized as intial distortion of titania nanoparticles and → fragmentation of O-Ti-O bonds → Planar fragment formation of O^- -Na^+-O^- linkage→ displacement of Na^+ ions by H^+ ions

during neutralization (acidic washing)→ nanotube formation through covalent bond formation between end groups→ removal of H_2O resulting transformation TiO_2 nanotube. Various techniques, such as XRD, TEM and BET analysis were successfully used for elucidating the nanotube formation mechanism. BET analysis shows the surface area of nanotube as high as 400 m^2/g. (Chapter 2)

5. Nanotube synthesized using hydrothermal method were successfully integrated with MEMS device. These nanotube successfully detected hydrogen at room temperature with response time less than 10 sec. Also, sensitivity shown by these nanotubes (S ~29) is the maximum sensitivity observed in current research as compared any other 1D nanostructures (TiO_2 NT using anodization or Thermally grown SnO_2 nanowires). Better performance of these nanotubes is pertained to higher porosity and surface area shown by these nanotubes. (Chapter 4)

6. Nanotube sensor developed using anodization showed very poor gas sensing properties (S~ 1.1) in present study due to integration and synthesis issues. Improving the synthesis of TiO2 nanotube using anodization is still under research in our group. (Chapter 4)

7. The room temperature response kinetics of the present nano-micro integrated sensor is observed to be a function of MEMS device parameters such as electrode spacing, length but it is independent of number of fingers. (Chapter 3)

8. Effect of gap between the electrodes of MEMS device largely affects the gas sensing performance. It has been shown that reducing the spacing of electrodes from 20 micron to 2 micron reduces the response time from 100 seconds to 10 seconds. But this results sensitivity drop of around 3 orders of magnitude. A diffusion model elucidating the effect of electrode spacing on the sensor performance was proposed. This model can theoretically predict the sensor performance such as response time and sensitivity modulation beforehand. (Chapter 3)

9. A handheld sensor device for detection of hydrogen and a handheld device for real time application of gas sensor have also been developed. Details are given in appendix section. Finding of this dissertation are summarized in table 5.1.

Table 5.1 Comparison of various different nanostructured based gas sensor developed in present study.

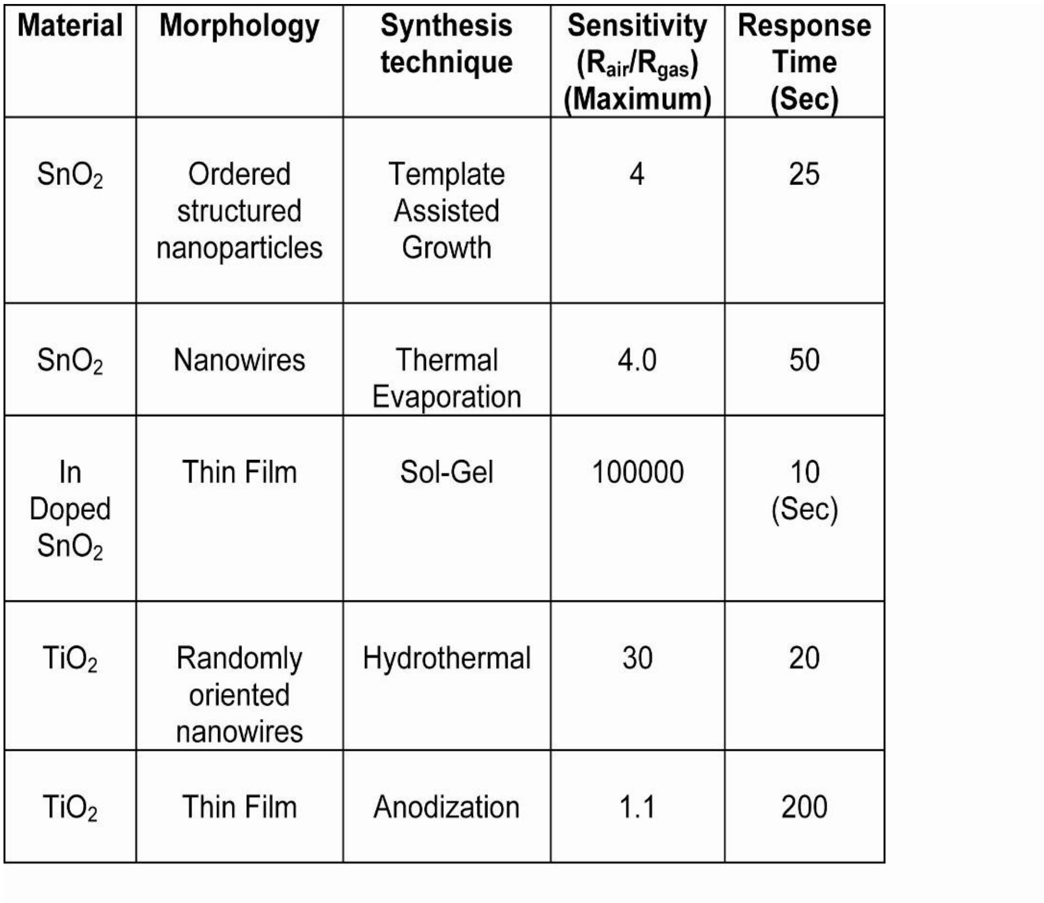

Material	Morphology	Synthesis technique	Sensitivity (R_{air}/R_{gas}) (Maximum)	Response Time (Sec)
SnO_2	Ordered structured nanoparticles	Template Assisted Growth	4	25
SnO_2	Nanowires	Thermal Evaporation	4.0	50
In Doped SnO_2	Thin Film	Sol-Gel	100000	10 (Sec)
TiO_2	Randomly oriented nanowires	Hydrothermal	30	20
TiO_2	Thin Film	Anodization	1.1	200

Future Research Avenues from Current Work

The last two decades have witnessed an extraordinary growth in research on sensors in general with special emphasis on chemical and biochemical sensors. Overall, the sensor market will reach almost $ 50.8 billion by 2008. Space, auto, and food processing industries are predicted to have the highest demand and growth sector. Due to increased demand for compressed natural gas, hydrogen vehicles in coming days validate the importance of hydrogen gas sensors. Though current research has shown successful detection of the hydrogen at the room conditions and response time is less than 10seconds. The finding of this dissertation can be used for the future generation device fabrications:

- Detection of the hydrogen at sub ambient temperature ($T < 0^oC$) and pressure (below 10Torr) is certainly an area for further research. At low temperature adsorption and desorption of the reactive species diminishes which can largely affect the sensor response and recovery .species. are product species
- Effect of multiple dopants (such as Cu, In and Zn) in the nanostructure for creation of oxygen vacancies will be the most important avenue to pursue for enhancing gas sensing performance at room temperature conditions.
- Studying the effect of the wall thickness variation in the TiO_2 nanotubes below 20nm can further significantly enhance sensitivity by maintaining response time of the sensor to few seconds.

- Recovery of the gas sensor using coating or doping rare earth oxides such as CeO_2 can be fundamentally improved. This can be another area to understand this phenomenon in real world.
- For Reducing sensor response time without sacrificing sensitivity further optimization of the MEMS or NEMS device is needed. Possible parameters like variation in MEMS device finger thickness, reducing the spacing between the electrodes to nanometer range (as small as 10nm) can possibly improve the gas sensor response time to few milliseconds. Advances in lithographic trechniques such as Immersion lithography can certainly help to achive these targets.
- Improvement in data acquisition and processing can lead to reduce the possibility of false alarming and erroneousness measurements. In this development of new baseline for measurement after periodic interval can be the possible avenue
- From commercial aspects to develop the technique for scaling up the deposition of solution based nanostructures and using reducing overall cost of the product can certainly a challenge.

APPENDIX

I. Synthesis of highly Ordered SnO_2 nanoparticle thin films:

Details of synthesis process of highly ordered nanoporous thin films of tin oxide having a thickness of about 200 nm with interconnected pores about 4-6 nm in diameter is discussed in detail in appendix section. (shown in appendix figure 1). These nanoporous thin films have a face-centered orthorhombic structure (space group *Fmmm*). They were synthesized using a polyethylene oxide-*b*-polypropylene oxide-*b*-polyethylene oxide triblock copolymer as the structure directing agent and anhydrous tin chloride as the inorganic precursor.[64]

In a typical synthesis, a coating solution was formed by adding $SnCl_4$ and deionized water to a solution of Pluronic-F127 triblock copolymer ($HO(CH_2CH_2O)_n$-$(CH_2CH(CH_3)O)_m$-$(CH_2CH_2O)_nH$; n ~ 106, m ~ 70) in ethyl alcohol. The overall molar ratio of coating solution was 1 $SnCl_4$:1×10^{-2} F127:45 EtOH:15 H_2O. Thin films were prepared from this solution by dip-coating at a withdrawal speed of 1 mm/sec. The films did not have an ordered nanostructure right after dip-coating due to incomplete hydrolysis and condensation of $SnCl_4$. They were subjected to an atmosphere of saturated water vapors at 70 °C for at least 2 hours to drive the hydrolysis and condensation of $SnCl_4$. After this water vapor treatment, the films had an ordered orthorhombic nanostructure. The films were then subjected to a rigorous, sequential thermal treatment at progressively higher temperatures to drive the condensation of the inorganic framework and create template-free porous films. FESEM image of the top surface of film (Fig. 2.2d) reveals the presence of pore openings which allow the gas molecules to diffuse into the film. Also, the interconnected voids left by the template have a diameter of about 5 nm (Fig. 2.2c), making SnO_2 surface throughout the thickness of the film accessible for adsorption of hydrogen. The film retains nanoporous structure (therefore, high surface area) even after calcination at 600 °C and shows no agglomeration. TEM images (Fig. 2.2 c) also confirm presence of highly ordered film of nanocrystallites about 3-4 nm in diameter after calcination at 600 °C.

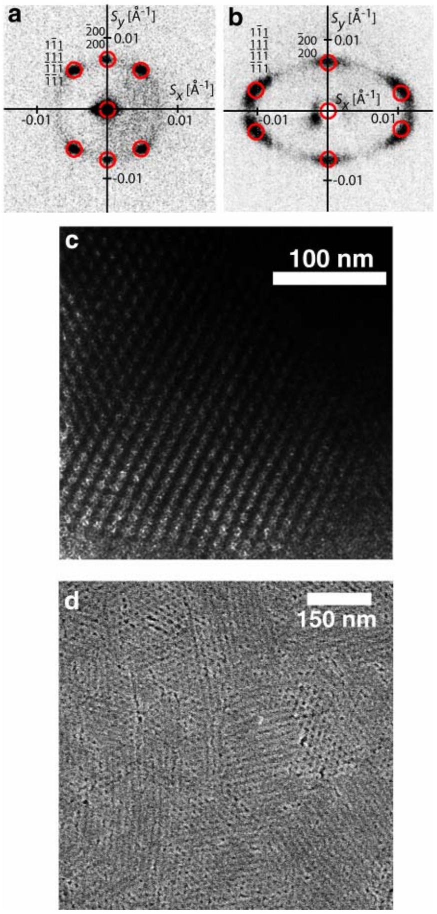

Appendix:Figure-1. Transmission small angle x-ray scattering (SAXS) pattern of an as-made ordered SnO_2–surfactant hybrid film with an angle of incidence of 30° between the X-ray beam and the substrate. Red circles overlaid on the scattering pattern are simulated[13] positions of Bragg spots for an orthorhombic *Fmmm* unit cell. (b) Transmission SAXS for a nano-porous SnO_2 film after the template has been removed by calcination at 600 °C. (c) Transmission electron micrograph of calcined SnO_2 film. Highly ordered and porous nanostructure is retained after calcination. (d) Field emission scanning electron microscopy (FESEM) image the top surface of calcined film. (Courtesy : Dr. Hillhouse Group, Purdue University)

II . Effect of Electrode spacing calculations details:

This appendix explains in detail the calculations involved in determining the fractional change in conductance with respect to the change in finger spacing of MEMS device.

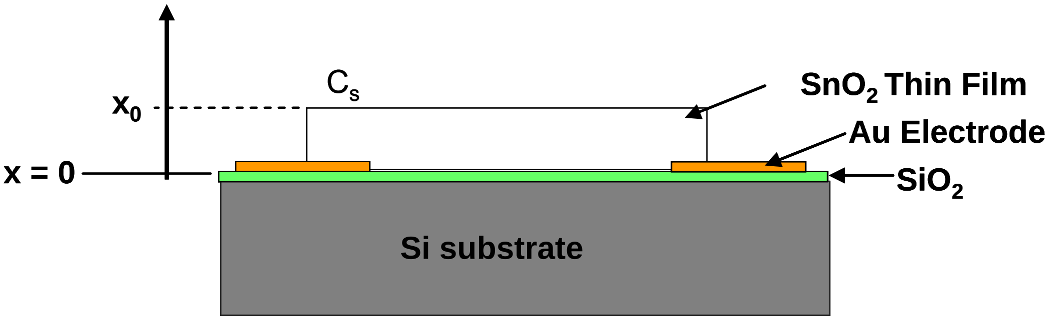

Appendix Figure 2. A cartoon diagram showing the thin film tin oxide sensor. Figure is not drawn in proportion. C_s is surface gas concentration.

When hydrogen gas starts diffusing inside the thin film of metal oxide, the ratio of concentration of gas inside the film at any point can be written as

$$C = \frac{c}{c_S} \qquad \text{...(1)}$$

If *c* is the concentration at a distance *x* inside the film and the gas of initial surface concentration (c_s) diffuses into the thin film of tin oxide (having thickness- x_0 = 150nm in our case); lying on the co-planar electrodes, with boundary conditions:

$C = c / c_S = 1$ when $x = x_0$ (on surface of the film)…………….............(2a)

and

$C = c/c_S = 0$ when $x = 0$ (underneath the film)…………………………(2b)

The solution satisfying above conditions becomes[Error! Bookmark not defined.]:

$$C = \frac{c}{c_S} = 1 - \frac{4}{\pi} \sum_{n=0}^{\infty} \frac{(-1)^n}{2n+1} \cdot e^{-D(2n+1)^2 \pi^2 t / 4 x_0^2} \cdot \cos \frac{(2n+1)\pi . x}{2 x_0} \text{…………..(3)}$$

Where, D is diffusion coefficient of the diffusing gas in present case hydrogen in the ITO which is 4.3 x 10 $^{-11}$ cm^2/s, and *t* is time (vary 0 to1),

Introducing the dimensionless parameters, in equation (3) as follows[Error! Bookmark not defined.]:

$$T = \frac{D.t}{x_0^2} \text{ and } X = \frac{x}{x_0}$$

Equation (3) becomes:

$$C = \frac{c}{c_S} = 1 - \frac{4}{\pi} \sum_{n=0}^{\infty} \frac{(-1)^n}{2n+1} \cdot e^{-(2n+1)^2 \pi^2 . T / 4} \cdot \cos \frac{(2n+1)\pi . X}{2} \text{……….(4)}$$

Analytical solution for the equation (4) is shown in figure below Appendix-2-figure1 which depicts the variation in concentration at different exposure time and varying film thickness. In the present case, the length of electrodes was kept constant (1000μm) for all sensor and the edge effect was neglected (since coating width>>coating thickness).

Solution for equation (3) using metcad is shown in figure 2(a). In figure to avoid variable confusion of mathcad software variable input used in equation shown in figure 1 are p and x, respectively. Out put of equation (3) from figure 2(a) for time t = 0.1 is shown in table

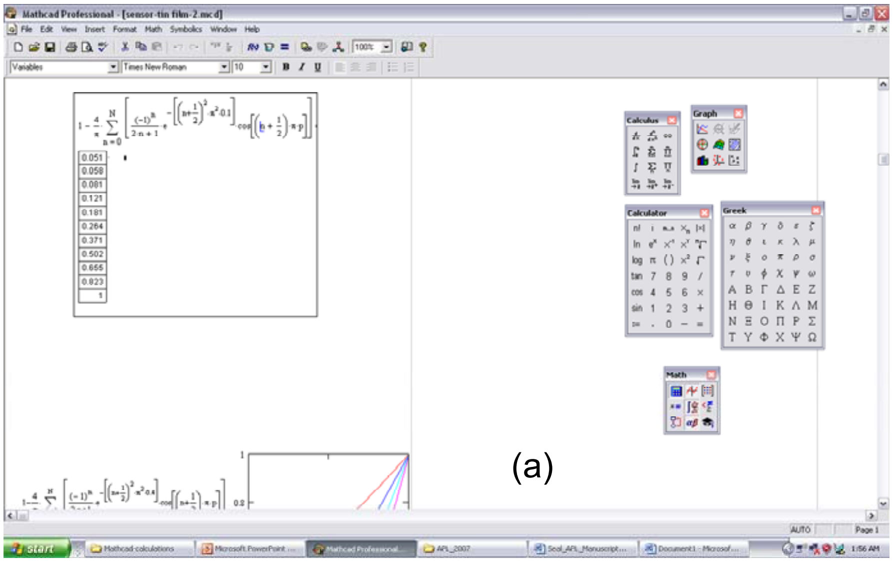

$$1-\frac{4}{\pi}\cdot\sum_{n=0}^{N}\left[\frac{(-1)^n}{2\cdot n+1}\cdot e^{-\left[\left(n+\frac{1}{2}\right)^2\cdot\pi^2\cdot 0.1\right]}\cdot\cos\left[\left(n+\frac{1}{2}\right)\cdot\pi\cdot p\right]\right]$$

```
0.051
0.058
0.081
0.121
0.181
0.264
0.371
0.502
0.655
0.823
1
```

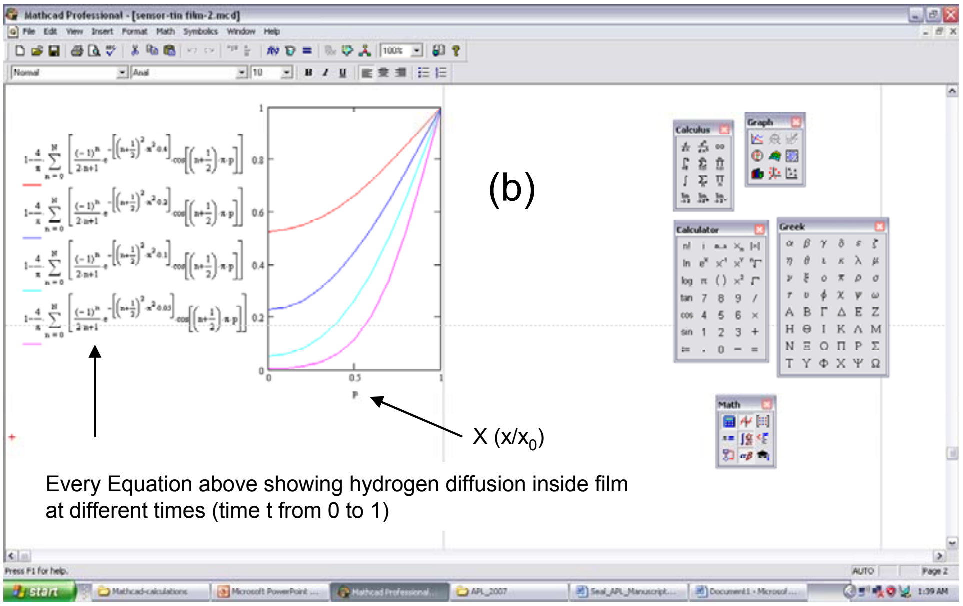

$$1-\frac{4}{\pi}\cdot\sum_{n=0}^{N}\left[\frac{(-1)^n}{2\cdot n+1}\cdot e^{-\left[\left(n+\frac{1}{2}\right)^2\cdot\pi^2\cdot 0.4\right]}\cdot\cos\left[\left(n+\frac{1}{2}\right)\cdot\pi\cdot p\right]\right]$$

$$1-\frac{4}{\pi}\cdot\sum_{n=0}^{N}\left[\frac{(-1)^n}{2\cdot n+1}\cdot e^{-\left[\left(n+\frac{1}{2}\right)^2\cdot\pi^2\cdot 0.2\right]}\cdot\cos\left[\left(n+\frac{1}{2}\right)\cdot\pi\cdot p\right]\right]$$

$$1-\frac{4}{\pi}\cdot\sum_{n=0}^{N}\left[\frac{(-1)^n}{2\cdot n+1}\cdot e^{-\left[\left(n+\frac{1}{2}\right)^2\cdot\pi^2\cdot 0.1\right]}\cdot\cos\left[\left(n+\frac{1}{2}\right)\cdot\pi\cdot p\right]\right]$$

$$1-\frac{4}{\pi}\cdot\sum_{n=0}^{N}\left[\frac{(-1)^n}{2\cdot n+1}\cdot e^{-\left[\left(n+\frac{1}{2}\right)^2\cdot\pi^2\cdot 0.03\right]}\cdot\cos\left[\left(n+\frac{1}{2}\right)\cdot\pi\cdot p\right]\right]$$

X (x/x_0)

Every Equation above showing hydrogen diffusion inside film at different times (time t from 0 to 1)

Appendix Figure 3 (a) Mathcad solution for equation 3 given on page 1. (b) graph showing diffusion of hydrogen inside thin film of tin oxide when time increased from 0 to 1.

According to Ohm’s law the current is proportional to the applied electric field (E). The current density (current per unit area) “*J”* inside the nano tin oxide film is a function of the conductivity (*σ)*, and can be defined as

$$J = \sigma \cdot E \text{ ………………………………………………(5)}$$

While the current flowing through the device is given by[Error! Bookmark not defined.]:

$$i(t) = \int J.ds = \int \sigma.E.ds \text{ …………………………………..(6)}$$

The change in total current [*i(t)*] flowing through the device can be given by:

$$\Delta i(t) = \mu.e.k \int_{cs} c.E.ds \text{ ……………………………………(7)}$$

Where, c is the gas concentration, E is the electric field inside the film while μ and e are electron mobility and charge respectively.

The change in electric conductance is given by[9]:

$$\Delta G(t) = \Delta i(t) / V \text{ ………………………………………..(8)}$$

Where, V is the applied voltage.

The solution for Laplace’s equation for the semiconducting layer above the co-planar electrode is derived in detail elsewhere as:

$$\text{Fractional Change in conductance} = \int_0^1 C[(1-X)^2 + g^2 / 4x_0^2]^{-1/2} dx \text{ ………………………(9)}$$

Where, G_0 is the initial conductance of the film, substituting the value of C calculated in equation (3) in equation 4 , g = 20 micron, x_0 = 150 nm, X = 0.5 (half the total thickness of the film). Figure 3(a) shows the example for 20 micron gap electrode sensor calculations are done for the $x/x_0 = 0.4$.

The mathcad calculation of equation 9 is shown in figure -4 below

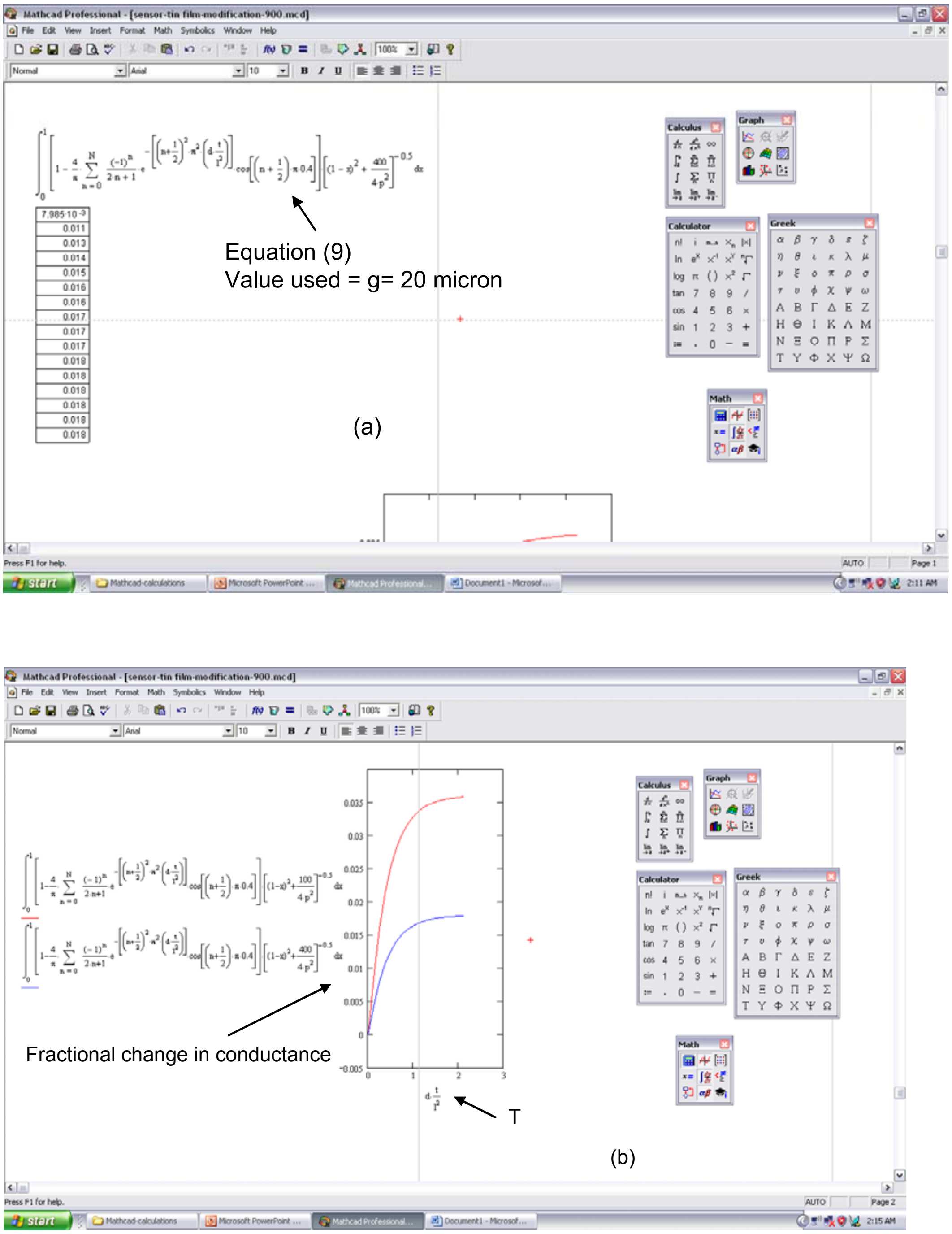

$$\int_0^1 \left[1-\frac{4}{\pi}\cdot\sum_{n=0}^{N}\frac{(-1)^n}{2\cdot n+1}\cdot e^{-\left[\left(n+\frac{1}{2}\right)^2\cdot\pi^2\cdot\left(d\cdot\frac{t}{l^2}\right)\right]}\cdot\cos\left[\left(n+\frac{1}{2}\right)\cdot\pi\cdot 0.4\right]\right]\cdot\left[(1-x)^2+\frac{400}{4\cdot p^2}\right]^{-0.5}dx$$

```
7.985·10^-3
0.011
0.013
0.014
0.015
0.016
0.016
0.017
0.017
0.017
0.018
0.018
0.018
0.018
0.018
0.018
```

Equation (9)
Value used = g= 20 micron

(a)

$$\int_0^1 \left[1-\frac{4}{\pi}\cdot\sum_{n=0}^{N}\frac{(-1)^n}{2\cdot n+1}\cdot e^{-\left[\left(n+\frac{1}{2}\right)^2\cdot\pi^2\cdot\left(d\cdot\frac{t}{l^2}\right)\right]}\cdot\cos\left[\left(n+\frac{1}{2}\right)\cdot\pi\cdot 0.4\right]\right]\cdot\left[(1-x)^2+\frac{100}{4\cdot p^2}\right]^{-0.5}dx$$

$$\int_0^1 \left[1-\frac{4}{\pi}\cdot\sum_{n=0}^{N}\frac{(-1)^n}{2\cdot n+1}\cdot e^{-\left[\left(n+\frac{1}{2}\right)^2\cdot\pi^2\cdot\left(d\cdot\frac{t}{l^2}\right)\right]}\cdot\cos\left[\left(n+\frac{1}{2}\right)\cdot\pi\cdot 0.4\right]\right]\cdot\left[(1-x)^2+\frac{400}{4\cdot p^2}\right]^{-0.5}dx$$

Fractional change in conductance

$d\cdot\frac{t}{l^2}$

T

(b)

Appendix Figure 4. (a) Figure showing calculation of fractional change in conductance for 20 micron electrode spacing (b) Figure showing comparison between fractional change in conductance for 10 micron (red) and 20 micron (blue) electrode spacing.

III. Development of Nano-micron integrated room temperature hydrogen sensor prototype.

A hand-held size prototype instrument was developed using a room temperature hydrogen microsensor. The instrument was designed to generate a warning signal and display a concentration level on exposure to hydrogen leak at room temperature. The sensor was designed and fabricated integrating indium oxide (In_2O_3) doped polycrystalline tin dioxide (SnO_2) nanoparticles with intedigitated microelectrodes then fully-packaged into a portable instrument with a measurement circuit and a display unit. The instrument demonstrated early detection of hydrogen leak at normal environmental conditions without any heated activation of the sensor surface. The whole system consists of a micro control unit (MCU, ATmega48V), a LCD, a piezo buzzer, a positive voltage regulator (SPX3819) and a step-up DC/DC converter (HT7737). The values of resistances at different concentrations (400 ppm and 900 ppm) were tabulated and "written" into the micro control unit (MCU, ATmega48V) of the instrument for calibration. In the calibration process, the MCU generates a "data base" of resistance versus concentration based on the recorded values. The DC/DC converter together with the positive voltage regulator provides the suitable driving voltage to the H_2 sensor, MCU and piezo buzzer. In operation, the MCU transfers the signals (resistances) obtained from the sensor to signals of the concentration by comparing resistances with the data base generated in the calibration step. Converted signals are sent to the display circuitry for LCD and piezo buzzer for alarm signals. Figure 15 shows the measurement, display and buzzer circuitry on a PCB with the H_2 sensor. Figure 16 exhibits a fully packaged portable H_2 instrument with a wire-boned H_2 sensor chip inside. Testing of the instrument was carried out at room temperature without inclusion of any heating element for sensor activation. Upon exposure to the hydrogen gas blown over the instrument at room temperature, within a minute, the instrument generated a warning alarm signal and displayed concentration level in 0.01 up to 0.99, in which the numerical value of 1.00 corresponds to LFL (lower flammable limit) of hydrogen gas.

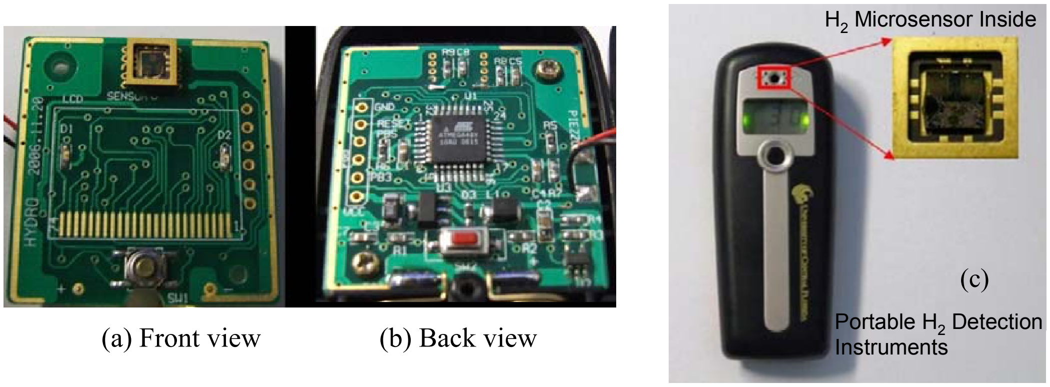

(a) Front view (b) Back view

Appendix – figure 5. (a&b) Front and back view of the different components mounted on the PCB (c) First generation handheld hydrogen sensor. Device includes doped tin oxide coated MEMS device as shown in figure.

REFERENCES

---

[1] R Feynman, *There's plenty of room at the Bottom,* Engg. Sci. 23 (1960) 22.

[2] N. Taguchi, Proc. Intl. Conf. Prod. Eng. Tokyo, Part II, Japan Society of Precision Engineering, 1974

[3] C.F. Quate, *Nanoscience and Engineering: The Next Five Years ,* J. Nanoparticles Res. 1 (1999)131.

[4] M.C. Roco, *Nanaoparticle and Nanotechnology Research*, J. Nanoparticle Res. 4(2002) 171.

[5] C. Suryanarayana, *Current status of research and development in nanocrystalline materials*, .Metallurgia Mater 50 (1994) 799Kulinowoski, Bull. Sci. Tech. Soc. 24 (2004) 24.

[6] T. Haruyama, *Micro- and Nanobiotechnology for Biosensing Cellular Responses*,

Adv. Drug Deli. Rev, 55 (2003) 393 Haruyama, Adv. Drug Deli. Rev. 55 (2003) 393.

[7] R. J. Gorte, H. Kim and J.M. Vohs, *Novel SOFC anodes for the direct electrochemical oxidation of hydrocarbon* , J. Power Sources 106 (2002) 10.

---

[8] C. Suryanarayana and C.C. Koch, Nanostructured Materials, Pergamon Materials Series 2 (1999) 313.

[9] Satyanarayana V. N. T. Kuchibhatla, A.S.Karakoti, D.Bera and S.Seal, *One Dimensional Nanostructured Materials*, Prog. Mater. Sci. 52(2007) 699.

[10] S.Deshpande, S.Patil, KVNT Satyanarayana, S.Seal, *Size dependency variation in lattice parameter and valency states in nanocrystalline cerium oxide*, Appl.Physics Letters 87 (2005) 133113.

[11] CC Koch in *"Nanostructured Materials:Processing properties and potential applications"*, Gary E. McGuire, Stephan M Rossnagel, eds. Material Scinece and Processing Technology Series, Norwich NY (2002)

[12] Y. Lan, X. Guo, H. Xu, Z. Zheng, T. Yan, F. Wu, S. Ringer and T. Song, Titania nanotubes and nanorods prepared from rutile powder , Adv. Functional Mater 15(2005)1310.

[13] Kwang-Min Lee, Sung-Tae Park and Doh-Jae Lee, *Fabrication of ferromagnetic iron carbide nanoparticles by a chemical vapor condensation process*, J Alloys and Compd. 390(2005) 297.

[14] V. Viswanathan, T. Laha, K. Balani, A. Agarwal and S. Seal, *Challenges and Advances in nanocomposite processing techniques*, Mater Sci. Engg. R 54(2006)121

[15] A. Yumoto, F. Hiroki, I. Shiota and N. Niwa, *In situ synthesis of titanium-aluminides in coating with supersonic free-jet PVD using Ti and Al nanoparticles*, Surf Coating Tech. 169-170(2003) 499.

---

[16] Preetam Singh, Ashvani Kumar, Deepak, B.D. Indu and Davinder Kaur, *ZnO nanocrystalline powder synthesized by ultrasonic mist-chemical vapour deposition*,. Optical Mater., *In press*

[17] A.F. Cabrera, A.M. Mudarra Navarro, C.E. Rodríguez Torres and F.H. Sánchez, *Mechanosynthesis of Fe-doped SnO_2 nanoparticles* ,Physica B: Condensed Matter 398(2007) 215.

[18] Jing Xu, Haibin Yang, Qingjiang Yu, Lianxia Chang, Xiaofen Pang, Xiang Li, Hongyang Zhu, Minghui Li and Guangtian Zou , *Preparation and magnetic properties of $SrFe_{12}O_{19}/SiO_2$ nanocomposites with core–shell structure*, Materials Letters 61(2007) 1424.

[19] L.F. Xi and Y.M. Lam, *Synthesis and characterization of CdSe nanorods using a novel microemulsion method at moderate temperature*, Journal of Colloid and Interface Science 316(2007) 771.

[20] https://www.llnl.gov/str/Imbro.html

[21] Caruso, *Nanoengineering of particle surfaces*, Adv Matl. 13(2001)11.

[22] S. Shukla and S.Seal, *Nanocrystalline SnO Gas Sensors in View of Surface Reactions and Modifications,* JOM 54(2002) 35

[23] C.Z. Li, A. Bogozi, W. Huang and N.J. Tao, *Fabrication of stable metallic nanowires with quantized conductance***,** Nanotechnolo. 10 (1999) 221.

---

[24] Vassilios Vargiamidis and George Petsos, *Conductance in modulated nanowires*, Mater. Sci. Engg. B 69-70(2000) 449.

[25] J. Riu,A.Maroto, and F.X. Rius, *Nanosensors in environmental analysis*, Talanta 69(2006) 288.

[26] W. Trimmer, "*Micromechanics and MEMS*", IEEE Press, New York, 1997.

[27] X. Vilanova, E. Llobet,J. Brezmes, J. Calderer and X. Correig, *Analysis of the conductance transient in thick-film tin oxide gas sensors*, Sens Atuators B 48 (1998) 425..

[28] Y. Shimizu, Y. Nakamura and M. Egashira, *Effects of diffusivity of hydrogen and oxygen through pores of thick film* SnO_2*-based sensors on their sensing properties*, Sens. Actuators B 128 (1993) 13.

[29] J. Tamaki, A. Miyaji, J. Makinodan, S. Ogura and S. Konishi, *Effect of micro-gap electrode on detection of dilute* NO_2 *using* WO_3 *thin film microsensors,* Sens. Actuators B 108 (2005) 202.

[30] S. Shukla , P.Zhang, H.J. Cho and S. Seal, *Room temperature hydrogen response kinetics of nano–micro-integrated doped tin oxide sensor*, Sens Actuaotrs B 120(2007) 573.

[31] S. Shukla, R. Agarwal, L. Ludwig, H. J. Cho, and S.Seal, *Effect of ultraviolet radiation exposure on room-temperature hydrogen sensitivity of nanocrystalline doped tin oxide*

---

sensor incorporated into micro-electro-mechanical systems device, J Appl Phys. 97 (2005) 054307.

[32] S. Patil, *Fundamental aspects of regenerative cerium oxide nanoparticles and their applications in nanobiotechnology*, Ph. D. Dissertation, UCF (2006).

[33] S.R. Ovshinsky, Materials Research Society Symposium - Proceedings, Materials and Technology for Hydrogen Economy 801 (2003) 3.

[34] S.F. Yin, B.Q. Xu, X.P. Xou and C.T. Au, *A mini-review on ammonia decomposition catalysts for on-site generation of hydrogen for fuel cell applications*, Appl. Catalysis. A:General 277 (2004) 1.

[35]H.E. Vollmar, C.-U. Maier, C. Noelscher, T. Merklein and M. Poppinger, *Innovative concepts for the co-production of electricity and syngas with solid oxide fuel cells*, J. Power Sources 86 (2000) 90.

[36] http://www.praxair.com/praxair.nsf/1928438066cae92d85256a63004b880d/8e0

[37] http://seecl.mae.ufl.edu/hydrogen/page1.html

[38] http://www.praxair.com/praxair.nsf/AllContent/7E8A75E1CC87FA998525655E0

[39] http://library.thinkquest.org/17940/texts/nuclear_disasters/nuclear_disasters.html

[40] http://www.jsc.nasa.gov/er/seh/explode.html

[41] http://www-pao.ksc.nasa.gov/kscpao/chron/sts-35.htm

---

[42] G.W.Hunter,NASA Technical Memorandum 106300, Lewis Research Center, Cleveland, Ohio, October (1992)

[43] S. Shukla and S. Seal, in Encyclopedia of Sensors edited C. Grimes, E. Dickey and M. Pishko, American Scientific Publishers, Los Angeles (2006), vol. 5, p.379..

[44] M.-I Baraton, L.Merhari, H.Ferkel and J.-F.Castagnet, *Comparison of the gas sensing properties of tin, indium and tungsten oxides nanopowders: carbon monoxide and oxygen detection*, Matl. Sci. Engg. C 19, (2002) 315.

[45] C.Drake, S.Deshpande and S.Seal,*Determination of free carrier density and space charge layer variation in nanocrystalline* In^{3+} *doped tin oxide using Fourier Transform Infrared Spectroscopy,* Appl. Phys. Lett. 89 (2006) 143116.

[46] S. Shukla, S. Seal, L. Ludwig and C. Perrish, *Nanocrystalline indium oxide-doped tin oxide thin film as low temperature hydrogen sensor,* Sens. Actuators B 97 (2004) 256.

[47] H. Pink, L. Treitinger and L. Vite, *Preparation of Fast Detecting* SnO_2 *Gas Sensors,* Jpn. J. Appl. Phys. 19 (1980) 513.

[48] J.Watson, *The tin oxide gas sensor and its applications*, Sens. Actuators, 5 (1984) 29.

[49] L. N. Yannopolus, *Antimony doped stannic oxide based thick film gas sensors*, Sens. Actuators 12 (1987) 77.

---

[50] J.W. Gardner, H.V. Shurmer and T.T. Tan, *Application of an electronic nose to the discrimination of coffees*, Sens. Actuators 6 (1992)71.

[51] S. W. Lee, P. P. Tsai and H. Chen, *Antimony-doped stannic oxide-based thick-film gas sensors, Comparison study of SnO_2 thin- and thick-film gas sensors*. Sens. Actuators B 67 (2000)122.

[52] V. N. Mishra and R. P. Agarwal, *Effect of orthorhombic phase on hydrogen gas sensing property of thick-film sensors fabricated by nanophase tin dioxide*, Microelectronics 29 (1998)861.

[53] Y. –D. Wang, C. –L. Ma, X. –H. Wu, X. –D. Sun and H. –D. Li, *Electrical and gas-sensing properties of mesostructured tin oxide-based H_2 sensor*, Sens. Actuators B 85 (2002) 270.

[54] J. –P. Ahn, S. –H. Kim, J. –K. Park and M. –Y. Huh, *Effect of orthorhombic phase on hydrogen gas sensing property of thick-film sensors fabricated by nanophase tin dioxide*, Sens.Actuators B 94 (2003) 125.

[55] K. Wada and M. Egashira, *Improvement of gas-sensing properties of SnO_2 by surface chemical modification with diethoxydimethylsilane* , Sens. Actuators B 53 (1998) 147.

[56] D. D. Vuong, G. Skai, K. Shimanoe and N. Yamazoe, *Preparation of grain size-controlled tin oxide sols by hydrothermal treatment for thin film sensor application* , Sens. Actuators B 103(2004) 386.

---

[57] S. W. Lee, P. P. Tsai and H. Chen, *Comparison study of SnO_2 thin- and thick-film gas sensors*, Sens. Actuators B 67 (2000) 122.

[58] K. H. Cha, H. C. Park and K. H. Kim, *Effect of palladium doping and film thickness on the H_2-gas sensing characteristics of SnO_2,* Sens. Actuators B 21 (1994) 91.

[59] V. A. Chaudhary, L. S. Mulla and K. Vijayamohanan, *Synergistic sensitivity effects in surface-modified tin oxide hydrogen sensors using ruthenium and palladium oxides*, J. Mater. Sci. Letts. 16 (1997) 1819.

[60] V. A. Chaudhary, L. S. Mulla and K. *Selective hydrogen sensing properties of surface functionalized tin oxide*, Sens. Actuators B 55 (1999) 154.

[61] J. W. Hammond and C. –C. Liu, *Silicon based microfabricated tin oxide gas sensor incorporating use of Hall effect measurement*, Sens. Actuators B 81 (2001) 25.

[62] J. Gong, Q. Chen, W. Fei and S. Seal, *Micromachined nanocrystalline SnO_2 chemical gas sensors for electronic nose*, Sens. Actuators B 102(2004) 117.

[63] C. Drake, *Understanding the low temperature electrical properties of nanocrystalline sno2 for gas sensor applications,* Ph.D. Dissertation, UCF (2007)

[64] V. N. Urade and H. W. Hillhouse, *Synthesis of Thermally Stable Highly Ordered Nanoporous Tin Oxide Thin Films with a 3D Face-Centered Orthorhombic Nanostructure* , J. Phys. Chem. B 109 (2005) 10538.

---

[65] Y. D. Wang, C. L. Ma, X. H. Wu, X. D. Sun and H. D. Li, *Electrical and gas-sensing properties of mesostructured tin oxide-based* H_2 *sensor,* Sens. Actuators B 85 (2002) 270.

[66] Y Y. Shimizu, T. Hyodo and M. Egashira, *Mesoporous semiconducting oxides for gas sensor application,* J. Eur. Ceram. Soc 24 (2004)1389.

[67] T. Wagner, C. D. Kohl, M. Froba and M. Tiemann, *Gas sensing properties of ordered Mesoporous* SnO_2*,* Sensors 6 (2006) 318.

[68] S. Shukla, S. Seal, L. Ludwig and C. Parrish, *Nanocrystalline indium oxide-doped tin oxide thin film as low temperature hydrogen sensor,* Sens. Actuators B 97 (2004) 256.

[69] W. J. Moon, J. H. Yu and G. M. Choi, *The CO and* H_2 *gas selectivity of CuO-doped* SnO_2*–ZnO composite gas sensor,* Sens. Actuators B 87 (2002) 464.

[70] A.P. Chatterjee,P.Mitra and A.K. Mukhopadhyay, Chemically deposited zinc oxide thin film gas sensor, J. Mater. Sci. 34 (1999) 4225..

[71] S.Shukla and S.Seal,*Room Temperature gas sensitivity of nanocrystalline pure tin oxide,* J Nanosci. Nanotechnol. 4(2004)141.

[72] J.-P. Ahn, S. Kim, J. Park, and M. Huh, *Effect of orthorhombic phase on hydrogen gas sensing property of thick-film sensors fabricated by nanophase tin dioxide*, Sensors and Actuators B 94 (2003)125.

---

[73] A. Kolmokov , Y. Zhang, G. Cheng and M. Moskovits, Adv. Materials 15 (2003) 997.

[74] C. Guo, M. Cao, C. Hu, *A novel and low-temperature hydrothermal synthesis of SnO_2 nanorods*, Inorg. Chem. Comm. 7 (2004) 929.

[75] S. Papargyri, D.N. Tsipas, D.A. Papargyris, A.I. Botis, A.D. Papargyris, *Review on production ann synthesis of Nanocrystalline SnO_2,* Sol. State Phenomenon 106 (2005) 57.

[76] S. Shukla, E. Brinley, H.J. Cho and S.Seal, *Electrospinning of hydroxypropyl cellulose fibers and their application in synthesis of nano and submicron tin oxide fibers*, Polymer 46 (2005) 12130.

[77] Y.X. Chen, L.J. Campbell and W.L. Zhou, *Self-catalytic branch growth of SnO_2 nanowire junctions* , J. Crystal Growth, 270(2004)505.

[78] Jong-Soo Lee, Sung-Kyu Sim, Byungdon Min, Kyoungah Cho, S.W.Soo Won Kim and Sangsig Kim, *Structural and optoelectronic properties of SnO_2 nanowires synthesized from ball-milled SnO_2 powders*, J. Crystal Growth, 267(2004)145.

[79] A. Kolmakov, D.O. Klenov, Y. Lilach, S. Stemmer and M. Moskovitz, *Nanoletters* 5 (2005) 667.

[80] S Shukla, V. Vishwanathan and S Seal, *Thermal Evaporation Processing of Nano and Submicron Tin Oxide Rods* , J Phys Chem. B 110 (2006) 11210.

---

[81] R.-Q. Zhang, Y. Lifshit and S.-T. Lee, *Oxide-Assisted Growth of Semiconducting Nanowires*, Adv. Materials 15(2003) 635.

[82] D. Calestani, M. Zha, G. Salviati, L. Lazzarini, L. Zanotti, E. Comini and G. Sberveglieri, *Nucleation and growth of SnO_2 nanowires* , J Crystal Growth 275 (2005) 2083..

[83] Y.P.Leung, W.C.H. Choy,I. Markov, G.K.H.Pang, *Synthesis of wurtzite ZnSe nanorings by thermal evaporation* , Appl. Phys. Lett. 88(2006)183110.

[84] Chien-Cheng Tsai and Hsisheng Teng, *Regulation of the Physical Characteristics of Titania Nanotube Aggregates Synthesized from Hydrothermal Treatment* ,Chem. Mater. 16(2004) 4352.

[85] V.F.Stone and R. Davis, *Synthesis, Characterization, and Photocatalytic Activity of Titania and Niobia Mesoporous Molecular Sieves*,J. Chem Mater.10(1998)1468.

[86] A.Li. Bassi, D. Cattaneo, V. Russo, C.E. Bottani, E. Barborini, T.Mazza, P. Piseri, P. Milani, F.O. Ernst, K. Wegner and S.E. Pratsinis, *Raman spectroscopy characterization of titania nanoparticles produced by flame pyrolysis: The influence of size and stoichiometry* , J Appl. Phys. 98 (2005) 074305.

[87] A.S. Barnard and L.A. Curtiss, *Prediction of TiO_2 Nanoparticle Phase and Shape Transitions Controlled by Surface Chemistry,* Nano Letters 5 (2005) 1261.

[88] Chih-Wen Hsieh, Anthony S.T. Chiang, Cheng-Chung Lee and Sheng-Jenn Yang, *Preparation of TiO_2—B_2O_3 coating by the sol-gel method* ,J Non crystalline Sol. 144 (19992) 53.

---

[89] Z .-Yuan, B.-L. Su, Colloid Surf. A, *Titanium oxide nanotubes, nanofibers and nanowires* , Physico Chem Engg Aspects 241 (2004) 173.

[90] H. H. Ou and S.-L. Lo, *Review of tiatania nanotube synthesized via hydrothermal treatment: Fabrication, modification, application*, Separation Pur. Technol. 58(2007)179.

[91] T. Kasuga, M. Hiramatsu, A. Hoson, A.Sekino, K. Niihara, *Titania Nanotubes Prepared by Chemical Processing* , Adv. Mater. 11 (1999)1307.

[92] Z.-Yuan, B.-L. Su, Colloid Surf. A, *Titanium oxide nanotubes, nanofibers and nanowires*, Physico Chem. Engg. Aspects 241 (2004) 173.

[93] J.M. Wu, *Low temperature preparation of titania nanorods through direct oxidation of titanium with hydrogen peroxide*, J Crystal Growth 269 (2004) 347.

[94] Y. Lan, X.P. Gao, H. Y. Zhu, Z.F. Zheng, T.Y.Yan, F. Wu, S.P. Ringer, D.Y. Song,*Titanate Nanotubes and Nanorods Prepared from Rutile Powder*, Adv. Funct. Mater 15 (2005)1310.

[95] M. Wei, Y. Konishi, H. Zhou, H. Sigihara, A. Arakawa,*Formation of nanotubes* TiO_2 *from layered titanate particles by a soft chemical process*, Sol State Comm 133 (2005)493.

[96] T. Kasuga, *Formation of titanium oxide nanotubes using chemical treatments and their characteristic properties* Thin Sol. Films 496 (2006)41.

---

[97] B.D. Yao, *Formation mechanism of TiO_2 nanotubes* ,App. Phys. Letters 82 (2003) 282.

[98] M. Zhang, Z. Jin, J. Zhang,X. Guo, J. Yang,W. Li,X. Wang and Z. Zhang, Effect of anneling temperature on morphology, structure and photocatalytics behaviour of nanotubed $H_2TiO_4(OH)_2$, J Molecular Catalysis, 217(2003) 203.

[99] J.N. Nian and H. Teng, *Hydrothermal synthesis of single crystalline TiO_2 nanorods and nanotubes as precursor,* J. Phys. Chem B 110(2006)4193.

[100] A.S. Karakoti, K V N T Satyanrayana, D. Bera, R. Filmalter, A. Vincent, *Spiral growth of one dimensional titania nanostrucutres using anodic oxidation*, J. Nanosci Nanotech, 6(2006)2084.

[101] Gopal K. Mor, Oomman K. Varghese, Maggie Paulose, Karthik Shankar and Craig A. Grimes, *A review on highly ordered, vertically oriented TiO_2 nanotube arrays: Fabrication, material properties, and solar energy applications* , Solar Energy Materials and Solar Cells, 90(2006)2011.

[102] Masako Tanaka, *An industrial and applied review of new MEMS devices features*, Microelectronic Engg 84(2007) 1341.

[103] N. Barsan, M. Schweizer-Berberich, W, Gopel, *Fundamental and practical aspects oin the design of nanoscaled SnO_2 gas sensors,* J Anal Chem 365(1999)287.

[104] P.Zhang, S.Deshpande, S.Seal, H.J. Cho, P. Medelius, 5th IEEE Conference on sensors and actuators, Oct. 2007, pp.712-715

---

[105] J. Tamaki, A. Miyaji, J. Makinodan, S. Ogura, S. Konishi, *An industrial and applied review of new MEMS devices features*, Sens and actuators B 108 (2005) 202.

[106] S Shukla and S. Seal, *Constitutive Equation for Gas Sensitivity of Nanocrystalline Tin oxide sensor*, Sens Letters 2 (2004) 125.

[107] J. Ding, T.J. McAvoy, R.E. Cavicchi, S. Semancik, *Surface state trapping models for SnO_2-based microhotplate sensors*, Sens Actuators B 77(2001)597.

[108] J. Crank, *The Mathematics of Diffusion*, 1st ed. (The Clarendon press, Oxford, UK, 1955), pp. 42-62.

[109] C. Liu, *Foundation of MEMS*, 1st ed. (Pearson Education Inc., NJ, USA, 2006) pp. 48-103.

[110] J. W. Gardner, *A diffusion-reaction model of electrical conduction in tin oxide gas sensors*, Semicond. Sci. Techno. 4 (1989) 345.

[111] J.W. Gardner, *Integrated array sensor for detecting organic solvents*, Sens. Actuators 26 (1995) 261.

[112] O.K. Varghesse, D. Gong, M. Paulose,K. Ong and C.A. Grimes, *Hydrogen sensing using titania nanotubes*, Sensors and Actuators B 93(2003) 624.

[113] S. Shukla, S. Seal, L. Ludwig and C Perrish, *Inverse Catalyst effect observed for nanocrsytalline doped tin oxide sensor at low operating temperature*, Sens. Actuators B 104 (2004) 223.

---

[114] S. W. Lee, P.P. Tsai and H.D. Chen, *Structure and gas-sensing characteristics of undoped tin oxide thin films fabricated by ion-assisted deposition*, Sens Actuators B 41 (1997)55.

[115] S.K. Song J.S. Cho, W.K. Choi, H.J. Jung, D.S. Choi, J.Y. Lee, H.K. Baik and S.K. Koh, *Structure and gas-sensing characteristics of undoped tin oxide thin films fabricated by ion-assisted deposition*, Sens Actuators B 41 (1998) 42.

[116] R. Sanjisanis, V. Dermarne and F. Levi, *Hall effect measurements in* SnO_x *film sensors exposed to reducing and oxidizing gases* , Thin Sol. Films, 193-194 (1990) 935.

[117] V.A. Chaudhary, I.S. Mulla and K. Vijay mohanan, *Selective hydrogen sensing properties of surface functionalized tin oxide,* Sens Actuators B 55 (2001)25.

[118] .W. Hammond and C.C. Liu, *Silicon based microfabricated tin oxide gas sensor incorporating use of Hall Effect measurement* , Sens Actuators B 81(2001) 25.

[119] H. T. Wang, B. S. Kang, F. Ren, L. C. Tien, P. W. Sadik, D. P. Norton, S. J. Pearton and J. Lin, Detection of hydrogen at room temperature with catalyst-coated multiple ZnO nanorods, Appl. Phys. A 81 (2005)1117.

[120] W. Eberhardt, F. Greunter and E.W. Plummer, *Bonding of H to Ni, Pd, and Pt Surfaces* , Phys. Rev. Lett. 46 (1981)1085.

[121] D. Calestani, M.Zha, A. Zappettini, L. Lazzarini, G. Salviati, L. Zanotti and G. Sberveglieri, *structural and optical study of SnO2 nanobelts and nanowires,* Material Science and Engg C 25(2005) 625.

---

[122] A.G. Munoz, *Semiconducting properties of Self organized TiO_2 nanotubes,52 (2007)4167.*

[123] A. Kolmokov and M. Moskovits, *Chemical Sensing and Catalysis by one dimensional nanostructures*, Ann. Rev. Mater. Res. 34 (2004)151.

[124] Y.K. Jun, *High H_2 sensing behavior of TiO_2 films formed by thermal oxidation*, Sensors and Actuators B 107 (2005)264.

[125] Chunmei Zhu, Liangyan Wang, Linren Kong, Xi Yang, Liansheng Wang, Shaojian Zheng, Feili Chen, Feng MaiZhi and Huang Zong, *Photocatalytic degradation of AZO dyes by supported TiO_2 + UV in aqueous solution*, Chemosphere 41(2000) 303.